THE VISCOSITY OF FLUIDS IN THE CRITICAL REGION

Thesis by

Hal Jeffry Strumpf

In Partial Fulfillment of the Requirements

for the Degree of

Doctor of Philosophy

California Institute of Technology

Pasadena, California

1972

(Submitted April 21, 1972)

ACKNOWLEDGMENTS

I would like to thank my research advisor, Professor C. J. Pings, for his interest and guidance throughout the course of the investigation. Special thanks go to Dr. Anthony F. Collings, who was instrumental in initiating the project, and Hollis H. Reamer, whose helpful assistance was invaluable. George Griffith rendered assistance in constructing the apparatus.

During my graduate studies I received financial assistance in the form of a Stauffer Fellowship, a New York State Regents Fellowship, a National Science Foundation Traineeship, a Fluor Fellowship, and a Graduate Research Assistantship from Caltech.

I would like to thank my wife, Faye, and my parents for their continuous encouragement.

ABSTRACT

The viscosity of xenon has been measured along ten isochores and the viscosity of ethane has been measured along five isochores in the region of the gas-liquid critical point. The viscometer was a specially cut quartz cylinder, which was excited into a torsionally oscillating mode upon application of an alternating voltage. The cylinder, oscillating in this manner, generated a viscous wave when immersed in a fluid. The viscous wave caused an impedance loading on the quartz which changed its resonant resistance and frequency. This change in resonant properties can be related to the viscosity-density product of the fluid.

The resonant properties of the quartz crystal were measured by connecting the crystal to the unknown arm of a Wheatstone bridge circuit, modified so as to measure parallel resistance and capacitance. The crystal was driven by a very stable frequency generator, and the circuit was tuned using an oscilloscope as a null detector.

The crystal was enclosed in a high pressure stainless steel cell and placed in a water thermostat which controlled temperature to $\pm$ 0.001^{o}C. The temperature was measured with a calibrated platinum resistance thermometer. The density was determined by a gravimetric technique.

The viscosities exhibit an "anomalous" increase as the critical temperature is approached along an isochore of close to critical density. The anomaly is consistent with a logarithmic divergence of the form:

$$\Delta\eta = A \log \varepsilon + B$$

where $\Delta\eta$ is the anomalous viscosity, ε is the reduced temperature difference from critical, and A and B are constants. The possibility of an exponential divergence or a cusp-type finite limit for viscosity is not precluded, however.

The critical temperatures and densities have been determined by visual observations. For xenon, $T_c = 16.627 \pm 0.005^{\circ}C$, $\rho_c = 1.11 \pm 0.01$ g/cm^3; for ethane, $T_c = 32.218 \pm 0.005^{\circ}C$, $\rho_c = 0.2055 \pm 0.002$ g/cm^3. The temperatures are stated with respect to the 1968 International Practical Temperature Scale.

Table of Contents

List of Figures

List of Tables

Nomenclature

Roman Letters

A, A_{1-5}	Constant
a	$\omega L - \frac{1}{\omega C}$
B	Constant
C, C'	Capacitance
C_v	Heat capacity at constant volume
E	Voltage; modulus of elasticity
E_1, E_2	Scaling law parameters
f	Resonant frequency
f(t)	Arbitrary function of t
Δf	Bandwidth
g	Local acceleration of gravity
$\underline{g}$	Gravitational force vector
g(y)	Arbitrary function of y
H	Internal magnetic field
h(x)	Scaling law function
I	Current
j	$\sqrt{-1}$
k	$\frac{1}{\delta}(j+1)$
k_T	Thermal conductivity
L	Inductance
L_1, L_2	Electrical leads
ℓ	Length
M	Residual magnetization; mass

N_{Re}	Reynolds number
P	Pressure
PO	Instantaneous power per unit area
Q	Quality of circuit
R	Resistance; radius
r	Radius
S	Surface area
T	Temperature
T_{ref}	Reference temperature
t	Time; temperature; wall thickness
V	Volume
$\underline{v}$	Velocity vector
W	Energy per cycle
W_D	Energy dissipated per cycle
W_S	Energy stored per cycle
x,y,z	Coordinate axes
x, x_o	Scaling law parameters
Z	Impedance
Z_A, Z_B	Bridge impedances
Z_P	Impedance of parallel arm
Z_S	Impedance of series arm
Z_T	Total impedance
z	Height

Greek Letters

α	Callendar constant
β	Critical exponent
γ	Critical exponent
Δ	Logarithmic decrement
δ	Penetration depth; Callendar constant
ε	Reduced temperature difference from critical; circumferential strain
η	Viscosity
$\Delta\eta$	Anomalous viscosity
η_{id}	Ideal viscosity
η^*	Excess viscosity
κ_T	Isothermal compressibility
μ	Chemical potential
ρ	Density
ρ_q	Density of quartz
σ	Shear elastic constant
$\underline{\underline{\tau}}$	Stress tensor
Φ_v	Dissipation function
ϕ	Critical exponent for viscosity
χ	Magnetic susceptibility
ω	Angular frequency

Subscripts

A	Air
B	Bulk; bridge balance
c	Critical

h.p.	Half power
LD	At loading
m	Mass
N	Variable
o	Vacuum conditions; ice point
V	Vacuum conditions
w	Surface of the crystal
X	Unknown

Superscripts

*	Reduced conditions

I. INTRODUCTION

In recent years there has been a great interest, both theoretical and experimental, in the study of phenomena in the neighborhood of critical points. The large number of recent review articles and conferences on critical phenomena is indicative of this interest[1,2,3]. Basically, a critical point is a limiting point that marks the disappearance of all differences between two distinct phases. It is becoming increasingly apparent that the critical behavior in many diverse types of systems is analogous.

For example, for the single-component gas-liquid critical region, the isothermal compressibility can be characterized by an equation of the following form along the critical isochore:

$$\kappa_T \sim \varepsilon^{-\gamma} \quad , \quad T > T_c \tag{1}$$

where κ_T is the isothermal compressibility $= \frac{1}{\rho} \left(\frac{\partial \rho}{\partial P}\right)_T$

ε is the reduced temperature difference from critical $= \frac{T - T_c}{T_c}$

γ is a critical exponent greater than zero

T is the temperature

ρ is the density

P is the pressure

and the subscript c indicates the property at the critical point.

There is a critical point exhibited by ferromagnetic materials, known as the Curie point. If a magnetic field is applied to a ferromagnet, a magnetic moment is produced which remains after the field is removed. As the temperature is raised, the magnitude of the remaining moment decreases, until at the Curie temperature, no moment remains

after the field is removed. The magnetic susceptibility χ , defined as $(\partial M/\partial H)_T$ where M is the residual magnetization and H is the internal magnetic field, is thought to be analogous to the isothermal compressibility. An equation of the form:

$$\chi \sim \varepsilon^{-\gamma} \quad , \qquad T > T_c \tag{2}$$

has been found to be valid if evaluated at a zero internal field. The value of γ is approximately the same for both systems[3].

There are a number of other critical systems which are thought to exhibit analogous behavior. For example, liquid helium exhibits a critical transition at the lambda point, below which it acquires strange flow properties. Partially miscible binary liquid mixtures often exhibit a critical transition at a consolute or critical mixing point. The critical mixing points are of two types, called upper and lower consolute points. For an upper consolute point, the components become miscible in all proportions above the critical temperature. For systems exhibiting a lower consolute point, the components are totally miscible below the critical temperature, at least until a solid phase is formed. Critical points are known to exist for ferro-electric, anti-ferromagnetic, superconductor, ternary mixture plait point[4], and other systems.

One of the most interesting facets of critical phenomena is the anomalous behavior of some of the physical properties. It can be seen from Eqs. (1) and (2), that the isothermal compressibility and susceptibility get very large as the critical temperature is closely

approached. In fact, it is believed that the properties diverge to infinity at the critical temperature. Other thermodynamic properties, such as the heat capacity at constant volume and the isobaric volumetric expansion, exhibit anomalously large increases as the critical point is approached. It is often attempted to describe the behavior of these properties in the critical region by exponential relationships of the form of Eqs. (1) and (2). A whole series of relationships have been formulated, with each property having its own critical index (exponent).

The behavior of the transport properties is less clear than that of the thermodynamic properties. The thermal conductivity has been found experimentally to approach a very large value in the region of the gas-liquid critical point[5]. In the consolute region of binary liquid mixtures, the thermal conductivity appears to exhibit no anomaly[2], although the experimental data are extremely scant.

The thermal diffusivity, which is equal to the ratio of the thermal conductivity to the product of the density and the heat capacity at constant pressure, appears to approach a value of zero close to the critical point of a pure substance[6]. This seems to indicate that the divergence of the heat capacity at constant pressure is stronger than the divergence of the thermal conductivity.

It also appears that the diffusion coefficient for a binary liquid mixture approaches a value of zero near the consolute point[6].

There have been a number of investigations into the viscosity of binary mixtures near their consolute points, none of which were

particularly well suited for such measurements. Some investigators interpreted their results as indicating an exponential relationship of the form[7]

$$\Delta\eta = A\varepsilon^{-\phi} + B \tag{3}$$

where $\Delta\eta$ is the "anomalous" viscosity, which is discussed in a later section

A and B are constants

ϕ is the critical exponent for viscosity, greater than zero.

However, it now appears that the anomalous viscosity can be better characterized by a logarithmic relationship:

$$\Delta\eta = A \log \varepsilon + B \quad . \tag{4}$$

Equation (4) is sometimes construed as being the limit of Eq. (3) for $\phi = 0$ [8].

It should be noted, as Kadanoff and Swift[9] pointed out, that the differentiation among a small exponential divergence, a logarithmic divergence, and a cusp-type finite limit for viscosity is very difficult without precise data very close to the critical temperature.

The present investigation is concerned with the measurement of viscosity in the region of the gas-liquid critical point. To expand on the previously given definition, the gas-liquid critical point is the point at which the properties of the gas and liquid phases become identical. The critical point represents the maximum temperature and pressure for coexistence between the two phases. The divergence to infinity of the isothermal compressibility has also been used to define

the critical point[3].

Since the compressibility is so large in the critical region, a small pressure differential results in a very large density change. Thus, any pressure changes or instabilities in a critical region experiment tend to greatly reduce the validity of the apparent results.

Most of the conventional methods for determining viscosity, such as rolling ball, falling weight, and transpiration (capillary flow) techniques require or result in pressure changes in the system. Viscosities determined by any of the above techniques are, at best, questionable in the critical region, even for very small pressure differences. For completeness it should be mentioned that with a capillary flow method Michels, et al.[10] reported a large anomalous viscosity in the critical region of carbon dioxide, while Starling, et al.[11] reported no anomalous behavior in the critical regions of ethane, propane, and butane.

Naldrett and Maass[12] and Kestin, Whitelaw, and Zien[13] have measured the viscosity of carbon dioxide in the critical region by an oscillating disk method. This procedure, somewhat similar in principle to the torsional crystal method, measures the damping of a slowly oscillating disk located between two fixed plates, and immersed in the fluid of interest. The rate of damping of the disk can be related to the viscosity of the fluid.

This method, along with the torsional crystal technique, has the great advantage over conventional methods of not producing any macroscopic pressure differences in the measurement of the viscosity. The two above investigations produced somewhat similar results,

although differing by as much as 7% close to the critical point. Naldrett and Maass[12] apparently got to within 0.1°C ($\varepsilon = 3.3 \times 10^{-4}$) of the critical temperature, while Kestin, et al.[13] got to within 0.16°C ($\varepsilon = 5.3 \times 10^{-4}$) of the critical temperature. Both experiments found a weak anomaly in the viscosity as the critical point was approached, much smaller than that found by Michels, et al.[10]. The data were not precise enough for fitting to a relationship of the form of Eq. (3) or (4). The analysis of the oscillating disk method is very complicated and both investigations determined the relative, rather than the absolute, viscosity.

Diller[14] measured the viscosity of parahydrogen in the critical region by a torsional crystal technique, and reported no anomalous behavior to within $\varepsilon = 7 \times 10^{-4}$.

The torsional crystal technique seems particularly well suited for viscosity measurements in the critical region. The torsionally oscillating crystal produces only microscopic pressure and temperature changes, resulting in negligible density variations, even very close to the critical point (see Appendix I for details).

The crystal has a height of only 0.3 cm in the gravitational field, thus minimizing density gradients due to gravity as much as possible. Gravitational effects, which are a serious problem in the critical region, are discussed in a later section.

II. THEORY OF METHOD

A. Torsional Crystal Viscometer

The torsional crystal method is the technique used for measuring viscosity in the present investigation. This method was originally developed by W. P. Mason[15] and improved upon by Rouse, et al.[16] and others. A quartz crystal was cut in the form of a right circular cylinder. The axis of the cylinder was cut along the x-crystallographic axis of quartz, as defined in the 1949 Institute of Radio Engineers (IRE) standard[17]. This cut was initially proposed by Giebe and Scheibe[18] and is shown in Figure 1.

A quartz crystal cut in this manner acts as a piezoelectric transducer. Piezoelectricity has been defined by W. G. Cady as "electric polarization produced by a mechanical strain in crystals belonging to certain classes"[19]. In the use of the crystal as a viscometer, the quartz becomes strained upon the application of a voltage, and the phenomenon should more properly be called the converse piezoelectric effect. The strain produced in the crystal is proportional to the applied voltage.

Four gold electrodes have been evaporated onto the surface of the cylinder (ends excluded) in 80 degree quadrants, the unplated strips lying in the y- and z-axes. The central lines of the electrodes make angles of 45° with respect to the y-axis. Four electrical leads were attached to the crystal, each lead at the center line of an electrode and at the longitudinal center of the crystal. These attachment positions represent nodal points of crystal motion. Viscometers

of similar plating and lead configuration have been used successfully by Collings[20] and others. A sketch of the crystal configuration is shown in Figure 2.

If the opposite leads are connected electrically, and an alternating voltage is applied across the two electrode pairs, an electric field is produced which causes a torsional strain in the crystal. This means that while one end is sheared to the right, the other end is sheared to the left, and vice versa. Thus one end of the crystal is twisted with respect to the other end.

The resonant frequency of the crystal, in its fundamental mode, is given by[21]:

$$f_o = \frac{1}{2\ell}\sqrt{\frac{\sigma}{\rho_q}} \tag{5}$$

where f_o is the resonant frequency in a vacuum

ℓ is the length of the crystal

ρ_q is the density of quartz

σ is the shear elastic constant equal to 40.5×10^{10} dyne/cm^2 for quartz in torsion[21].

The frequency of oscillation can be seen to be a function of the length of the crystal. The length can be considered as equal to half a "wavelength", with a node at the center (where the leads are attached) and antinodes at the ends. The grouping $\sqrt{\sigma/\rho_q}$ is a velocity type term, constant for quartz in torsion, equal to about 3.9×10^5 cm/sec.

If the torsionally oscillating crystal is immersed in a viscous fluid, a highly attenuated viscous (or shear) wave is produced, causing

the fluid in the immediate vicinity of the surface of the crystal to undergo a shearing force. The viscous wave causes an impedance loading on the crystal, which lowers its resonant frequency and increases its resonant resistance. The change in these electrical properties can be related to the viscosity of the medium.

Before developing the relationship between the resonant properties and the viscosity, it is useful to consider a parameter known as the penetration depth of the viscous wave δ given by[22]

$$\delta = \sqrt{\frac{\eta}{\pi f \rho}} \tag{6}$$

where η is the viscosity of the fluid

f is the resonant frequency of the crystal in the fluid

ρ is the density of the fluid.

The penetration depth is a characteristic length for the system and is equal to the distance the shear wave travels (from the crystal surface) before its amplitude is $1/e$ times its maximum amplitude at the surface of the crystal; e is the base of natural logarithms. Since the wave is highly attenuated, it is expected that the penetration depth would be quite small. Looking ahead, for xenon in the critical region, $\eta \sim 6 \times 10^{-4}$ g/cm sec, $f \sim 38{,}700$ Hz, and $\rho \sim 1.11$ g/cm^3. This gives a penetration depth of about 6.7×10^{-5} cm. Since the radius of the crystal is 0.15 cm, the assumption can be made that the shear wave is propagated from a plane surface, since its characteristic length is much smaller than the curvature of the crystal surface.

Consider the torsionally oscillating crystal shown in Figure 3. The length of the crystal is along the x-axis. The viscous wave, which is assumed to be planar, is propagated in the y-direction, normal to the crystal surface. Particle motion, and hence velocity, is in the z-direction, tangent to the crystal surface.

To relate the resonant properties of the crystal to the viscosity of the fluid, consider the general equation of motion for a Newtonian fluid as given in Bird, Stewart, and Lightfoot[23]:

$$\rho \frac{D\underline{v}}{Dt} = -\nabla P - [\nabla \cdot \underline{\underline{\tau}}] + \rho \underline{g} \tag{7}$$

where D/Dt is the substantial derivative (t is time)

$\underline{v}$ is the velocity vector

$\underline{\underline{\tau}}$ is the stress tensor

$\underline{g}$ is the gravitational force per unit mass vector.

Since the wave is planar, the only component of the velocity having a non-zero value is v_z, which is a function only of y. Thus the only component of the stress tensor having a non-zero value is τ_{yz}, which for a Newtonian fluid is given by:

$$\tau_{yz} = -\eta \frac{\partial v_z}{\partial y} \tag{8}$$

Using the definition of the z-component of the substantial derivative:

$$\frac{Dv_z}{Dt} = \frac{\partial v_z}{\partial t} + v_x \frac{\partial v_z}{\partial x} + v_y \frac{\partial v_z}{\partial y} + v_z \frac{\partial v_z}{\partial z} \tag{9}$$

and substituting this into Eq. (7), the result is:

$$\rho \frac{\partial v_z}{\partial t} = - \frac{\partial \tau_{yz}}{\partial y} = \eta \frac{\partial^2 v_z}{\partial y^2} \tag{10}$$

All terms equal to zero have been eliminated. Since the wave is so highly attenuated, it can be assumed that the change in the bulk fluid pressure caused by the crystal motion is very small (see Appendix I). Thus, the only non-zero component of ∇P is the vertical component in the gravitational field. This term is equal to the vertical component of the gravitational field vector $\rho \underline{g}$ and cancels.

Equation (10) can be solved by considering that the solution is a product of functions of t and y, i.e.,

$$v_z(t,y) = f(t) \cdot g(y) \tag{11}$$

The torsional oscillations of the crystal can be considered simple harmonic motion, for which the equation of motion is:

$$\frac{\partial v_z}{\partial t} = j\omega v_z \tag{12}$$

where $j = \sqrt{-1}$

ω is the angular frequency, equal to $2\pi f$.

The solution to Eq. (12) yields:

$$f(t) = A_1 \exp(j\omega t) \tag{13}$$

where A_1 is a constant.

To find $g(y)$, Eq. (12) is substituted into Eq. (10) to give:

$$\frac{\partial^2 v_z}{\partial y^2} - \frac{2\pi f j \rho}{\eta} = 0 \quad . \tag{14}$$

The solution to Eq. (14) yields:

$$g(y) = A_2 \exp(-ky) + A_3 \exp(+ky) \tag{15}$$

where A_2 and A_3 are constants, and

$$k = \sqrt{\frac{2\pi f j \rho}{\eta}} \quad .$$

Thus

$$v_z(t,y) = A_4 \exp(j\omega t - ky) + A_5 \exp(j\omega t + ky) \tag{16}$$

where A_4 and A_5 are constants, is a solution to Eq. (10).

If it is assumed that the velocity of the fluid in contact with the surface of the crystal is the same as that of the crystal itself, the boundary conditions can be considered to be:

$$\begin{aligned} v_z &= v_w \qquad \text{at} \qquad y = 0,\ t = 0 \\ v_z &= 0 \qquad \text{at} \qquad y = \infty \end{aligned} \tag{17}$$

where v_w is the velocity at the wall.

Substituting the boundary conditions into Eq. (16) gives:

$$v_z(t,y) = v_w \exp(j\omega t - ky) \quad . \tag{18}$$

The real part of the velocity can be determined as follows:

$$k = \sqrt{\frac{2\pi f j \rho}{\eta}} = \sqrt{\frac{2\pi f \rho}{\eta} \frac{(j+1)^2}{2}}$$

$$k = \sqrt{\frac{\pi f \rho}{\eta}}\,(j+1) = \frac{1}{\delta}\,(j+1) \quad . \tag{19}$$

Substitution into Eq. (18) gives:

$$v_z = v_w \exp[j\omega t - \frac{y}{\delta}\,(j+1)]$$

$$v_z = v_w \exp[j(\omega t - \frac{y}{\delta}) - \frac{y}{\delta}]$$

$$\text{Real}[v_z] = v_w\, e^{-y/\delta} \cos(\omega t - \frac{y}{\delta}) \quad . \tag{20}$$

The real part of v_z will still be written v_z .

It can be seen from Eq. (20) that the penetration depth δ is indeed the distance a wave must travel for its amplitude to be 1/e times its maximum amplitude. The shear stress can be determined from Eqs. (8) and (20):

$$\tau_{yz} = -\eta \frac{\partial}{\partial y} [v_w\, e^{-y/\delta} \cos(\omega t - \frac{y}{\delta})]$$

$$\tau_{yz} = -\frac{\eta v_w}{\delta}\, e^{-y/\delta} [\sin(\omega t - \frac{y}{\delta}) - \cos(\omega t - \frac{y}{\delta})] \quad . \tag{21}$$

At this point it is useful to consider the common representation of the equivalent circuit for an oscillating piezoelectric crystal[24], that of a series resonant branch (consisting of a resistance R , a capacitance C , and an inductance L) in parallel with a capacitance C' . Far from resonance the impedance of the series arm is extremely high; thus the total impedance of the crystal is the parallel capacitance C' . At series resonance, the capacitive and inductive reactances in the series arm cancel; the impedance of the crystal is now the resistance R in parallel with the capacitance C'.

The equivalent circuits are shown in Figure 4.

It is useful to recall two parameters from simple circuit theory. Considering the series resonant arm, the logarithmic decrement Δ of the circuit is defined as the ratio of the amplitude of two successive oscillations, and is given by[25]

$$\Delta = \frac{\pi R}{\omega L} \quad . \tag{22}$$

The quality Q of the circuit is defined as[26]

$$Q = \frac{\omega L}{R} \quad . \tag{23}$$

The quality is thus equal to π/Δ . An alternate definition for the quality is[27]

$$Q = \frac{2\pi W_S}{W_D} \tag{24}$$

where W_S is the energy stored per cycle

W_D is the energy dissipated per cycle.

The energy dissipated by the crystal, per cycle, can be considered equal to the viscous dissipation of energy by the fluid, per cycle, if other energy losses (conduction, radiation, etc.) are neglected, as seems quite reasonable. The viscous energy supplied to the fluid can be determined by considering the instantaneous power of the crystal per unit area PO which is given by the product of the velocity and the shear stress at the crystal surface $y = 0$

$$PO = \tau_{yz} v_z \Big|_{y=0}$$

$$PO = -\frac{\eta v_w}{\delta}\,[\sin \omega t - \cos \omega t]\, v_w \cos \omega t$$

$$PO = -\frac{\eta v_w^2}{\delta}\,[\sin \omega t \cos \omega t - \cos^2 \omega t] \quad . \tag{25}$$

The energy dissipated per cycle is found by integrating Eq. (25) over the surface area of the crystal and one cycle:

$$W_D = \int_S \int_0^{2\pi/\omega} -\frac{\eta v_w^2}{\delta}\,[\sin \omega t \cos \omega t - \cos^2 \omega t]\,dt\,ds \tag{26}$$

where S is the surface area of the crystal including the ends. Integration yields

$$W_D = \frac{\pi \eta v_w^2 S}{\omega \delta} \quad . \tag{27}$$

The energy stored per cycle is simply the average potential energy of a harmonic oscillator which is equal to the average kinetic energy and is given by[28]

$$W_S = \frac{1}{4} M v_w^2 \tag{28}$$

where M is the mass of the crystal.

Up to this point it has been implicitly assumed that the crystal, envisioned to be an infinite plane, is oscillating at the same velocity along its (infinite) length. This is, in fact, not the case. The velocity varies sinusoidally with antinodes at the ends and a node at the center (as previously mentioned). However, each differential length along the x-axis can be considered to be a point of propagation for the wave described in Eq. (18). It seems reasonable to assume that the term v_w in Eqs. (27) and (28) is actually a sinusoidally

oscillating velocity (with length x). The velocities are still equal and will cancel in Eq. (24) as seen below.

Combining Eqs. (22), (23), (24), (27), and (28) gives:

$$\Delta = \frac{2\pi\eta S}{M\omega\delta} \tag{29}$$

Using the definition of δ ,

$$\Delta = \left(\frac{\eta\pi\rho}{f}\right)^{1/2} \frac{S}{M} \tag{30}$$

The logarithmic decrement in Eq. (30) represents the damping of the crystal due to viscous losses. However, the "observed" damping also includes losses due to the internal friction of the quartz and resistance caused by the imperfect attachment of the electrical leads. The nonviscous losses can be represented by Δ_o , which is assumed to be equal to the logarithmic decrement of the crystal in a vacuum, given by

$$\Delta_o = \frac{\pi R_o}{\omega_o L_o} \tag{31}$$

where the subscript o indicates vacuum conditions. The vacuum losses must be subtracted from the observed losses to get the viscosity of the fluid. Using this idea and Eqs. (22), (30), and (31) gives:

$$\eta\rho = \left(\frac{M}{S}\right)^2 \pi f \left(\frac{R}{\omega L} - \frac{R_o}{\omega_o L_o}\right)^2 \tag{32}$$

Looking ahead, the frequency difference between vacuum resonance and fluid resonance is very small, with $\frac{\omega_o - \omega}{\omega} < 4 \times 10^{-4}$.

The difference in inductance is given by[29]

$$L - L_o = \frac{2(\omega_o - \omega)}{\omega} \tag{33}$$

Thus $\frac{L - L_o}{L} < 8 \times 10^{-4}$. The resistance change, however, is very large, since the crystal losses are small. Thus, Eq. (32) can be well approximated by:

$$\eta\rho = \frac{(M/S)^2 (R - R_o)^2}{4\pi f L^2} \tag{34}$$

The surface area and volume V of the crystal are given respectively by

$$S = 2\pi r\ell + 2\pi r^2 \tag{35}$$

$$V = \pi r^2 \ell \tag{36}$$

where r is the radius of the crystal

ℓ is the length of the crystal.

Combination of Eqs. (34), (35), and (36) yields:

$$\eta\rho = \left[\frac{\rho_q (R-R_o)}{4L}\right]^2 \left[\frac{1}{\frac{1}{r}+\frac{1}{\ell}}\right]^2 \frac{1}{\pi f} \tag{37}$$

where ρ_q is the density of the quartz equal to M/V.

The quality of the circuit, defined by Eq. (23), can also be defined as the ratio of the resonant frequency to the bandwidth of the resonance curve Δf [26]

$$Q = \frac{f}{\Delta f} \tag{38}$$

Combination with Eq. (23) yields

$$L = \frac{R}{2\pi\Delta f} \tag{39}$$

Substitution into Eq. (37) yields the final equation for the relationship of the viscosity of the fluid to the crystal properties:

$$\eta\rho = \left[\frac{\pi^{1/2} \Delta f \ \rho_q (R-R_o)}{2Rf^{1/2} (\frac{1}{r} + \frac{1}{\ell})} \right]^2 \tag{40}$$

It should be noticed that the crystal properties do not yield the viscosity directly, but the viscosity-density product.

In Appendix I, the pressure and temperature effects caused by the viscous wave are determined. In addition, calculations are made for various parameters, including the maximum velocity and amplitude of the crystal, the maximum shear stress and rate of shear, and the Reynolds number, which is seen to be in the laminar region.

B. Measurement of Resonant Properties

The equivalent circuit used to represent the oscillating crystal has been previously mentioned. The circuit, shown in Figure 4, consists of a series resonant RLC branch in parallel with a capacitor C' .

An impedance bridge, a frequency generator, and a null detector have been used to determine the resonant properties of the crystal. A schematic drawing of the bridge appears in Figure 5. Two adjacent arms of the bridge are composed of impedances equal at all frequencies; these arms are represented by Z_A and Z_B in Figure 5. The variable arm consists of a resistance R_N in parallel with a capacitance C_N . The crystal is connected across the fourth arm of the bridge; R_X and C_X represent the unknown parallel resistance and capacitance.

To determine the parameters measured by the bridge, consider the impedance of the variable arm consisting of R_B and C_B . The impedance Z_N is given by:

$$\frac{1}{Z_N} = \frac{1}{R_B} + \frac{1}{-j/\omega C_B}$$

$$Z_N = \frac{R_B - jR_B^2\,\omega C_B}{1 + (R_B\,\omega C_B)^2} \tag{41}$$

For later use, the real and imaginary parts of Eq. (41) are taken:

$$\text{Real}\ (Z_N) = \frac{R_B}{1 + (\omega C_B R_B)^2} \tag{42}$$

$$\text{Imag.}(Z_N) = \frac{-\omega C_B R_B^2}{1 + (\omega C_B R_B)^2} \tag{43}$$

Consider also the equivalent circuit of the crystal, as shown in Figure 4. The impedance of the series arm Z_S is given by

$$Z_S = R + j(\omega L - \frac{1}{\omega C}) \quad . \tag{44}$$

The impedance of the parallel arm Z_p is given by:

$$Z_p = - \frac{j}{\omega C'} \quad . \tag{45}$$

The total impedance Z_T is thus:

$$\frac{1}{Z_T} = \frac{1}{R + j(\omega L - \frac{1}{\omega C})} + \frac{1}{-j/\omega C'} \quad . \tag{46}$$

For convenience, let $(\omega L - \frac{1}{\omega C}) = a$, then:

$$Z_T = \frac{R - j(\omega C' R^2 + a^2 \omega C' - a)}{(\omega C' R)^2 + (a\omega C' - 1)^2} \quad . \tag{47}$$

The real and imaginary parts of Z_T are given by:

$$\text{Real}(Z_T) = \frac{R}{(\omega C' R)^2 + (a\omega C' - 1)^2} \tag{48}$$

$$\text{Imag.}(Z_T) = \frac{-(\omega C' R^2 + a^2 \omega C' - a)}{(\omega C' R)^2 + (a\omega C' - 1)^2} \quad . \tag{49}$$

When the bridge circuit is balanced, the variable arm of the bridge has the same resistance and reactance as the unknown (crystal) arm. Therefore, the real and imaginary parts of the unknown and variable impedances are respectively equal. Equating Eqs. (42) and (48) yields:

$$\frac{R_B}{1+(\omega C_B R_B)^2} = \frac{R}{(\omega C'R)^2+(a\omega C'-1)^2} \quad . \tag{50}$$

Equating Eqs. (43) and (49) yields:

$$\frac{\omega C_B R_B^2}{1+(\omega C_B R_B)^2} = \frac{(\omega C'R^2+a^2\omega C'-a)}{(\omega C'R)^2+(a\omega C'-1)^2} \quad . \tag{51}$$

Equations (50) and (51) can be solved simultaneously to give:

$$R_B = \frac{R[1+\frac{1}{R^2}(\omega C'R^2+a^2\omega C'-a)^2]}{(\omega C'R)^2+(a\omega C'-1)^2} \tag{52}$$

$$C_B = \frac{[\omega C'R^2+a^2\omega C'-a][(\omega C'R)^2+(a\omega C'-1)^2]}{R^2\omega[1+\frac{1}{R}(\omega C'R^2+a^2\omega C'-a)^2]} \tag{53}$$

with

$$a = \omega L = \frac{1}{\omega C} \quad .$$

Equations (52) and (53) represent the relationship between the crystal parameters and the bridge settings needed to balance the circuit. The "resonance curve" for a particular fluid state is actually the relationship between R_B and ω as given in Eq. (52)--not the crystal resistance R as is sometimes stated. The crystal properties do not change for a given fluid state.

The condition for series resonance is:

$$a = \omega L - \frac{1}{\omega C} = 0 \quad \text{at resonance} \; . \tag{54}$$

For this condition, Eqs. (52) and (53) reduce to:

$$R_B = R$$
$$\text{at resonance} \qquad (55)$$
$$C_B = C'$$

Thus, at resonance, the equivalent circuit of the crystal becomes simply a resistance in parallel with a capacitance (see Figure 4) with the two components measured directly by the bridge. The resonant resistance represents the lowest possible impedance of the series arm, and is equal to the minimum variable resistance necessary to balance the bridge.

For convenience, the capacitance C' can be found by balancing the bridge circuit when the crystal is far from resonance. For this condition $\left(a = \omega L - \frac{1}{\omega C} = \pm\infty\right)$ Eqs. (52) and (53) become:

$$R_B = \infty$$
$$C_B = C' \qquad (56)$$

Thus, far from resonance, the bridge is balanced with a pure capacitance C' which is equal to the parallel capacitance at resonance.

It is recalled from Eq. (40) that it is necessary to measure the bandwidth of the series resonant arm. The bandwidth is the width of the resonance curve between the half-power points[26], that is, the difference in frequency between the two balance points at which the power dissipated in the series arm is equal to one-half the power dissipated at resonance. The power dissipated is given by I^2R, where I is the current, given by

$$I = \frac{E}{|Z_S|} \qquad (57)$$

where E is the voltage applied

$|Z_S|$ is the absolute value of the series impedance.

The half-power points are thus the points at which the current is $1/\sqrt{2}$ times the current at resonance, and the absolute value of the impedance is $\sqrt{2}$ times the impedance at resonance, which is R. Thus

$$|Z_{S(h.p)}| = \sqrt{2}\, R \tag{58}$$

where $|Z_{S(h.p)}|$ is the absolute value of the series impedance at the half-power points. The series impedance is given in Eq. (44). Thus, at the half-power points,

$$|R + aj| = \sqrt{2}\, R$$

$$\sqrt{R^2 + a^2} = \sqrt{2}\, R$$

$$a = \pm R = \omega L - \frac{1}{\omega C} \quad . \tag{59}$$

The two solutions in Eq. (59) represent the two half-power points. For the conditions of Eq. (59), Eqs. (52) and (53) become:

$$a = +R \quad , \quad R_B = 2R$$
$$C_B = C' - \frac{1}{2\omega R} \tag{60}$$

$$a = -R \quad , \quad R_B = 2R$$
$$C_B = C' + \frac{1}{2\omega R} \quad . \tag{61}$$

Thus, the half-power frequencies can be found by balancing the bridge circuit with the variable resistance set at twice the resonant resistance. There are, of course, two balance points which are symmetrical,

as indicated in Eqs. (60) and (61).

III. EXPERIMENTAL METHOD

A. Apparatus

The quartz crystal was cut, polished, and plated by the Valpey-Fisher Corporation, Holliston, Massachusetts. The angle of cut was accurate to ±10 minutes of arc, and the "out-of-roundness" was less than 2×10^{-4}cm at the ends. This high precision is necessary to enhance the purity of the torsional mode of oscillation. Other investigators have found that there is a tendency for other modes of oscillation to be coupled with the torsional mode. Mason[15] noticed a ring-type oscillation in which one diameter is enlarged while the diameter 90^{o} away is contracted. Motion of this sort would tend to set up a complex longitudinal wave in the fluid, and interfere with the accurate measurement of viscosity, which is based on the torsional mode only.

Mason[15] suggested that a cell diameter only slightly larger than the crystal diameter would tend to inhibit the unwanted mode. It has also been postulated that a large length to diameter ratio for the crystal would tend to reduce non-torsional modes of oscillation, with a ratio of at least 10:1 necessary for reasonable accuracy[30]. It would seem, however, that other modes of oscillation would have to exist; by careful crystal preparation these other modes should be kept to a minimum.

The surface of the crystal (including the ends) has been polished so that there are no imperfections to considerably less than optical wavelengths (about 1.5×10^{-5}cm). The fine polish is extremely important

since the shear wave is so highly attenuated. The penetration depth, as previously mentioned, is about 6.7×10^{-5}cm for xenon in the critical region. The magnitude of the imperfections must be small with respect to the penetration depth, or else the shear wave would be disturbed.

The gold electrodes were placed on the crystal surface by a vacuum deposition technique. The electrodes are about 5×10^{-6}cm thick. The electrodes are carefully oriented so that the center line of each electrode makes a 45^{o} angle with the y-axis.

The quartz cylinder has a length of 5.000 ± 0.01 cm and a diameter of 0.2997 ± 0.004 cm. The dimensions of the quartz change less than 0.05% for the temperature and pressure conditions of the present investigation. The density of single crystal quartz is taken as 2.646 g/cm^3 at 25^{o}C [31].

Coming from the manufacturer, the quartz crystal had electrical leads and gold plating on the ends. These were removed by a combination of aqua regia and scraping with a tool. A very small section of the desired electrodes was inadvertently removed by this process. This area was resurfaced by brushing on a gold "paint", Hanovia Liquid Bright Gold (Type N), after carefully cleaning the area. The paint consisted of gold particles and a low melting point glass dispersed in an organic vehicle. After application, the paint was fired in a well-ventilated oven at 510^{o}C for one hour. This temperature was high enough to burn out the organic components and melt the glass; the residue formed an electrically conductive spot which adhered to the quartz. Good air circulation was necessary to

prevent the reduction of the lead borate in the glass to lead, which would tend to greatly reduce the adherence of the gold.

The crystal was then positioned lengthwise in a traveling microscope. The point on each electrode at which the center line crossed the longitudinal center was noted and marked. As mentioned previously, these are the points at which the leads should be attached.

Gold plating was removed by scraping from a small circular area around the marked positions. Hanovia type 122-A liquid silver was applied to the bare area, making certain that complete electrical contact was made with the gold electrodes. The silver paint, which was similar to the previously mentioned gold paint, was then fired to the crystal at 550^{o}C for one hour. It was found that the adherence of the silver to the bare quartz was superior to the adherence of the silver to the gold plating--this was the reason for scraping away some of the gold. The silver dots, which were about 0.1" in diameter, were burnished after being cooled down, to improve the quality of attachment of the electrical leads.

The electrical leads were phosphor-bronze wires, 0.008" in diameter. The end of each wire was flattened in a die, so that the diameter of the head was about three times the diameter of the wire. Wires headed in this manner were found to be more easily attached to the crystal.

A tin sphere was attached to each lead about 0.07" from the head. The spheres were used to "clamp" the wires, in case they had any tendency to oscillate with the crystal[32]. The leads were attached to nodes of the crystal oscillation, and should be basically

motionless. The tin spheres were about 0.1" in diameter and were attached to the phosphor-bronze wires by solidifying a dab of liquefied tin in the desired position along the wire. A schematic of the headed wire and tin sphere is shown in Figure 6 [32].

The wires were attached to the crystal by soldering to the burnished silver dots. The soldering operation was quite difficult and much care was necessary. The four phosphor-bronze wires acted not only as the electrical leads, but also as the only physical support for the crystal, and were thus stressed by the crystal weight. The whole success of the torsional crystal method rests on the stability of the bond between the leads and the crystal.

The heads of the wires were pre-tinned with a small amount of solder, which had a composition of 60% tin, 36% lead, and 4% silver. The silver in the solder was necessary to discourage migration of the silver in the dot to the solder during the soldering operation. Migration would tend to weaken the bond. The solder melts at 172°C, with a very narrow two-phase region. The melting point of the tin spheres, 222°C, is comfortably above the melting point of the solder.

It is desirable to limit the heating of the solder joint in order to reduce the silver migration. In addition, the quartz crystal itself can be affected by localized heating. It is known that quartz undergoes a transition from ambient α-quartz to high temperature β-quartz at 573°C. This transformation produces electrical twinning upon cooling, rendering the quartz unsuitable for viscosity measurements. However, twinning may occur at much lower temperatures if there is a large temperature gradient in the quartz[33]. In the operation of

firing on the gold and silver paint, care was taken to heat the quartz evenly and not to approach the transition temperature.

Since use of a soldering iron can result in large localized heating effects, it was decided to melt the solder with a stream of heated nitrogen gas. Nitrogen was passed over a heated nicrome wire filament inside a glass tube with a necked down outlet. The outlet temperature of the nitrogen was varied by changing the flow rate of the gas and the current through the wire.

A special crystal holder was fabricated to hold the quartz during the soldering operation. The holder had teflon cups, so as not to mar the quartz. The pre-tinned wires were positioned against the silver dots, and held there by the crystal holder. The crystal holder was then placed on a covered hot plate, and heated evenly to just below the melting point of the solder.

A soluble resin flux was then applied sparingly to the joints. No more solder was added as it was desirable to keep the amount of solder as small as possible. The hot nitrogen blast was then introduced, with the outlet temperature controlled to just melt the solder. The solder solidified on removal of the stream, completing the joint. Each of the four leads was soldered to the crystal by this procedure. After cooling, the resin flux was carefully removed with solvents. The plating and lead configuration can be seen in Figure 2.

The permanent crystal support consisted of four stainless steel strips and two soapstone rings as shown in Figure 7. The soapstone was fired at 950^{o}C after machining. The fired soapstone was checked for absorbency with argon at 1000 psia; no absorbency was noticed.

The crystal was removed from the temporary holder and supported with bent pipe cleaners. One stainless steel strip, attached to a soapstone ring at each end, was brought near the crystal, while one of the crystal leads was fed through a hole in the center of the strip. A conventional solder joint was made on the outside of the strip. The opposite wire was fed through a hole in the second strip, which had been screwed into the two soapstone rings. The wire was then soldered to the strip. The crystal cage was then rotated 90^{o}, the weight of the crystal now being supported entirely by the two attached wires. The last two steel strips were attached to the soapstone, and the wires soldered to the strips. The extraneous wires were then clipped off close to the joints. The length of phosphor-bronze wire between the tin sphere and the stainless steel strip was about 1/32".

The opposite stainless steel strips were electrically connected with two small metal lugs at one of the soapstone rings, as can be seen in Figure 7. The crystal and its support unit are shown in Figure 8. The crystal housing unit was attached to a stainless steel flange by screwing one of the soapstone supports into a protrusion on the flange. A picture of the flange is shown in Figure 9.

An electrical lead was attached to each of the electrode pairs by soldering the wires to pins which were connected to the opposite stainless steel strips. The leads were stranded copper wire (for flexibility) with teflon insulation, with an O.D. of 1/32". The other ends of the leads were attached to an electrical feed-through designed for high pressures. The feed-through was manufactured jointly by Caltech and the Hermetic Seals Corporation, Rosemead, California. The

feed-through consisted of a threaded stainless steel nut containing two drilled holes. Two ceramic beads, each containing a stainless steel pin, were fired into the drilled holes, resulting in a leak tight seal. The two copper wires were passed through a small opening in the flange and then soldered to the two pins on the feed-through. The flange opening acts as a passageway for the introduction of fluid into the pressure cell, described below.

The feed-through was then screwed into the back of the flange with a specially built torque wrench, and was sealed to the flange with a teflon gasket. External electrical wires were soldered to the open side of the feed-through. The wires pass through two tubes which exit to the atmosphere. The outside of the feed-through was sealed to a water-tight condition with a stainless steel plate and a neoprene gasket. The feed-through and back side of the flange are shown in Figure 10.

The external wires come up through two tubes and are connected to gold crimp connectors manufactured by Microdot, Inc., South Pasadena, California. The mated crimp connectors were soldered to two shielded coaxial cables. The cables were kept rigid by taping them to a lucite rod, covering the rod and wires with additional shielding, and clamping the assembly to a rigid body. The cables were finally soldered to General Radio connectors which can be plugged into a Wheatstone bridge circuit as has been discussed.

The crystal was housed in a cylindrical cell made of type 304 stainless steel. The cell was 4" long, with a 1" O.D., and a 0.718" I.D. Welded to the cell was a mating part for the flange. The seal

was effected with a teflon gasket and six long bolts. The cell and the crystal were oriented so that their cylindrical axes were parallel to the horizontal. The crystal-cell assembly is shown in Figures 11 and 12.

A 3/16" stainless steel tube was silver soldered to an opening at the top of the flange, as can be seen in Figure 9. This tube was connected to a small section of 1/8" stainless steel tubing which led to a valve. The valve was connected to a piping system as shown in Figure 13. The valves were all Whitey type 3NBS4-316, manufactured by the Whitey Research Tool Company, Emeryville, California. The valves have a ball tip made of chrome carbide, and a stainless steel seat. The valves are teflon packed, with the valve threads above the packing. Thus, no thread lubrication comes in contact with the fluid system.

All tubing was 1/4" O.D., 3/16" I.D. stainless steel. The fittings were stainless steel Swagelock, manufactured by the Crawford Fitting Company, Solon, Ohio. In the piping system were two "weighing bombs", to be known as weighing bomb 1 and weighing bomb 2. Both vessels were made of type 304 stainless steel. Weighing bomb 1 had a nominal volume of 10 cm^3, while weighing bomb 2 had a nominal volume of 75 cm^3. Both vessels had Swagelok fittings welded to their open ends with valves connected to the fittings. The other side of the valves were connected to fittings which had been machined to accept special solder/weld tube fittings, also supplied by Hoke, Inc. These fittings were of the "nose-cone" type and could be broken and resealed many times without failing. The special fittings have been silver soldered to the 1/4" tubing in the manifold system.

Weighing bomb 1 was used to determine the density of the sample in the cell. The vessel was immersed in a temperature bath along with the cell. Upon loading, the fluid in the cell was allowed to come to equilibrium with the fluid in the weighing bomb. Thus, a determination of the density of the fluid in the weighing bomb sufficed as a determination of the density of the fluid in the cell. This procedure is described in more detail in a later section.

Weighing bomb 2 had a two-fold purpose. It was used as a pumping station to facilitate the transfer of the fluid into the cell. It was also used to check the density determination and for any leakage out of the cell. This function is expanded upon in a later section.

The xenon storage cylinder was made of stainless steel, about 500 cm^3 in volume. The valve on the vessel was a standard diaphragm type manufactured by the Union Carbide Corporation. The valve was connected to the manifold system by means of a CGA-580 fitting. The ethane storage cylinder was similar to the xenon vessel, except that the valve outlet was CGA-350.

There were two types of pressure gauges in the system. It should be mentioned that accurate pressure measurements were not needed for the investigation; the gauges were used for convenience and protection. Gauges 1 and 3 were standard, clock-faced brass bourdon tubes, manufactured by Union Carbide Corporation. The stated accuracy of the gauges was 2% in the middle range and 3% at the ends of the scale, which went from 0 to 2000 psig. As a check, the gauges were calibrated against a precision pressure device, traceable to a high accuracy dead weight tester. The results of the calibrations are shown in Figures 14

and 15. Notice that the indicated pressure in psig was calibrated against the absolute pressure in psia.

Pressure gauge 2 was a high precision stainless steel optical bourdon tube capsule, manufactured by Texas Instruments, Inc., Houston, Texas, model number 141. Very simply, a very light mirror is attached to a coiled bourdon tube which is strained upon application of a pressure. The pressure is related to the displacement of the mirror, which is measured by a relatively simple optical system. The capsule used has a nominal pressure range of 0-1000 psig. The gauge and capsule have been calibrated by the manufacturer against a dead weight tester. The calibration table is reproduced as Table I.

The manifold system was mounted on a lucite plate, which could be raised and lowered easily. This enabled the cell and weighing bomb 1 to be taken out of the temperature bath when necessary. The cell rested in a lucite support block, which was attached through an aluminum frame to the main lucite plate. Thus, the cell was externally supported, and did not stress the steel tubing. In addition, all of the valves had external supports so that the torque from opening and closing did not stress the manifold. The system was pressure tested and found leak tight at 1500 psig. Before use, the crystal, cell, and tubing were carefully cleaned with solvents, both before and after assembly.

The high pressure system was connected through a valve to a vacuum system. The vacuum system consisted of a high vacuum oil diffusion pump, a liquid nitrogen cold trap, and a General Electric

thermocouple vacuum gauge, catalog number 5797633G1. The gauge had an adjustable current setting and a range of 1 to 1×10^{-3} torr.

The Wheatstone bridge circuit has been previously mentioned (see Figure 5). The main component was a General Radio type 1615A capacitance bridge. The bridge has a digital readout of capacitance from -1.1×10^{5}pf to 1×10^{6}pf, the smallest division being 10^{-5}pf. The bridge has a stated accuracy of ±0.03% in capacitance at the conditions of the experiment. The losses in the capacitors are negligible and they can be considered as pure capacitors.

Connected in parallel to the variable capacitance arm of the 1615A bridge was a General Radio type 1432M decade resistance box. As connected, the resistance box has a range of 0 to 1.1×10^{6}ohms, the smallest division being 1 ohm. The resistors have a stated accuracy of ±0.025% in the range used, and are basically independent of frequency. As connected, the shunt capacitance of the resistance box is about 2 pf, which becomes part of the tuning capacitance. The parallel capacitance of the crystal at resonance is about 12 pf. It is not necessary, however, to know this value accurately.

The voltage generator was a Hewlett-Packard type 5102A frequency synthesizer, with digital selection of frequency. The range is 0 to 10^{6}Hz, the smallest division being 0.01 Hz. The stated stability of the synthesizer is on the order of two parts in 10^{10}. As connected, the voltage across the unknown arm of the bridge can be varied continuously from 3×10^{-4} to 1 volt.

There were two null detectors used. The primary device was a Tektronix type 531 oscilloscope with a type E low level differential plug-in. The oscilloscope has a maximum gain of 50 μvolts/cm. The back-up null device was a General Radio type 1232A tuned amplifier and null detector. The detector has a sensitivity of about 1 μvolt full scale at maximum gain.

The temperature coefficients for all of the above equipment are negligible for the conditions in the laboratory, i.e., $\pm 1^{o}C$.

B. Temperature Measurement and Control

The temperature of the cell and weighing bomb were controlled by a water thermostat. The bath was a double-walled glass vessel with a high-speed stirrer and a 900 watt quartz heating element. The vessel was actually a Tamson model TVM 40 temperature bath, manufactured by P.M. Tamson, N.V. Zoetermeer, Holland. However, the temperature controller supplied with the bath had been disconnected and only the stirrer and heater were used. The vessel was covered with a lucite plate.

Cooling water was circulated through coils in the bath by an auxiliary temperature bath and pumping station. The auxiliary bath consisted of a Tamson model T3 circulation thermostat used with a Tamson model PBC-4 portable bath cooler. The temperature in the circulation thermostat was regulated by means of an on-off mercury contact relay which activated a 900 watt quartz heater. The flow rate remained relatively constant, while the temperature of the cooling water was regulated to within $\pm 0.02^{\circ}C$.

The control system used was based on a Wheatstone bridge type circuit. The main component of the circuit was a Leeds and Northrup Mueller bridge, catalog number 8067. The bridge consisted of two equal arms (500 ohms), an arm containing a variable resistance, and an arm across which a platinum resistance thermometer (from Leeds and Northrup) is connected. A schematic of the circuit is shown in Figure 16.

The thermometer was connected to the bridge in a three-lead set up. Two of the leads, L_1 and L_2, were of equal resistance. The platinum element was encased in a glass bulb containing helium at

slightly above atmospheric pressure. The nominal ice-point resistance of the thermometer is 25.5 ohms. The thermometer was protected by a special stainless steel case.

The thermometer was immersed in the water bath along with the cell. A difference in resistance between the thermometer in the bath and the variable arm of the bridge produces an unbalanced condition in the bridge, which is sensed by a control unit. The controller has proportional, reset, and rate response. The unit consisted of Leeds and Northrup equipment--a Series 60 control unit, a microvolt indicating amplifier catalog number 9835B, and a speedomax H recorder. The output of the recorder is fed to the quartz heating element in the primary temperature bath.

A 12 ohm resistor was switched in series with the quartz heater when the unit was on control. This reduced the current in the circuit so as not to overpower the controller. The quartz heater had a maximum output of about 100 watts for this set-up. For rapid heating the resistor was switched out of the circuit, and the heater operated at full power, i.e., 900 watts.

The voltage to the bridge was supplied by a six volt Exide lead-acid battery. The current across the platinum element was about 12 ma. The large current was necessary for increased sensitivity.

In practice, the desired temperature was "dialed in" to the variable resistance (the correct value being known from experience) and the temperature in the water bath was controlled so that the resistance of the platinum thermometer was equal to the resistance of the variable resistor; this balances the Wheatstone bridge circuit.

The temperature of the water bath can be controlled to within $\pm 0.001^{\circ}C$ for periods of up to an hour, depending on the changes in temperature of the Mueller bridge. Temperature variation with position in the bath is less than $\pm 0.001^{\circ}C$.

The actual bath temperature was measured with a platinum resistance thermometer, separate from the control thermometer. The thermometer is model number G-20, manufactured by Electric Thermometers, Inc., Kearny, New Jersey. The element consisted of a doped platinum wire that was wound on a glass core and covered with a thin layer of glass. The thermometer was approximately 25 mm long and 2 mm in diameter and had a nominal ice point resistance of 100 ohms. The element had two platinum leads available for external connection.

The thermometer was housed in a tight fitting copper tube with silicone oil used to fill up the air spaces in order to improve the thermal contact. The copper well was screwed into a long thin-walled stainless steel tube. Four copper wires with varnish insulation, 0.01" O.D., were soldered to the thermometer element, with two wires attached to each lead. The copper wires were drawn out through the stainless steel tube and were connected to a shielded cable which went to the temperature measuring device. The stainless steel tube was partially immersed in the temperature bath, the immersion depth being great enough to limit heat conduction through the tube to the atmosphere.

The resistance of the thermometer was determined with the circuit shown schematically in a somewhat simplified form in Figure 17. The potentiometer used was a Leeds and Northrup six-dial guarded

potentiometer, catalog number 7556. For the scale used the potentiometer can measure voltages from 0 to 1.6 volts in steps of 1.0 μvolt. The stated accuracy is ± (0.003% + 0.1 μvolt). The potentiometer was driven with battery B_1 which was a 2-volt Exide lead-acid battery. The null detector was a Hewlett-Packard 419A DC null voltmeter, with a minimum range of 3 μvolts half-scale. This instrument was found to be quite adequate for high accuracy temperature measurements, and precluded the use of a much more delicate galvanometer.

Variable resistor R_1 was a Leeds and Northrup Mueller bridge, catalog number 8067, which had been modified so as to act as a very precise decade resistance box. The range of the resistor is 0-80 ohms in steps of 0.001 ohm. The resistor was connected so as to replace the trimmer adjustments in the potentiometer, which had been found to be inadequate.

The standard cell was unsaturated, with a voltage of 1.01929 volts and a drift rate of less than 100 μvolts per year. The cell was supplied by Eppley Laboratory, Inc., Newport, Rhode Island, catalog number 100. The standard cell was used to adjust the potentiometer so that the potential differences were given in actual volts. This is accomplished by nulling the detector with the standard cell switched in and the potentiometer dials set at 1.01929 volts. Variable resistor R_1 was used to achieve the null.

It is possible to determine the resistance of the thermometer without standardization, since the resistance is calculated from a ratio of voltages as is shown below. However, it is felt that standardization is quite worthwhile, since it acts as a check on the

battery drift and the general operation of the potentiometer circuit. The standardization was performed before each complete temperature measurement.

In the thermometer part of the circuit, variable resistor R_2 was a Leeds and Northrup decade resistance box, catalog number 4775, with a range of 0-10,000 ohms in steps of 1 ohm. Battery B_2 was a two volt Exide lead-acid battery which provided current to the circuit. The platinum resistance thermometer is shown as PRT.

The standard resistor was supplied by Leeds and Northrup, catalog number 4030B; as connected, the stated value of the resistance is 100.00036 ± 0.001 ohms at $25.0^{\circ}C$. It was determined by comparison with a similarly constructed resistor that a better value for the resistance at $25.0^{\circ}C$ is given by 99.99948 ohms, which is within the accuracy limits given by the manufacturer. It is not necessary to know the value of the standard resistor to the greatest accuracy, as long as the same resistor is used in measuring the ice point resistance of the thermometer as is used for the temperature measurements. The stability of the resistor must be good, however, and the temperature dependence must be known very precisely. Leeds and Northrup gives the temperature dependence of the resistor as:

$$R_t = R_{25}[1 + 0.000004(t-25) - 0.0000006(t-25)^2] \qquad (62)$$

where R_t is the resistance at temperature t ($^{\circ}C$)

$R_{25} = 99.99948$ ohms.

Values of R_t as a function of temperature as calculated from Eq. (62) are given in Table II in steps of $0.05^{\circ}C$. The range in

temperature represents the possible range for the ambient temperature.

As can be seen in Figure 17, the potentiometer can be switched to measure the voltage drop across either the PRT or the standard resistor.

Temperature determinations using resistance thermometry are based on the ratio of the resistance of a platinum wire at the temperature of interest to its resistance at the ice point R_t/R_o . The resistance of the thermometer is equal to the ratio of the voltage drop across the thermometer E to the current in the circuit I . The current is determined by measuring the voltage drop across the standard resistor, and dividing that by its resistance at the measured temperature of the resistor, as given in Table II. Thus,

$$\frac{R_t}{R_o} = \frac{E_t/I_t}{E_o/I_o} \tag{63}$$

It was necessary to correct for thermal or stray voltages which may exist in the circuit. These were determined by measuring the "zero-current" voltages in both the thermometer and standard resistor circuits. These voltages (which are quite small but not negligible) were used as the zero reference for the temperature measurements.

The measurement procedure was as follows. First, the zero-current reference point was determined followed by the balancing of the potentiometer against the standard cell. The voltage drop across the standard resistor was then measured followed by the voltage drop across the thermometer and the standard resistor again. The two voltage drops across the standard resistor were averaged if they

differed. The temperature of the standard resistor was then measured with a mercury glass thermometer placed in a special temperature well in the resistor.

It can be assumed that the potentiometric errors are related to the differences in the voltages measured. The ratio of two similar voltages should be very precise, while the ratio of two very different voltages will have a much larger error. Consider Eq. (63) rearranged as follows:

$$\frac{R_t}{R_o} = \frac{E_t/E_o}{I_t/I_o} \tag{64}$$

The currents I_t and I_o represent two different current determinations, one performed as part of the temperature measurement, and the other as part of the ice point determination. To reduce potentiometer errors, the standard resistor voltage drops were always adjusted to the same value, with the use of the decade resistance box R_2. The current used in the circuit was about 1 ma. Thus, the potential drop across the standard resistor was about 0.1 volt. In practice, the decade resistance box can alter the voltage by as little as 50 μvolts, and the standard resistor voltage was adjusted to within 50 μvolts of 0.1 volts for each measurement. The voltage was not set at a value below 0.1 volts, since that would result in altering all of the potentiometer dials, thus defeating the idea of the adjustment. With this procedure it is felt that the ratio I_t/I_o is very precise and introduces a negligible error in the temperature determinations.

Thus, the potentiometer error shows up in the voltage ratio E_t/E_o. The standard resistor has been chosen so that E_o is very

close to, but greater than 0.1 volt. Therefore, the measurement of E_t results in the least possible changing of the potentiometer dials. By choosing the value of the standard resistor to be very close to the resistance of the thermometer at the ice point, the ice point determinations are free of potentiometer errors, and are limited only by the accuracy of the standard resistor.

It can be easily seen that the most accurate temperature measurements are for those temperatures closest to the ice point. By following the above procedure, the potentiometer errors can be kept to less than $\pm 0.001^{\circ}C$ at $30^{\circ}C$.

As a byproduct of the careful control of the voltage drop across the standard resistor, the current in the thermometer is automatically adjusted to be very close to 1 ma which, as is shown below, is the current used for calibration. Thus there were no extraneous heating effects in the thermometer to worry about.

The ice point resistance of the thermometer has been measured a number of times and has a best value of 100.00542 ± 0.0003 ohms. The ice baths were carefully constructed from distilled water and ice and were not stirred. The precision in the resistance measurement is equivalent to $\pm 0.0007^{\circ}C$.

The temperature dependence of the resistance of platinum varies somewhat from thermometer to thermometer. Thus, for high accuracy measurements, it is always necessary to calibrate the thermometer to be used. The present thermometer was calibrated with two platinum resistance thermometers having calibration certificates from the National Bureau of Standards. The calibration was performed in the

same temperature bath as was used in the experiment, with the measurements taken in the manner prescribed above.

The standard thermometers had a nominal ice point resistance of 25.5 ohms and the NBS certificate specified a current of 2 ma as compared to the 1 ma for the measuring thermometer. Thus it was necessary to use another standard resistor (also from Leeds and Northrup) which had a given resistance of 49.99996 ±0.001 ohms at 25°C. The temperature dependence of the resistor is given by:

$$R_t = R_{25}[1 - 0.000002(t-25) - 0.0000005(t-25)^2] \quad . \qquad (65)$$

The calibration procedure was as follows. First the ice point resistances of the standard thermometers were determined. Since the thermometers were glass enclosed, it was found necessary to place an opaque shield on the ice bath vessel, to protect the thermometers from radiation effects.

Two calibration temperatures were used, 13.07°C and 30.34°C. At these temperatures the resistance of the thermometer to be calibrated was measured. The actual temperature was determined with the two standards, which agreed to better than ±0.001°C.

The temperatures as determined by the standard thermometers are on the 1948 International Temperature Scale (ITS)[34]. That scale measures temperature as a function of the resistance of platinum for the region of interest as follows:

$$R_t = R_o(1 + At + Bt^2) \qquad (66)$$

where t is the temperature in °C, and A and B are constants.

Equation (66) can be rearranged to give:

$$t = \frac{R_t - R_o}{\alpha R_o} + \delta\left(\frac{t}{100} - 1\right)\left(\frac{t}{100}\right) \qquad (67)$$

where α and δ, the Callendar constants, are given for each standard thermometer by the NBS calibration certificate.

Using Eq. (67), the temperatures at the two calibration points were determined from the measurement of R_o and R_t for the standard thermometers; as mentioned above, the calculated temperatures agree to better than $\pm 0.001^{o}C$ for the two standards.

To calibrate the measuring thermometer, it is assumed that its resistance follows a relationship similar to Eq. (66), even though the element is doped rather than pure platinum. The range of the calibration is small, and the assumption is probably fairly accurate. Equation (67) can be further rearranged as

$$\frac{R_t}{R_o} = 1 + \alpha(1 + \delta \times 10^{-2})t - \alpha\delta \times 10^{-4} t^2 \qquad (68)$$

Using the values of t measured with the standard thermometers and the measured resistances of the doped thermometer, the effective Callendar constants for the thermometer can be determined by solving the two simultaneous equations resulting from the two calibration points. The Callendar constants for the measuring thermometer were calculated to be:

$$\alpha = 0.003857118$$

$$\delta = 1.45566 \qquad (69)$$

Using these values, a calibration table was calculated and is shown in Table III. It can be seen from the difference column that a linear interpolation within $1^{o}C$ should be quite accurate.

As a check, a third temperature was measured, using the two standard thermometers and the measuring thermometer as calibrated. This check at $22.16^{o}C$ showed the temperature as determined by each of the three thermometers agreeing to within $\pm 0.001^{o}C$.

The overall uncertainty in a temperature measurement is estimated to be $\pm 0.003^{o}C$ with respect to the 1948 International Temperature Scale. The precision of a temperature measurement is better than $\pm 0.001^{o}C$. The sensitivity of the thermometer circuit is about $\pm 0.0003^{o}C$.

Although temperatures were measured on the 1948 ITS, they are reported in degrees Celsius on the 1968 International Practical Temperature Scale (IPTS). It should be mentioned that these temperature scales are not "absolute" scales, but are "experimental" scales designed to be updated as temperature measuring technique is improved. A table presented by the Comité International des Poids et Mesures[35] gives the relationship between the 1948 ITS and the 1968 IPTS. The table is presented as corrections to the 1948 scale and is shown in graphical form for the region of interest in Figure 18. The corrections are $0.01^{o}C$ or less and are expected to be accurate to better than $\pm 0.001^{o}C$.

C. Density Measurements

As previously mentioned, the density in the cell was determined by the use of a weighing bomb containing fluid in equilibrium with that in the cell. For the calibration and density measurements, weights were determined with an Ainsworth analytical balance, type DLB. The set of masses used for the weighing were class S-2 stainless steel manufactured by the Christian Becker Company, New York City, which had been calibrated against a set of class S stainless steel masses with a National Bureau of Standards calibration certificate.

The calibration procedure was as follows. For each mass to be calibrated, the analytical balance was brought to a balance point by matching the mass with a standard mass of the same nominal value. The masses were then reversed and the balance was brought to the same rest point by adjustment of the balance chain. With this method, known as transposition weighing, the calibration was basically independent of the balance used. The mass was determined by taking the square root of the product of the two determinations[36].

The NBS certificate for the standard masses gives apparent mass as measured against brass at an air density of 1.2 mg/cm^3. A correction must be applied to account for the difference in air buoyancy of stainless steel and brass. The buoyancy correction is of the form:

$$M_V = M_A\left(1 - \frac{\rho_A}{\rho_m}\right) \tag{70}$$

where M_V is the true mass (in vacuum)

M_A is the apparent mass in air

ρ_A is the density of air

ρ_m is the density of the mass being weighed.

The variation in the air density for normal ambient conditions introduces a variation of less than 4 ppm in the apparent mass of stainless steel or brass. Since this variation is smaller than the accuracy of the NBS calibration certificate, an average value for air density is used. The buoyancy correction is 150 ppm for stainless steel and slightly less for brass.

With the above procedure the masses of the set being calibrated were determined as actual mass. In use, the air buoyancy correction for stainless steel must be applied. In addition, the analytical balance chain had been calibrated against the standard masses. The results of the calibration are shown in Table IV (for the masses) and Figure 19 (for the chain).

The actual weighings were performed by a substitution method using a tare heavier than the weighing bomb and its contents. The substitution method worked as follows. A tare of known mass was placed on the left pan of the balance. The weighing bomb was placed on the right pan and masses were added to it until the scale was balanced. After the buoyancy corrections were made, the mass of the weighing bomb was determined by subtracting the mass added to the weighing bomb from the mass of the tare. Since the same tare was always used, the weighings were always done at the same load. Thus, errors due to beam bending or lever arm inequalities were eliminated.

Since it was desired to know the mass of the contents of the weighing bomb, the empty mass of the vessel had to be determined and subtracted from the loaded weight. The empty masses were determined

with the weighing bomb evacuated to better than 5×10^{-3} torr. In practice, the empty masses were determined prior to each mass determination. This kept track of any possible physical changes in the vessel.

Since the same tare was used to determine both the loaded and the empty mass, the weight of the tare did not need to be known, as it canceled out. The weighing bomb, of course, is much less dense than the masses, so that the buoyancy corrections become more important. The change in air density between an empty weighing and a loaded weighing can result in a significant variation in the apparent mass. Thus, a calculation of the volume of the weighing bomb and a determination of the air density for each weighing would be required.

In the present experiment, the tare used was a weighing bomb identical in dimensions to the working vessel. The tare was filled with scrap metal to make it somewhat heavier than the weighing bomb and contents. Thus, the buoyancy corrections for the tare and the weighing bomb cancel for any and all weighings. The only buoyancy corrections necessary were for the stainless steel masses needed to balance the weighing bomb with the tare. As previously mentioned, an average air density can safely be used for the stainless steel buoyancy correction.

Prior to all mass determinations, the weighing bomb was placed in an evacuated bell jar for one hour, in order to remove any surface moisture from the temperature bath. After removal from the bell jar the vessel was equilibrated with the atmosphere for at least one hour.

The volume of the weighing bomb was determined by calibrating with distilled water as follows. The bomb and transfer lines were

evacuated to at least 2×10^{-2} torr. Any dissolved air was removed from the water by vacuum boiling. The water was then drawn into the weighing bomb by opening a valve between the evacuated manifold and the water source. Care was taken so that no air was allowed to enter the system. The weighing bomb was lowered into the thermostat and brought to the desired calibration temperature. For atmospheric measurements, the manifold was left open to the air. For high pressure measurements, the water was compressed with dry nitrogen, it being assumed that the nitrogen did not diffuse through the water in the manifold and result in any appreciable concentration in the weighing bomb. The pressure was measured with pressure gauge 1 (see Figure 13), the accuracy of which was quite sufficient for the highly incompressible water. When the water was equilibrated with the temperature and pressure, the valve on the weighing bomb was closed. The bomb was removed from the system and weighed.

Using the empty weights, the mass of water in the weighing bomb at various conditions can be determined. The volume of the weighing bomb at the various states can be determined by using the accurate water PVT data of Kell and Whalley[37]. The results of the calibration are presented in Table V. Figure 20 shows the volume of the bomb as a function of pressure at 30°C.

As can be seen, the variations in the weighing bomb dimensions with temperature and pressure are quite small and can almost be neglected. However, corrections are used so that the density determinations are of the highest possible accuracy. The volume changes 0.0759% between 10°C and 30°C. Assuming a constant volumetric expansion

coefficient, its value would be $3.8 \times 10^{-5}/^{o}C$. This was assumed to be the expansion for the temperature range from $10^{o}C$ to $50^{o}C$. The value for the linear coefficient of thermal expansion for 304 stainless steel is given in the Stainless Steel Handbook[38] as $8 \times 10^{-6}/^{o}F$. Assuming that the coefficient of volumetric (cubical) expansion is three times the coefficient of linear expansion, the volumetric expansion becomes $4.3 \times 10^{-5}/^{o}C$, quite close to the measured value. The measured value of $3.8 \times 10^{-5}/^{o}C$ was used.

Assuming that the coefficient of volumetric expansion is independent of pressure, the volume of the weighing bomb for any loading conditions can easily be determined with the help of Figure 20. Thus the density in the weighing bomb and cell can be determined for any loading.

The dimensions of the cell, however, change with temperature and pressure. The gaskets and other "squashy" parts of the cell were of very small volume in comparison with the total cell volume (about 23 cm^3). Thus it is the change in volume of the stainless steel that is of interest. The cell is basically of the same design as the weighing bomb, i.e., a thin-walled 304 stainless steel cylinder. It was assumed that the volume changes in the cell were analogous to those in the weighing bomb.

For the temperature dependence, the measured volumetric expansion of $3.8 \times 10^{-5}/^{o}C$ is used directly, as it is properly a material function.

The pressure dependence is a more difficult problem. Fortunately, the pressure effect is very small, almost negligible for the

conditions of the present experiment. However, corrections can be made. As is seen below, the cell is closed during the viscosity measurements so the pressure cannot be measured. However, the pressure can be estimated from existing PVT data. Even a rough estimate is quite sufficient.

Consider the equation for the circumferential strain for a thin-walled cylindrical vessel, neglecting end effects[39]

$$\varepsilon = \frac{PR}{tE} \tag{71}$$

where ε is the circumferential strain

P is the internal pressure

t is the wall thickness

R is the mean radius of the cylinder

E is the modulus of elasticity for the material.

The change in volume can be seen to be proportional to $(R/t)^2$ for a given pressure.

For the weighing bomb $R = 0.281"$, $t = 0.0621"$, $(R/t)^2 = 20.54$.

For the cell $R = 0.430"$, $t = 0.141"$, $(R/t)^2 = 9.30$.

From Figure 20 it can be calculated that the average value for the "compressibility" of the weighing bomb is 5.13×10^{-7}/psia. The "compressibility" of the cell is assumed to be equal to

$$\frac{9.30}{20.54} \times 5.13 \times 10^{-7}/\text{psia} = 2.3 \times 10^{-7}/\text{psia} \quad .$$

With this information, the density in the cell can be computed for any

given conditions as follows:

$$\rho(T,P) = \rho_{LD}[1 + (2.3 \times 10^{-7})(P - P_{LD}) + (3.8 \times 10^{-5})(T - T_{LD})] \qquad (72)$$

where $\rho(T,P)$ is the density in the cell at any temperature and pressure

the subscript LD indicates loading conditions

P is the pressure in psia

T is the temperature in ^{o}C.

The density at loading was determined by closing the weighing bomb valve at loading, determining the mass of fluid in the bomb by the previously described gravimetric techniques, and calculating the volume of the bomb at the loading conditions. The density corrections given in Eq. (72) are quite small for the conditions of the present experiment; they were usually less than 0.06%.

One point worth considering is the density change caused by closing the valves. The valve stems have a finite, if small, volume and this changes the density of a fixed mass when introduced into the system upon closing a valve. In the operation of loading the cell, both the cell valve and the weighing bomb valve must be closed. Great care must be taken that the two valves are closed simultaneously, otherwise the fluid in the cell would be at a different density from the fluid in the weighing bomb.

The overall absolute accuracy of the density for a given state is estimated to be no worse than ±0.1%.

D. Vacuum Measurements

As previously mentioned, it was necessary to measure the resonant resistance of the crystal in a vacuum so that a correction could be made for the background losses. The vacuum resistance is dependent upon the temperature. The measurements were taken for an applied voltage of 1.0 volt across the crystal, the same voltage as was used for the fluid measurements. The data are shown in Figure 21 for the temperature range of interest; they were taken under a vacuum of about 10^{-3} torr. Naturally, the vacuum resistance at the temperature of the fluid state was used as the correction. The vacuum resonant frequency varies from about 38,781 Hz at the low temperatures to about 38,787 Hz at the high temperatures. The equivalent parallel capacitance is basically constant for all temperatures at 11.25 pf.

It should be realized that the vacuum corrections are only approximations for the inherent crystal losses which exist when the crystal is oscillating in a viscous medium. At vacuum resonance, the resistance is much lower than at fluid resonance; hence the amplitude of oscillation and the crystal power are much larger. It is much more difficult to dissipate any heat energy since a vacuum is a poor conductor. It has, in addition, been found that the apparent vacuum resonant resistance increases with the applied voltage, while the fluid resonant resistance does not.

Thus, it is not clear to what extent the vacuum measurements correct for the real crystal losses. It seems reasonable to assume, however, that the real losses are not going to be larger than the measured vacuum resistance at 1.0 volt, since this voltage seems to be

equivalent to a much higher voltage for fluid measurements.

At 30°C, for example, the vacuum resistance for 1.0 volt is about 2580 ohms. This is equal to about 6% of the resonant resistance of carbon dioxide, 3% of the resonant resistance of xenon, and 10% of the resonant resistance of ethane.

Vacuum resistance measurements were taken before each run to check on the consistent operation of the crystal.

E. Procedure for a Measurement Run

The vacuum gauge facilitated static vacuum tests, for which the build-up in pressure was monitored as a function of time. There seemed to be no evidence of any leaks, so the build-up in pressure was associated with the degassing of the metal surfaces in the cell and manifold. The xenon or ethane used remained in the cell for an entire run, which often took as long as two weeks. It was thus necessary to determine whether the degassing over this period of time would seriously affect the purity of the sample.

The worst case for the loaded cell would seem to be a constant degassing rate over the full two weeks, equal to the short term degassing rate into a vacuum. The degassing rate in the cell seemed quite large, but was equivalent to a rate which would add less than 50 ppm impurities over a two week time. This was equivalent to a pressure build-up of 0.36 torr/day.

The fluids were not discarded after use; rather they were returned to the storage vessel and mixed with the stored fluid. The next sample was then taken from the contents of the storage vessel. This procedure introduced two purity problems. First, the storage vessel itself must have a small degassing rate. The storage vessels were stainless steel and the fluids were transferred into these vessels from their original vessels. The vessels had a degassing rate of less than 0.01 torr/day. For the worst case this would introduce less than 15 ppm impurities for a forty week storage time.

Of course, these numbers represent the very worst possible case for degassing. The degassing rate undoubtedly decreases, if not with

pressure then surely with time (as the degassed material gets used up). Care was taken never to open the cell to the atmosphere. After some time, the cell degassing material could probably be assumed to be the fluid in use, thus not affecting the purity. The degassing rates were much too small to affect any density measurements.

In addition, the fluid in the storage vessel was rid of noncondensable material by freezing the fluid with liquid nitrogen and removing the vapor with the vacuum pump. This operation was performed before each run.

The degassing of the piping lines was insignificant since the fluid was in contact with the lines only during the short transfer time.

The cell and weighing bomb 1 were loaded as follows. The cell and bomb were lowered into the thermostat and the temperature controlled to a pre-set value. This value was either 25°C or 30°C for xenon, 100°F (37.778°C) or 110°F (43.333°C) for ethane, and 35°C for carbon dioxide. The vacuum system was closed off and the storage tank opened to the system. Mass was transferred into the cell by two techniques. For the xenon, weighing bomb 2 (see Figure 13) was used as a transfer vessel. The xenon from the storage tank was condensed into weighing bomb 2 with liquid nitrogen. The storage vessel valve was closed and the xenon in the weighing bomb was allowed to heat up, thus building up the pressure in the cell. For ethane and carbon dioxide, the storage tank was simply heated with hot water to increase pressure.

The pressure was measured with the precision pressure gauge 2. The PVT data of Michels, et al.[40] for xenon, Reamer, et al.[41] for

ethane, and Michels and Michels[42] for carbon dioxide were used to determine the pressure necessary to give the desired density for the run. The loading pressure was always super-critical so that there was no difficulty with two phases during the loading.

When the system was equilibrated at the desired pressure, the valves on the cell and weighing bomb were carefully closed, as described previously. A valve on the manifold was adjusted to keep the pressure constant and to correct for room temperature changes.

The fluid in the lines was condensed back into the storage vessel with liquid nitrogen. After ascertaining with the vacuum gauge that the cell and weighing bomb valves were indeed closed, the weighing bomb was removed from the system and the loading density determined by the previously described method.

The viscosity was measured at decreasing temperatures along the isochore. For each temperature the "actual" density was determined using Eq. (72) and the above-mentioned PVT data. At least two hours were allowed for the system to reach equilibrium after a change of temperature. The viscosity measurement was repeated in an hour, and the data accepted only if the two values agreed to within 0.1%, as was almost always the case. The voltage to the crystal was applied only during a measurement and was turned off at all other times.

As has been mentioned before, the viscosity measurement requires the determination of the lowest resistance which balances the bridge circuit. To find this resistance, the parallel capacitance was found by balancing the bridge against an infinite resistance, achieved by disconnecting the resistance box, at frequencies far above and far

below the resonant frequency. The two capacitance values, which differed slightly, were averaged and dialed into the bridge. The resistance and the frequency were then varied until a bridge balance was achieved.

The capacitance was varied slightly to see if a lower resistance could balance the bridge. The minimum resistance was taken as the resonant resistance. The bridge was then set at twice the value of the resonant resistance, and the two half-power balance points were found by adjusting the frequency and capacitance. The half-power frequencies and effective capacitances are basically symmetrical around the resonant values.

After completion of the isochore, the fluid in the cell was transferred to weighing bomb 2 by condensing with liquid nitrogen. Weighing bomb 2 was removed from the system and was weighed by a method identical to that previously described except that a different analytical balance was used since weighing bomb 2 is larger than weighing bomb 1. The balance used had a nominal 2000g capacity, and was manufactured by Christian Becker Inc. The accuracy of the balance was not as good as the smaller balance (nominal 200g). The empty mass of weighing bomb 2 was measured before each run, thus the loaded weighing yielded the mass of fluid in the cell, assuming that all material had been transferred (the vapor pressure of both xenon and ethane at liquid nitrogen temperatures is negligible on a mass basis). Using the previously determined density, the volume of the cell was calculated and reduced to some standard condition. This volume was computed for each isochore, and acted as a check on the density

determination and any possible cell leakage. The cell volumes calculated by this method agree to ±0.1% from a mean value. This does not affect the stated density accuracy, since the precision of the large analytical balance is poor and probably equivalent to almost 0.1% of a density measurement.

After weighing, the bomb was reconnected to the manifold, and the fluid, along with the fluid from weighing bomb 1, was transferred back to the storage vessel. Prior to the next isochore, the empty weights of the two weighing bombs were determined and the fluid was purified of noncondensables by the method previously mentioned.

F. Sample Work-Up of Data

Take, for example, xenon isochore VI (see Table IX). First the empty masses of the two weighing bombs were determined.

Weighing bomb 1

Weights used: 10, 5, 1 g

Balance chain: 37.7 mg

From Table IV, weight of masses = 16-0.0001-0.0002-0.0002 = 15.9995 g

weight in vacuum = (15.9995)(0.99985) = 15.9971 g

From Figure 19, weight of chain = 0.0377 + 0.0003 = 0.0380 g

total weight in vacuum = 15.9971 + 0.0380 = 16.0351 g

Weighing bomb 2

Weights used: 50, 20, 5, 2, 1 g

200, 100, 100* mg

Rider at -14.8 mg

weight of masses in vacuum = (78.4000 - 0.0013)(0.99985)

= 78.3870 g

total weight in vacuum = 78.3870 - 0.0148

= 78.3722

Vacuum resistance check at 25°C, R_o = 2530 ohms

Cell and manifold were loaded with xenon; cell was at 25°C. Pressure gauge #2 was used to measure and control the pressure. Reading of gauge was 204.900; vacuum reading was 0.386; the difference was 204.514. From Table I, this is equal to 1002.5 psia.

Next, the mass of xenon in weighing bomb 1 was determined.

Weights used: 2 g, 500, 200, 100, 100* mg

Balance chain at: 27.2 mg

Weights of masses in vacuum = $(2.900 - 0.0011)(0.99985) = 2.8986$ g

Weight of chain = $0.0272 + 0.0004 = 0.0276$

Total weight in vacuum = $2.8986 + 0.0276 = 2.9262$ g

Weight xenon = $16.0351 - 2.9262 = 13.1089$ g

Volume of weighing bomb at 30°C and 1002.5 psia (from Figure 19)
= 11.2020 cm^3

Volume of weighing bomb at 25°C and 1002.5 psia (from Eq. (72))
= $11.2020[1 - (3.8 \times 10^{-5})(5)]$
= 11.1999 cm^3

Density at loading = $\frac{13.1089 \text{ g}}{11.1999 \text{ cm}^3} = 1.1704 \text{ g/cm}^3$

For data point #1, temperature measurement:

Voltage drop across thermometer = 0.1097808 volt

Voltage drop across standard resistor
= 0.10002120 and 0.10002125

Temperature of standard resistor = 20.75°C

Resistance of standard resistor (from Table II) = 99.99670 ohms

Ice point resistance = 100.00542 ohms

$$\frac{R_t}{R_o} = \frac{0.1097808}{0.100021225} \times \frac{99.99670}{100.00542} = 1.097479 \text{ (from Eq. (63))}$$

From Table III, t = 25.000°C (1948 ITS); conversion to 1968 IPTS using Figure 18, t = 24.992°C

Resonance measurements:

C = 12.04 pf

f = 38775.082 Hz

R = 85,830 ohms

Half-power points (at R = 171,660 ohms)

1) C = 35.86 pf , f = 38767.446 Hz

2) C = -11.92 pf, f = 38782.787 Hz

$R - R_o = 85,830 - 2500 = 83,330$ ohms

$f_1 - f_2 = 38782.787 - 38767.446 = 15.341$ Hz

From Eq. (40) and the crystal parameters previously given:

$$\eta\rho = \left[\frac{\pi^{1/2}(15.341)(2.646)(83,330)}{(2)(85,830)(38775.082)^{1/2}(\frac{1}{0.1499}+\frac{1}{5.000})}\right]^2 \qquad (73)$$

$$\eta\rho = 6.674 \times 10^{-4} \frac{g^2}{cm^4 sec}$$

since $\rho = 1.1704$ g/cm^3 , $\eta = 5.702 \times 10^{-4}$ poise.

Data point #2 was at 21.995°C. At this temperature the pressure in the cell was about 975 psia[40]. From Eq. (72):

$$\rho = 1.1704[1 + (2.3 \times 10^{-7})(1002.5 - 975) + (3.8 \times 10^{-5})(3)]$$

$$\rho = 1.1705 \text{ g/cm}^3 \qquad (74)$$

After the isochore was completed, the xenon in the cell was transferred to weighing bomb 2, which was removed from the manifold and weighed.

Weights used: 50, 1 g

500, 50 mg

Rider at: +17.6 mg

Weight of masses in vacuum = (51.5500 - 0.0009)(0.99985)

= 51.5415 g

Total weight in vacuum = = 51.5415 + 0.0176 = 51.5591 g

Weight of xenon in cell = 78.3722 - 51.5415 = 26.8131 g

Volume of cell at loading = $\frac{26.8131 \text{ g}}{1.1704 \text{ g/cm}^3}$ = 22.9093 cm^3

This value is reduced to the standard conditions of 25°C and 1000 psia by Eq. (72), which yields basically no change in the volume.

IV RESULTS[a]

The main interest of the present investigation has been the viscosity measurements for ten xenon isochores and five ethane isochores in the critical region. However, the viscosities of several other fluids have in addition been measured. Normal-hexane, cyclohexane, and propane viscosities were measured and compared with presumably accurate literature values. The viscosity of carbon dioxide was measured in the critical region, partially as a check and partially to collect new data. The data presented by other investigators for the viscosity of carbon dioxide in the critical region differed by as much as 7% for the different experiments. The carbon dioxide data taken in the present experiment are of the same quality as the xenon and ethane data.

There are no known viscosity data for xenon in the critical region, so no comparison with the present data can be made. For ethane however, it was possible to run a comparison with one data point on the isochore farthest from critical.

In general, it appears that the accuracy of the torsional crystal viscometer is related to the value of the resonant resistance of the crystal in the particular fluid. The fluids yielding large resonant resistances, i.e., large viscosity-density products, seem to be more amenable to measurement with the torsional crystal viscometer. This is undoubtedly due to the problem of analyzing the vacuum resistance or background losses in the crystal. For fluids with low

---

[a] The raw data can be found in Notebooks #5063, 6008, and 6019, in the file of Professor C. J. Pings, Caltech.

viscosity-density products, the vacuum resistance is a significant fraction of the resonant resistance. To put it another way, the crystal losses are significant with respect to the viscous losses.

All data were taken at an applied voltage of 1.0 volt across the crystal.

A. Normal-Hexane and Cyclohexane[b]

The n-hexane and cyclohexane used were reagent grade, 99+ mole % supplied by Matheson, Coleman, and Bell Company, East Rutherford, New Jersey. The viscosity measurements were taken with the liquids open to the atmosphere, the open cell being filled with a syringe. The temperatures were measured with a mercury in glass thermometer, believed to be accurate to $0.1^{\circ}C$.

The densities needed to determine the viscosity were taken from the API Research Project 44 [43]. The calculated viscosities were compared with viscosity values from the same publication. Table VI lists the calculated viscosities, the API viscosities[43], and the percentage variation of the present data from the API values. Figures 22 and 23 give the comparison in graphical form.

The comparison seems quite good, especially when considering the conditions under which the present data were taken. At $30^{\circ}C$, n-hexane yields a resonant resistance of about 141,000 ohms, while cyclohexane yields a resonant resistance of about 261,000 ohms.

---

[b] Some of the measurements in this section were taken by Dr. Anthony F. Collings.

B. Propane

The viscosity of propane has been measured at various pressures along the 100°F isotherm (37.778°C). The propane used was instrument grade (99.5% pure) supplied by the Union Carbide Corporation. During the measurements the cell was open to the manifold and the pressure was measured on gauge #1. The densities needed to calculate the viscosities were determined from the PVT data of Reamer, et al.[44]. Propane is quite incompressible in the region being measured and the accuracy of the calibrated gauge was quite sufficient to yield realistic densities. Temperature was measured with the platinum resistance thermometer as previously described.

The calculated viscosities are compared to the data of Carmichael, et al.[45], as shown in Table VII and Figure 24. The comparison of the data seems quite good over the entire pressure range. At 1000 psia, the resonant resistance of the crystal in propane is about 73,500 ohms.

C. Carbon Dioxide

Viscosity measurements were taken for three isochores in the critical region. The carbon dioxide used was instrument grade (99.99% pure) supplied by the Union Carbide Corporation. The data were taken using the same procedures as for xenon and ethane. The viscosity data are presented in Table VIII. Figure 25 shows the location of the data points in the thermodynamic density-temperature plane. The coexistence curve drawn is suggested from the data of Michels, et al.[40]. The approximate location of the critical point is at $T_c = 31.03^{\circ}C$, $\rho_c = 0.4679$ g/cm^3 [46].

The data are compared with those of Naldrett and Maass[12] and Kestin, et al.[13] in Figure 26. The present data show the viscosity exhibiting a small increase as the critical temperature is approached along an isochore close to critical density. This increase, which can be considered a critical anomaly, is seen to be much larger for xenon and ethane, since their critical points were more closely approached than the carbon dioxide critical point. The comparisons in Figure 26 are for the isochores of the other experiments closest to those of the present experiment.

D. Xenon

The xenon viscosity data are presented in Table IX. The actual densities for each state are shown, although the data were taken along ten "isochores". The xenon used was supplied by the Union Carbide Corporation, with a nominal maximum impurity level of 50 ppm. A mass spectrograph analysis supplied by the vendor gave 15 ppm as the impurity level. After the experiment had been completed a sample of the xenon was analyzed spectroscopically by the Cryogenic Service Corporation, Glendale, California, and found to have 40 ppm impurities.

The order of presentation of the data follows the order in which they were taken. In general, the viscosities were measured at states of decreasing temperature along the isochores. It was found that small hysteresis effects were present upon heating to the single-phase region from the two-phase region. For this reason, upon entering the two-phase region the xenon was heated to a high temperature and allowed to recover before recommencement of data taking. No actual viscosity data could be taken in the two-phase region.

Figure 27 shows the location of the data points in the thermodynamic density-temperature plane. Figure 28 shows the viscosity data in graphical form. The nominal density of each isochore is the density at the coexistence boundary. Figure 29 shows viscosity as a function of density for two isotherms at 30°C and 16.685°C. The isotherms were obtained by cross-plotting the smoothed isochoric data.

The data indicate the existence of a "spurious" peak in the viscosity around 25°C for some of the isochores. These contributions have been observed in other systems by a number of investigators who

used a torsional crystal viscometer[14,47,48]. It is believed the peaks are caused by a compressional wave which is the result of another oscillatory mode existing in the crystal. The possibility of non-torsional modes of oscillation in the crystal has been previously discussed. Compressional waves, unlike shear waves, are not highly attenuated. When the velocity of sound in the medium is such that the wavelength of the compressional wave couples with some dimension in the cell, a resonance is produced which appears as the spurious contribution to the resistance of the crystal. Due to the large isothermal compressibility in the critical region, the pressure varies only a small amount from isochore to isochore at 25°C. It seems reasonable to assume that the velocity of sound necessary to cause the spurious resistance reproduces in the region of 25°C for different isochores.

Theoretically, it should be possible to change the crystal size or cell geometry to shift the unwanted resonances to another region. This, however, was not practicable in the present investigation. A second cell of quite similar geometry was used for some check measurements, with the result that the position of the peaks was shifted (see Appendix II). This proved to be inconclusive since the nature and position of the peaks were sensitive to small changes in density, and the densities used with the second cell were not exactly the same as those with the original cell.

It is expected that the values for the viscosity-density product are not appreciably affected by the compressional wave, except in the region of the peaks. The spurious viscosity data are not shown in Figure 28. They are, however, included in Table IX and are noted

by an asterisk. The largest spurious peak (about 3.5% of the viscosity) is for isochore #7, at $\rho = 1.1036$ g/cm^3. The apparent viscosities in the region of the spurious peak for this isochore are plotted in Figure 30.

Although all data were taken with a voltage of 1.0 volts, check measurements were taken at 0.3 volts. There seemed to be little difference in the resonant resistances for the two voltages, even very close to the critical point. Since the rate of shear is proportional to the applied voltage, this seems to indicate that the viscosity is independent of the shear rate and the Newtonian viscosity relationship still holds. Sallavanti and Fixman[49] had suggested that the viscosity might be affected by the shear rate close to the critical point, but this does not seem to be the case.

As previously mentioned, there are no xenon viscosity data in the literature for the region of this experiment. It is expected that the values given here represent the true viscosities to within ±3% . The precision of the viscosity data is approximately ±0.5%.

E. Ethane

The ethane used was research grade with a nominal maximum impurity level of 100 ppm, supplied by the Air Reduction Company, New York City. A mass spectrographic analysis performed by West Coast Technical Service Inc., San Gabriel, California, gave the maximum impurity level to be 50 ppm.

The ethane viscosity data are presented in Table X. As with the xenon, the viscosities were measured in the order of presentation. Similar hysteresis and two-phase region effects were noticed for ethane as for xenon. Figure 31 shows the location of the data points in the thermodynamic density-temperature plane. Figure 32 shows the viscosity data in graphical form. Figure 33 shows the viscosity as a function of density for two isotherms at 49°C and 32.24°C. The isotherms were obtained by cross-plotting the smoothed isochoric data.

Isochore #4, at $\rho = 0.21638$ g/cm^3 exhibited a spurious peak similar to those observed in xenon, except not quite as broad. The peak shows up around 40.5°C. The value of the peak is about 2% of the viscosity. The spurious data are marked with an asterisk in Table X and are not included in Figure 32.

There are some ethane viscosity data in the literature which overlap the region covered in the present experiment, notably those of Starling, et al.[11] and Carmichael and Sage[50]. These data, however, are presented as a function of pressure along isotherms, whereas the present experiment measured viscosity as a function of temperature along isochores. To compare the two types of viscosity data, accurate PVT values must be known for the states measured. Interpolation in

the critical region is not accurate. With this in mind, it was possible to compare only one data point with the viscosity for the same state as given by Carmichael and Sage[50]. The PVT data of Reamer, et al.[41] were used. For isochore #3 at $T = 37.769^{\circ}C$ and $\rho = 0.28988\ g/cm^3$ the viscosity is 310.9 micropoise. The pressure at this state is given as 898.2 psia[41]. The viscosity at 898.2 psia and $100^{\circ}F$ ($37.778^{\circ}C$) is given by Carmichael and Sage[50] to be 336.1 micropoise. The viscosities differ by about 7.5%.

The viscosity-density product for ethane is quite low, much smaller than that for xenon or carbon dioxide. As previously mentioned, the vacuum resistance is about 10% of the resonant resistance for ethane. The vacuum resistance is not expected to be an accurate measure of the actual crystal losses. It is felt that this is the reason for the inaccuracy of the ethane data. The "relative accuracy" of the viscosity data should still be good, however, and any critical region effects noticed should be valid. The precision of the viscosity data is the same as for xenon, about ±0.5%.

V. DISCUSSION

A. Anomalous Critical Behavior

The "critical" behavior of the viscosity can be inferred from Figures 28 and 29 for xenon and Figures 32 and 33 for ethane. Away from the critical density, the viscosity isochores are relatively flat until the coexistence curve is reached. Close to critical density, however, the viscosity isochores are flat only until the critical temperature is approached. At this point, the viscosity increases as the temperature is lowered. This increase can be considered to be "anomalous" critical behavior. The range of the data may be too narrow for the isothermal representation to show the character of the anomaly, but the critical increase is quite apparent. The behavior of the viscosity seems to be similar to that found by Naldrett and Maass[12] and Kestin, et al.[13].

It is of interest to consider the behavior of the "anomalous" viscosity as a function of reduced temperature difference ε along the critical isochore. As previously discussed, the relationship of properties with reduced temperature difference is a convenient way to characterize the critical behavior. In particular, Eqs. (3) and (4) which have been used to characterize the viscosity of the binary liquid mixtures can be similarly used for single component viscosities. One of the difficulties in the use of these relationships is that the characteristic behavior is often strongly affected by the nature of the anomalous viscosity term.

J. V. Sengers[51] suggests the following form for the anomalous viscosity along the critical isochore $\Delta\eta$:

$$\Delta\eta = \eta(\rho_c,T) - \eta(\rho_c,T_{ref}) + \eta(0,T_{ref}) - \eta(0,T) \tag{75}$$

where $\eta(\rho_c,T)$ is the measured viscosity

$\eta(\rho_c,T_{ref})$ is the viscosity along the critical isochore at a super-critical reference temperature

$\eta(0,T_{ref})$ is the dilute gas viscosity at zero density and the reference temperature

$\eta(0,T)$ is the dilute gas viscosity at the temperature of measurement.

Equation (75) is derived as follows. The anomalous viscosity can be represented as:

$$\Delta\eta = \eta(\rho_c,T) - \eta_{id}(\rho_c,T) \tag{76}$$

where η_{id} is the "ideal" viscosity which would be the value of the viscosity in the absence of any critical behavior. Consider the non-critical excess viscosity η^* , which is the difference between the actual viscosity and the dilute gas viscosity at the same temperature:

$$\eta^*(\rho_c) = \eta(\rho_c,T_{ref}) - \eta(0,T_{ref}) \tag{77}$$

It is often assumed that the excess viscosity is a function of density alone and independent of the temperature[50]. In the absence of critical effects, the viscosity in the critical region would be given by:

$$\eta_{id}(\rho_c,T) = \eta^*(\rho_c) + \eta(0,T) \tag{78}$$

The combination of Eqs. (76)-(78) results in Eq. (75).

For xenon, the reference temperature is chosen as 30°C, the highest temperature for which viscosities were measured. The low density viscosities are taken from the data of Clarke and Smith[52] and are reproduced in Figure 34 for the range of interest. In Eq. (75), $\eta(0,T_{ref})$ = 234.4 micropoise and the values for $\eta(0,T)$ range from 226.8 to 224.4 micropoise for the states considered.

The critical point of the xenon used in the present investigation has been determined by visual observation (see Appendix II). The values are $T_c = 16.627 \pm 0.005^{\circ}C$ and $\rho_c = 1.11 \pm 0.01$ g/cm^3. These compare with the values of $T_c = 16.590^{\circ}C$ and $\rho_c = 1.105$ g/cm^3 as reported by Weinberger and Schneider[53]. Their critical temperature is presumably reported in relation to the 1948 ITS. This would be equivalent to 16.584°C on the 1968 IPTS.

The isochore closest to the determined critical density is #5 at $\rho = 1.1092$ g/cm^3. This is taken as the "critical" isochore and used in Eq. (75). The value of $\eta(\rho_c,T_{ref})$ is 535.2 micropoise.

Using the data given in Table IX, the anomalous viscosities have been calculated and are listed in Table XI. The onset of the critical behavior is around $T - T_c = 3.5^{\circ}C$, $\varepsilon = 1.2 \times 10^{-2}$. The closest approach to critical is at $T - T_c = 0.034^{\circ}C$, $\varepsilon = 1.2 \times 10^{-4}$. At temperatures closer to critical than 0.034°C, it was not possible to get sensible viscosity measurements due to the severe density gradients set up in the gravitational field. Gravitational effects are discussed in a later section. The maximum value for the anomalous viscosity at the closest approach to critical is about 15% of the ideal viscosity.

In Figure 35, the logarithm of the anomalous viscosity is plotted as a function of the logarithm of the reduced temperature difference from critical. As can be seen, the data do not fall on a straight line and do not seem to be consistent with the idea of an exponential divergence. In Figure 36, the anomalous viscosity is plotted as a function of the logarithm of reduced temperature difference. The data can be fitted to a straight line of equation

$$\Delta\eta = -37.71 \log\left(\frac{T - T_c}{T_c}\right) - 68.66; \quad \Delta\eta \text{ in micropoise} \tag{79}$$

by a linear least-squares technique. The error bars in Figures 35 and 36 represent the estimated precision of a viscosity measurement, ± 0.5%.

The results seem to be consistent with the idea of a logarithmic viscosity divergence, the form of which is given in Eq. (4). The straight line fit is only weakly dependent upon the nature of the anomalous viscosity determination and a straight line could be reasonably well fitted to a plot of actual viscosity versus $\log\left(\frac{T - T_c}{T_c}\right)$. The difficulty of distinguishing among a logarithmic divergence, a small exponential divergence, and a finite limit for viscosity has been previously mentioned. The results of the present investigation should not be construed so as to preclude the possibility of a finite limit or small exponential divergence for the anomalous viscosity.

The critical point of ethane has also been determined by visual observation (see Appendix II). The values were found to be $T_c = 32.218 \pm 0.005^{\circ}C$ and $\rho_c = 0.2055 \pm 0.002$ g/cm^3. There is a disparity in the critical parameters for ethane as reported in the literature. A recent investigation by Miniovich and Sorina[54] gave

the values of $T_c = 32.200 \pm 0.005^{o}C$ and $\rho_c = 0.2041 \pm 0.0007$ g/cm^3. The temperature scale was not given.

The isochore closest to the determined critical density is #2 at $\rho = 0.20952$ g/cm^3. This is taken as the "critical" isochore and used in the determination of the anomalous viscosity.

The reference temperature for ethane is chosen as $49^{o}C$, the highest temperature for which viscosities were measured. The value of $\eta(\rho_c, T_{ref})$ is 200.2 micropoise. The low density viscosities are taken from the data of Carmichael and Sage[50] and are reproduced in Figure 37 for the range of interest. The range in $\eta(0,T)$ is from 95.7 to 95.5 micropoise and $\eta(0,T_{ref}) = 100.4$ micropoise.

Using the data given in Table X, the anomalous viscosities have been calculated and are listed in Table XII. The onset of the critical behavior is around $T - T_c = 0.8^{o}C$, $\varepsilon = 2.5 \times 10^{-3}$. The closest approach to critical is at $T - T_c = 0.017^{o}C$, $\varepsilon = 5.6 \times 10^{-5}$. Again gravitational problems are blamed for the inability to more closely approach the critical temperature. The maximum value for the anomalous viscosity at the closest approach to critical is about 16% of the ideal viscosity.

Figures 38 and 39 show the logarithm of the anomalous viscosity and the anomalous viscosity plotted as a function of the logarithm of reduced temperature difference. The error bars represent the estimated precision of the measurements, ± 0.5%. The data in Figure 39 are fitted to a straight line of equation

$$\Delta\eta = -15.15 \log\left(\frac{T - T_c}{T_c}\right) - 32.57; \quad \Delta\eta \text{ in micropoise} \qquad (80)$$

by a linear least squares technique. The ethane data also seem to be consistent with the idea of a logarithmic divergence of viscosity as given in Eq. (4).

B. Gravitational Effects

A fluid of finite height in a gravitational field is compressed under its own weight. Close to the critical point where the isothermal compressibility becomes very large, this phenomenon results in large density gradients in the direction of the field. These effects are well known[55] and are of great hindrance to critical region studies, the present investigation not excepted.

It is possible to estimate the density gradients in the cell by using the scaling law equation of state. The scaling law equation of state is a universal equation which can be used to predict the reduced PVT properties of fluids in the critical region as follows[51]:

$$\Delta\mu^* = \Delta\rho^* |\Delta\rho^*|^{\delta-1} h(x) \tag{81}$$

where $\Delta\mu^* = \dfrac{\mu(\rho,T) - \mu(\rho_c,T)}{P_c/\rho_c}$

$$\Delta\rho^* = \frac{\rho - \rho_c}{\rho_c}$$

$$x = \frac{\varepsilon}{|\Delta\rho^*|^{1/\beta}}$$

μ is the chemical potential

β and δ are the critical exponents,

and $h(x)$ is a function only of x.

The following form of $h(x)$ has been proposed by Vicentini-Missoni and Levelt Sengers[56]:

$$h(x) = E_1 \left(\frac{x+x_o}{x_o}\right)\left[1 + E_2\left(\frac{x+x_o}{x_o}\right)^{2\beta}\right]^{[\beta(\delta-1)-1]\ 2\beta} \qquad (82)$$

Vicentini-Missoni and Levelt Sengers give the following values for the parameters, derived from the available xenon PVT data in the critical region[56]:

$\beta = 0.350$

$\delta = 4.6$

$x_o = 0.186$

$E_1 = 2.96$

$E_2 = 0.37$

$P_c = 57.636$ atm

From Eqs. (81) and (82) the difference in chemical potential $\mu(\rho,T) - \mu(\rho_c,T)$ can be calculated for a given density and temperature. The chemical potential difference is proportional to height in the gravitational field, as follows[51]:

$$z - z_c = -\frac{1}{g}\left[\mu(\rho,T) - \mu(\rho_c,T)\right] \qquad (83)$$

where g is the local acceleration of gravity

and z_c is the height at which the local density equals the critical density.

Using the values of T_c and ρ_c from the present investigation, the density profile has been calculated for $T - T_c = 0.034^{o}C$, using Eqs. (81)-(83). This temperature difference represents the closest approach to the critical temperature of xenon in the present investigation. The calculated profile is shown in Figure 40. It should be

made clear that the curve in Figure 40 does not necessarily represent the density profile in the cell, but simply shows the variation of density with height, with the position of the height coordinate not specified. In order to specify the position of the vertical component, it is necessary to know the value of the local density at some height in the cell.

In the present investigation, the viscosity measurements can potentially be affected by the density gradients in two ways. First, close to the critical temperature the density can vary appreciably over the vertical component of the crystal, even though the crystal is aligned parallel to the horizontal and the diameter is only 0.3 cm. If the density at the center of the crystal is the critical density, it can be seen from Figure 40 that for $T - T_c = 0.034^{o}C$ the density can vary by ±1.5% over the ±0.15 cm of the crystal diameter. If the density at the center of the crystal is different from critical, the variation is not as large, but is still quite substantial at densities close to critical. As the critical temperature is more closely approached, the gradient over the crystal increases rapidly. It is difficult to predict what effect the density gradient would have on the measured viscosity. Presumably some sort of "averaging" of the viscosity-density product would occur, possibly masking the anomalous increase. The crystal, of course, measures the viscosity-density product only of a very thin layer of fluid surrounding the crystal, and is unaffected by the bulk fluid.

The second problem is closely related to the first. At an average density close to, but not exactly at the critical, the density

at the level of the crystal changes as the critical temperature is approached, and can become quite different from the average density. Since the average density value is used in calculating the viscosity from the resonant properties of the crystal, what results is an apparent viscosity for a non-existing state. This, of course, can be quite different from the real viscosity for the existing state. The cell is about 1.8 cm high, with the crystal positioned approximately in the center.

It is believed that the above-mentioned difficulties caused the apparent viscosity values to degenerate for values of $T - T_c < 0.034^{o}C$ for xenon. The ethane problems were, of course, similar to those found for xenon. Since ethane is quite a bit less dense than xenon, the gravitational effects might not be expected to be as severe. Indeed, the viscosity values seemed to be sensible up to $T - T_c = 0.017^{o}C$.

VI. CONCLUSIONS AND RECOMMENDATIONS

The viscosity of xenon has been measured along ten isochores and the viscosity of ethane has been measured along five isochores in the critical region. The data have been found to be consistent with the idea of a logarithmic divergence in anomalous viscosity with reduced temperature difference from critical. The results, however, do not exclude the possibility of either a finite limit or a small exponential divergence of anomalous viscosity.

The critical temperatures and densities have been found to be $T_c = 16.627 \pm 0.005^{\circ}C$, $\rho_c = 1.11 \pm 0.01$ g/cm^3 for xenon and $T_c = 32.218 \pm 0.005^{\circ}C$, $\rho_c = 0.2055 \pm 0.002$ g/cm^3 for ethane. The temperatures are stated with respect to the 1968 International Practical Temperature Scale.

The torsional crystal method seems to be the best available technique for measuring viscosities in the critical region. The major limitations seem to be the large background losses relative to the fluid losses and the density gradients set up in the gravitational field close to the critical point.

The background losses seem to increase with temperature. In the same temperature range, the most accurate results are obtained for the fluid with the largest viscosity-density product. The torsional crystal method has been used for low temperature measurements of a non-critical nature and has performed quite well[47]. At cryogenic temperatures, the background losses are quite small with relation to the fluid losses[47]. Thus it should be possible to measure the

viscosity of cryogenic fluids in the critical region (e.g., argon or nitrogen) very accurately. Of course, special care would have to be taken to insure the stability of the solder joints and correct for the change in dimensions of the quartz.

Gravitational effects seem to be a serious limitation on the viscosity measurements. Techniques exist for determining the density in a cell as a function of height by measuring the index of refraction of the fluid at various levels and relating the index to the density[55]. The method requires a cell which is transparent. This technique could determine the mean density at the level of the crystal for different temperatures so that viscosity could be determined for the correct state.

Another possibility is the use of a crystal with two electrical leads attached to the ends at the crystal axis, rather than the four radially attached leads used in the present investigation. The gold electrodes would have to be continued on the ends, so as to make contact with the leads. If this configuration could be made to work, the cell could be made much smaller, with a diameter only slightly larger than that of the crystal. The mean density at the crystal would thus be very similar to the average density in the cell.

It does not appear that anything can be done about the density gradient over the crystal diameter, save performing the measurements in a zero gravity field. The crystal used in the present investigation is as small (0.3 cm) as is commonly used, although it certainly may be possible to manufacture crystals of smaller diameter. This, of course, would not eliminate the density gradients; only increase the

effective range of the viscometer.

The torsional crystal method seems especially well suited for viscosity measurements on binary liquid mixtures in the region of their consolute points. Most viscosity measurements on the binaries have been performed in open systems using flow-type viscometers. These techniques seem questionable in the consolute region and could be improved upon by the torsional crystal viscometer.

APPENDIX I

PRESSURE AND TEMPERATURE CHANGES IN THE FLUID CAUSED BY THE CRYSTAL OSCILLATION

In the development of the equation relating the fluid viscosity to the crystal properties, it was necessary to assume that the term ∇P was negligible with respect to the other terms in the equation of motion, Eq. (7). This is a conventional assumption made in the derivation of the velocity equation for a plane propagated shear wave[57]. The assumption seems quite valid, since the term ∇P represents the total pressure change in the fluid, which includes the large, non-varying bulk pressure. Assuming that the above assumption is valid, it is possible to estimate the maximum magnitude of the pressure variation, to see what effect it would have in the critical region, where the isothermal compressibility is very large.

In order to do this, it is necessary to determine the velocity at the crystal surface v_w. This can be done by equating the energy dissipated in the viscous wave with the electrical energy supplied to the crystal. The energy supplied per cycle W is assumed to be:

$$W = \frac{E^2}{R} \frac{2\pi}{\omega} \tag{84}$$

where E is the applied voltage.

The energy dissipated is given by Eq. (27) reproduced here:

$$W_D = \frac{\pi \eta v_w^2 S}{\omega \delta} \tag{85}$$

Equating Eqs. (84) and (85) yields:

$$v_w^2 = \frac{2E^2\delta}{R\eta S} \quad . \tag{86}$$

The following values of the parameters can be used:

$E = 1$ volt

$\delta = 6.7 \times 10^{-5}$ cm

$R = 80{,}000$ ohms

$\eta = 6 \times 10^{-4}$ g/cm sec

$S = 4.85$ cm^2 .

Substitution of these values into Eq. (86) gives

$$v_w = 2.4 \text{ cm/sec} \quad . \tag{87}$$

This represents the maximum linear velocity of a point on the end of the crystal. The velocity, as can be seen from Eq. (86), is directly proportional to the voltage.

The maximum pressure variation can be estimated in the following manner. Starting with the equation of motion, Eq. (7), cancel the gravitational terms in ∇P and $\rho \underline{g}$. The pressure effect can now be determined by neglecting the shear stress term $\nabla \cdot \underline{\underline{\tau}}$ and determining P from the resultant equation. This is equivalent to neglecting the velocity term $\rho \frac{D\underline{v}}{Dt}$ and retaining $\nabla \cdot \underline{\underline{\tau}}$ since $\rho \frac{D\underline{v}}{Dt}$ equals $\nabla \cdot \underline{\underline{\tau}}$. The pressure effect calculated from the above analysis should be much larger than the actual pressure effect, since the ∇P term is thought to be much smaller than the other terms.

Neglecting $\nabla \cdot \underline{\underline{\tau}}$, the equation of motion becomes:

$$\rho \frac{\partial v_z}{\partial t} = - \frac{\partial P}{\partial y} \quad . \tag{88}$$

Substituting the known form of the velocity, from Eq. (20), and differentiating yields :

$$-\omega \rho v_w e^{-y/\delta} \sin(\omega t - \frac{y}{\delta}) = - \frac{\partial P}{\partial y} \quad . \tag{89}$$

Equation (89) can be solved by integration:

$$P = \int \omega \rho \, v_w \, e^{-y/\delta} \sin(\omega t - \frac{y}{\delta}) \, dy \tag{90}$$

$$P = \frac{\omega \rho v_w \delta}{2} e^{-y/\delta} \left[\cos(\omega t - \frac{y}{\delta}) - \sin(\omega t - \frac{y}{\delta})\right] + P_B \tag{91}$$

where P_B , the bulk pressure, is the value of P for $y = \infty$.

It can readily be seen that the term $\frac{\omega \rho v_w \delta}{2}$ represents the maximum pressure variation caused by the viscous wave, since the maximum value of $e^{-y/\delta}[\cos(\omega t - \frac{y}{\delta}) - \sin(\omega t - \frac{y}{\delta})]$ is unity.

Using the parameter values previously given and $\omega = 2\pi f$, $f = 38{,}700$ Hz, $\rho = 1.11$ g/cm^3 , the maximum pressure effect $P - P_B$ is found to be:

$$P - P_B = 21.6 \text{ dyne/cm}^2 = 3.1 \times 10^{-4} \text{psia} \quad . \tag{92}$$

Pressure variations of this order of magnitude should cause negligible density variations, even very close to the critical point.

Before going on to the temperature effect, it is of interest to calculate a number of parameters, values of which were not

previously given. The maximum amplitude of a point on the end of the crystal is given by v_w/ω , and is equal to about 1×10^{-5}cm . The maximum shear stress per unit area is easily shown to be equal to the maximum pressure variation, about 21.6 dyne/cm^2. The maximum shear rate is calculated to be $3.6 \times 10^4 \text{sec}^{-1}$.

Welber[47] suggests the following form for a Reynolds number, N_{Re}:

$$N_{Re} = \frac{v_w \rho \delta}{\eta} \tag{93}$$

For the usual conditions, the maximum Reynolds number is about 0.3 , safely in the laminar region.

It is also of importance to consider whether the viscous heating of the fluid results in a significant temperature gradient in the fluid. In the critical region, the isobaric volumetric expansion becomes very large, and a small temperature gradient would cause a large density gradient.

To determine the temperature gradient, consider the general equation of energy for a viscous fluid[58]:

$$\rho C_v \frac{DT}{Dt} = k_T \nabla^2 T - T\left(\frac{\partial P}{\partial T}\right)_\rho (\nabla \cdot \underline{v}) + \eta \Phi_v \tag{94}$$

where C_v is the heat capacity of the fluid at constant volume

k_T is the thermal conductivity of the fluid

Φ_v is the dissipation function.

With the usual assumptions, the dissipation function reduces to $(\partial v_z/\partial y)^2$. Upon elimination of all terms equal to zero, Eq. (94) becomes:

$$\rho C_v \frac{\partial T}{\partial t} = k_T \frac{\partial^2 T}{\partial y^2} + \eta \left(\frac{\partial v_z}{\partial y}\right)^2 \tag{95}$$

To estimate the temperature effect, it will be assumed that the heat capacity is very small so that the term $\rho C_v \frac{\partial T}{\partial t}$ can be neglected. This is the worst possible case, since a fluid of zero heat capacity cannot absorb any energy. Thus, the viscous heating is more readily converted into a temperature increase. For these conditions Eq. (95) reduces to:

$$k_T \frac{\partial^2 T}{\partial y^2} + \eta \left(\frac{\partial v_z}{\partial y}\right)^2 = 0 \tag{96}$$

Using the form of v_z given in Eq. (20), and substituting into Eq. (96) yields:

$$k_T \frac{\partial^2 T}{\partial y^2} + \eta \left[\frac{\partial}{\partial y} v_w e^{-y/\delta} \cos\left(\omega t - \frac{y}{\delta}\right)\right]^2$$

$$\frac{\partial^2 T}{\partial y^2} = \frac{\eta v_w^2}{k_T \delta^2} e^{-2y/\delta} \left[1 - \sin 2\left(\omega t - \frac{y}{\delta}\right)\right] \tag{97}$$

Equation (97) can be solved by integrating twice. The boundary conditions are:

$$\frac{\partial T}{\partial y} = 0 \qquad \text{at} \quad y = \infty$$

$$T = T_B \qquad \text{at} \quad y = \infty \quad . \tag{98}$$

The solution to Eq. (97) is:

$$T = T_B + \frac{3\eta v_w^2}{8k_T} e^{-2y/\delta} \left[\frac{2}{3} - \frac{1}{3} \cos 2\left(\omega t - \frac{y}{\delta}\right)\right] \quad . \tag{99}$$

Since the maximum value of the term $e^{-2y/\delta}\left[\frac{2}{3} - \frac{1}{3}\cos 2(\omega t - \frac{y}{\delta})\right]$ is unity, $\frac{3\eta\, v_w^2}{8k_T}$ represents the maximum temperature increase due to viscous heating. An approximate value for the thermal conductivity of xenon in the critical region is 40.2×10^{-6} cal/cm sec^{o}C [59]. Thus,

$$\frac{3\eta v_w^2}{8k_T} = 7.6 \times 10^{-7}\ ^{o}C \qquad (100)$$

with the usual values for η and v_w. This temperature change is much too small to have any effect, even very close to the critical point.

APPENDIX II

MEASUREMENTS USING A CELL WITH SAPPHIRE WINDOWS

Some viscosity measurements were performed using a cell with sapphire windows. The cell was also used for the visual determination of the critical points of xenon and ethane. The cell was of similar design to the previously described all stainless steel cell with two holes cut so as to be fitted with sapphire windows. The design of the cell is shown in Figure 41. The windows are positioned so that it is possible to see through the cell when it is connected in its normal position.

The sapphire windows are 0.5" in diameter and 0.08" thick. The windows were brazed to a kovar mounting ring which in turn was welded to the cell. The brazing and welding operations, along with the fabrication of the windows, were performed by the Eimac Company, San Carlos, California. A photograph of the cell is shown in Figure 42. The sealing teflon gasket is also shown.

To check the viscosity measurements, the cell was loaded with xenon at a density of $\rho = 1.0996$ g/cm^3, close to isochore #7 at $\rho = 1.1036$ g/cm^3. The viscosity data are given in Table XIII. The viscosities agree fairly well with those measured along isochore #7. Around 25°C, however, the data differ somewhat. Whereas the spurious peak of isochore #7 has a maximum at 25°C, the spurious peak of the sapphire window cell isochore has a maximum at 24°C. The shift in position of the peak may be ascribed to the slight change in the geometry of the two cells. However, the densities are somewhat different, and the nature and position of the peaks are sensitive to

relatively small density differences.

Viscosity measurements were also taken for an ethane loading at $\rho = 0.21578$ g/cm^3, close to ethane isochore #4 at $\rho = 0.21638$ g/cm^3. The data are listed in Table XIV. The data are consistent with those of isochore #4. The position of the spurious peak (at 40.5°C) seems to be the same, but the maximum value is somewhat smaller. It appears that except in the regions of the spurious peaks, the use of the different cell did not affect the viscosity measurements. This, of course, was expected, since the waves produced by the torsional oscillation of the crystal are very rapidly attenuated.

It was possible to determine the critical point by viewing the fluid through the sapphire windows. Normally, on cooling until the coexistence curve is reached, either a gas phase will start forming at the top of the cell, or a liquid phase will form at the bottom of the cell, depending on the density of the loading. The entire cell was not visible through the sapphire windows so the bubble and dew temperatures could not be determined.

At densities close to critical, the meniscus separating the two phases would appear within the visible region of the cell. This behavior was a result of the density gradients in the cell. The meniscus forms in the cell at the level at which the local density is equal to the critical density. On heating from the two-phase region, the meniscus can be seen to disappear within the cell.

Whenever the meniscus appears and disappears within the cell, the temperature of the transition is always the same, and is in fact the critical temperature. Thus, the coexistence curve has an apparent

"flat-top" region, for which the same coexistence temperature exists for a range of mean densities. The width of the "flat-top" region is related to the height of the cell.

In the present investigation the temperature and position of the meniscus were determined (if visible) at the transition point for various mean densities. By assuming that the meniscus should appear near the center of the cell for a mean density equal to critical, it was possible to bracket the critical density along with measuring the critical temperature.

The visual observations were hampered by the onset of critical opalescence as the critical temperature was approached along an isochore of close to critical density. Very close to the critical point, the fluid became opaque under normal lighting, and it was not possible to see into the cell. Using a high-powered lamp, the fluid took on a milky appearance when lighted at an angle. If lighted directly, the fluid took on a transparent, bright orange color. Reflections from the crystal and crystal holder also made viewing the meniscus more difficult. Figure 43 shows the appearance of the cell under direct lighting when it is filled with xenon very close to the critical point. The variation of appearance within the cell is indicative of the density gradient caused by gravity. Figure 43 also shows the appearance of the cell with the xenon far from critical.

The temperatures of appearance and disappearance of the meniscus seemed to differ by a few thousandths of a degree. This difference was probably due to non-equilibrium effects or the existence of metastable states. This difficulty could probably be corrected by a

stirring device.

The critical points as determined by the above techniques have been found to be $T_c = 16.627 \pm 0.005^{\circ}C$, $\rho_c = 1.11 \pm 0.01$ g/cm^3 for xenon and $T_c = 32.218 \pm 0.005^{\circ}C$, $\rho_c = 0.2055 \pm 0.002$ g/cm^3 for ethane. The above values are not so much best estimates of the correct values as they are midpoints of the ranges in which the correct values are thought to lie.

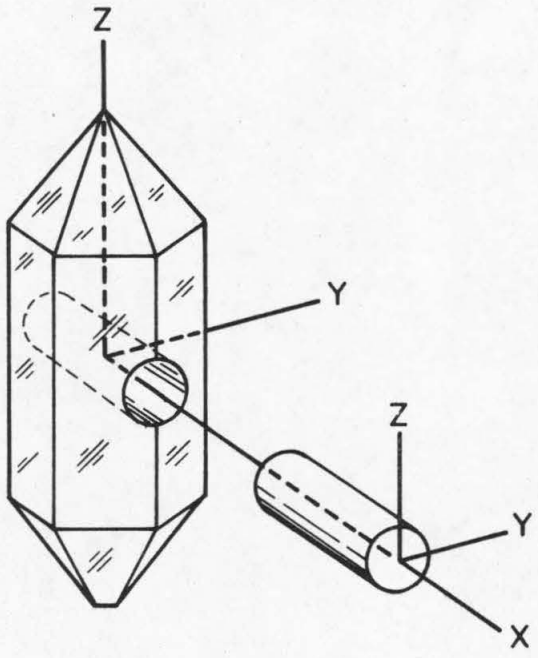

Figure 1. Torsional cylinder cut from quartz crystal

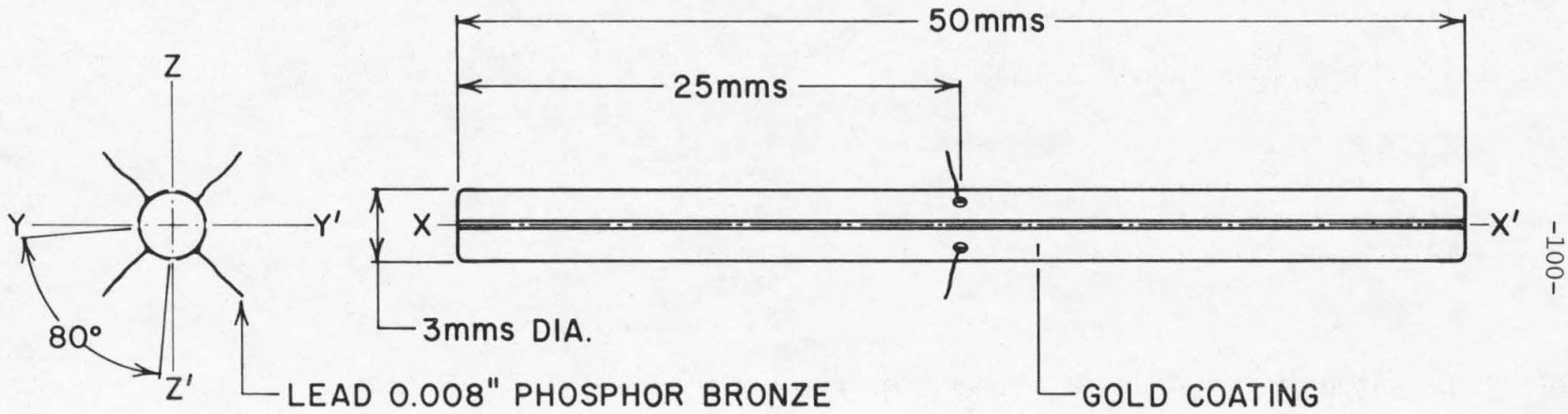

Figure 2. Torsional crystal plating and lead configuration

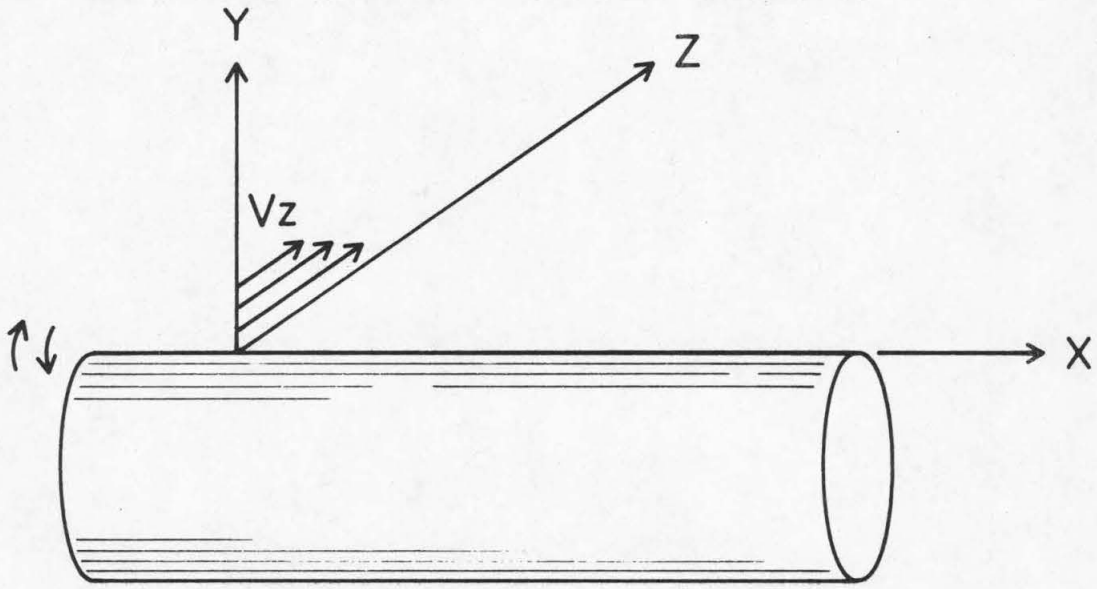

Figure 3. Torsionally oscillating crystal

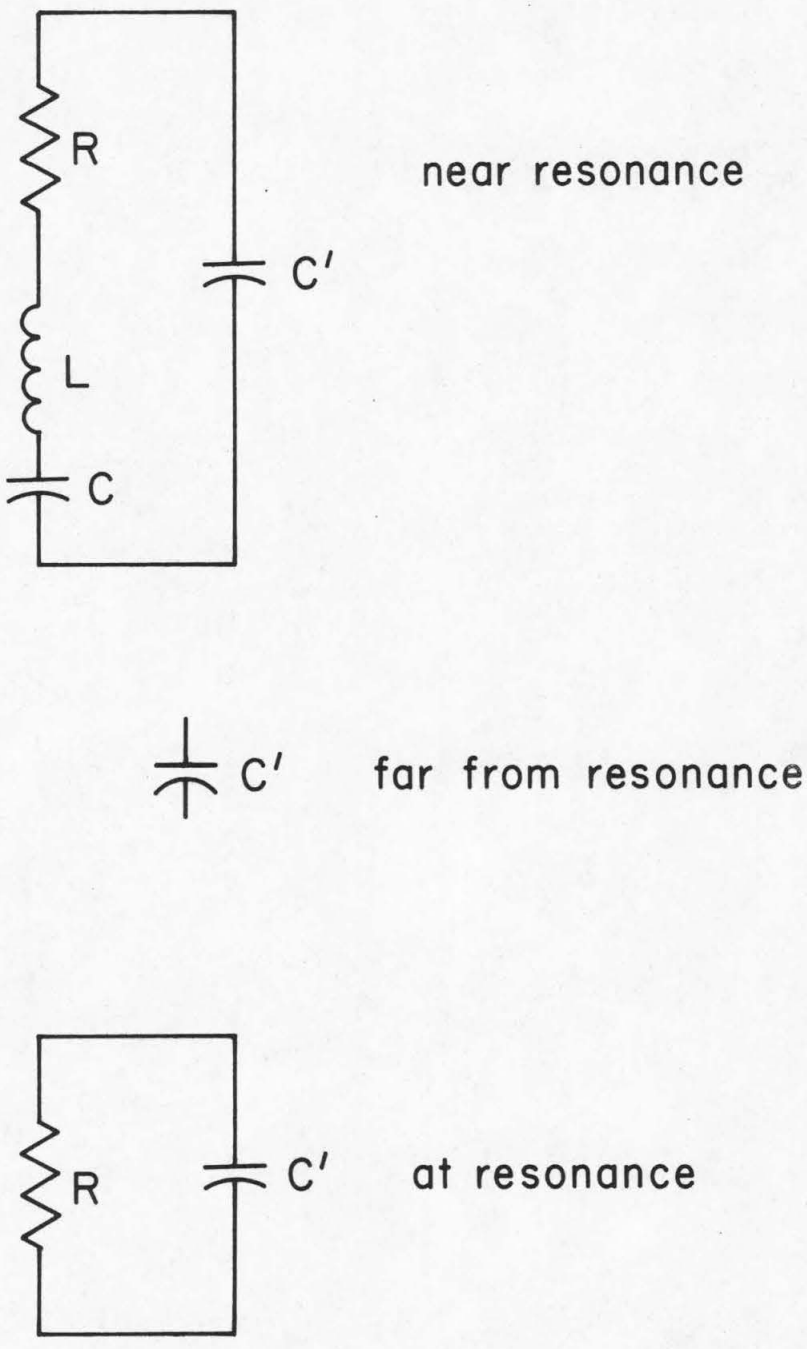

Figure 4. Equivalent circuits of crystal

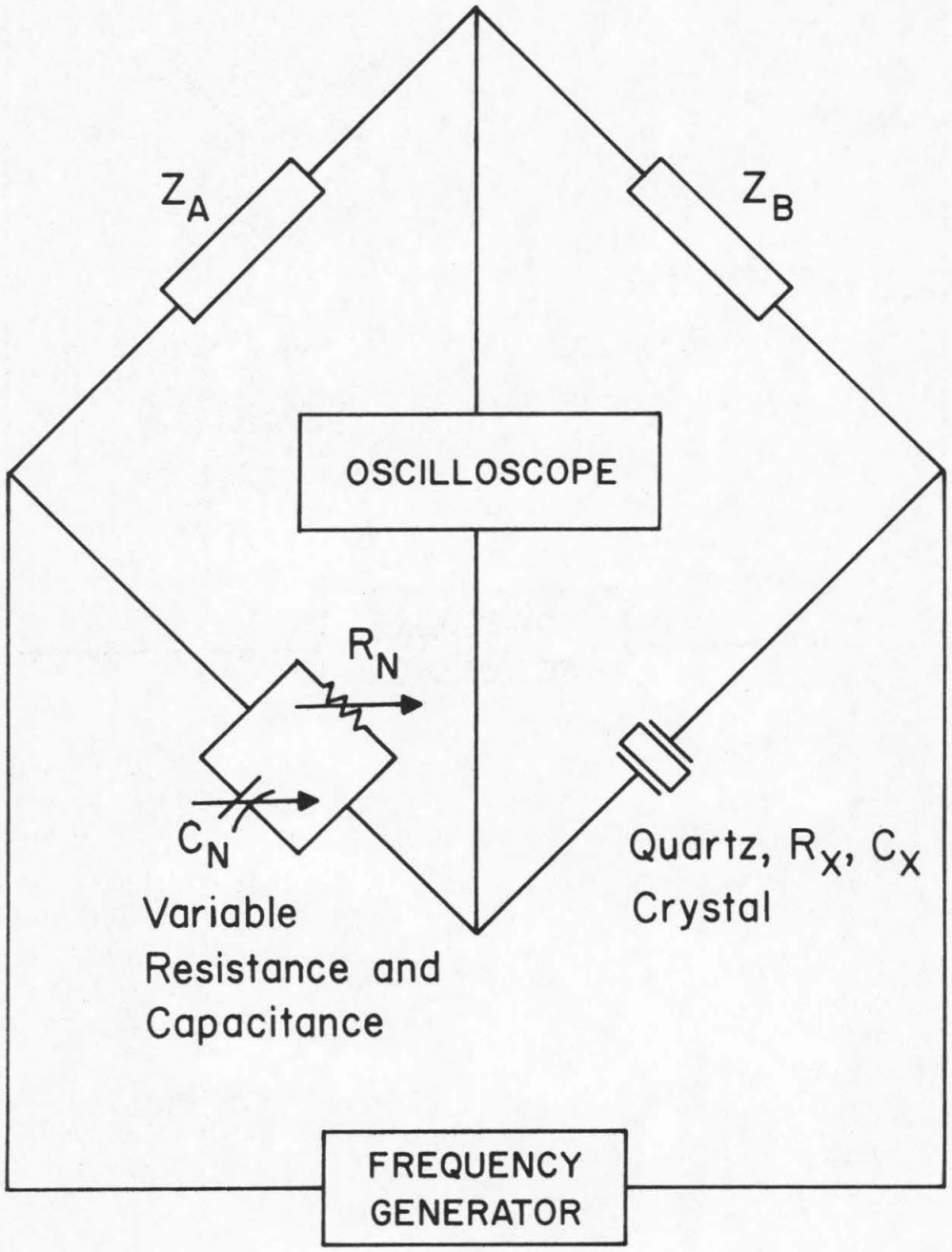

Figure 5. Impedance bridge

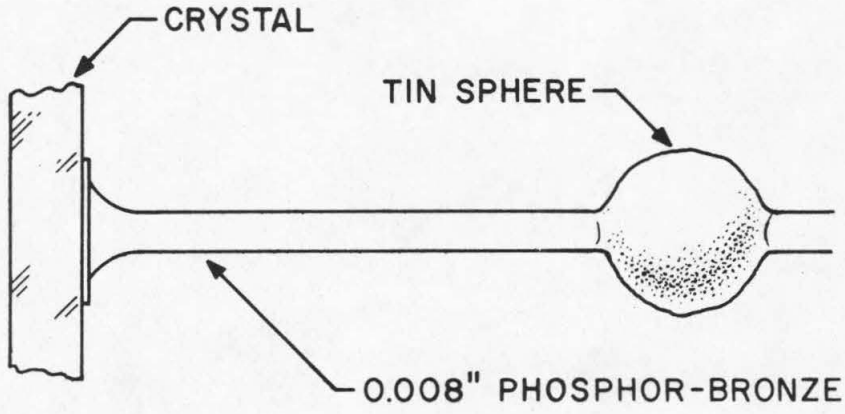

Figure 6. Headed phosphor-bronze wire and tin sphere

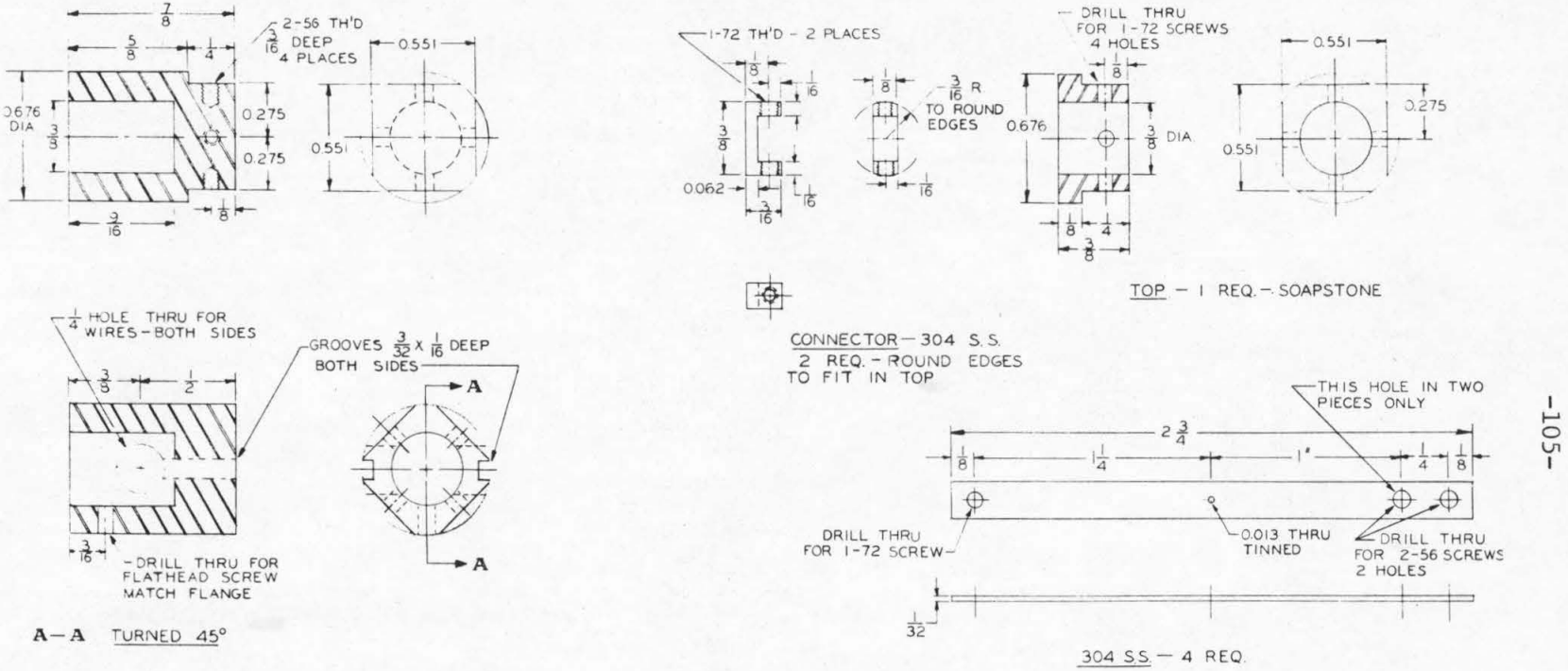

Figure 7. Crystal support unit

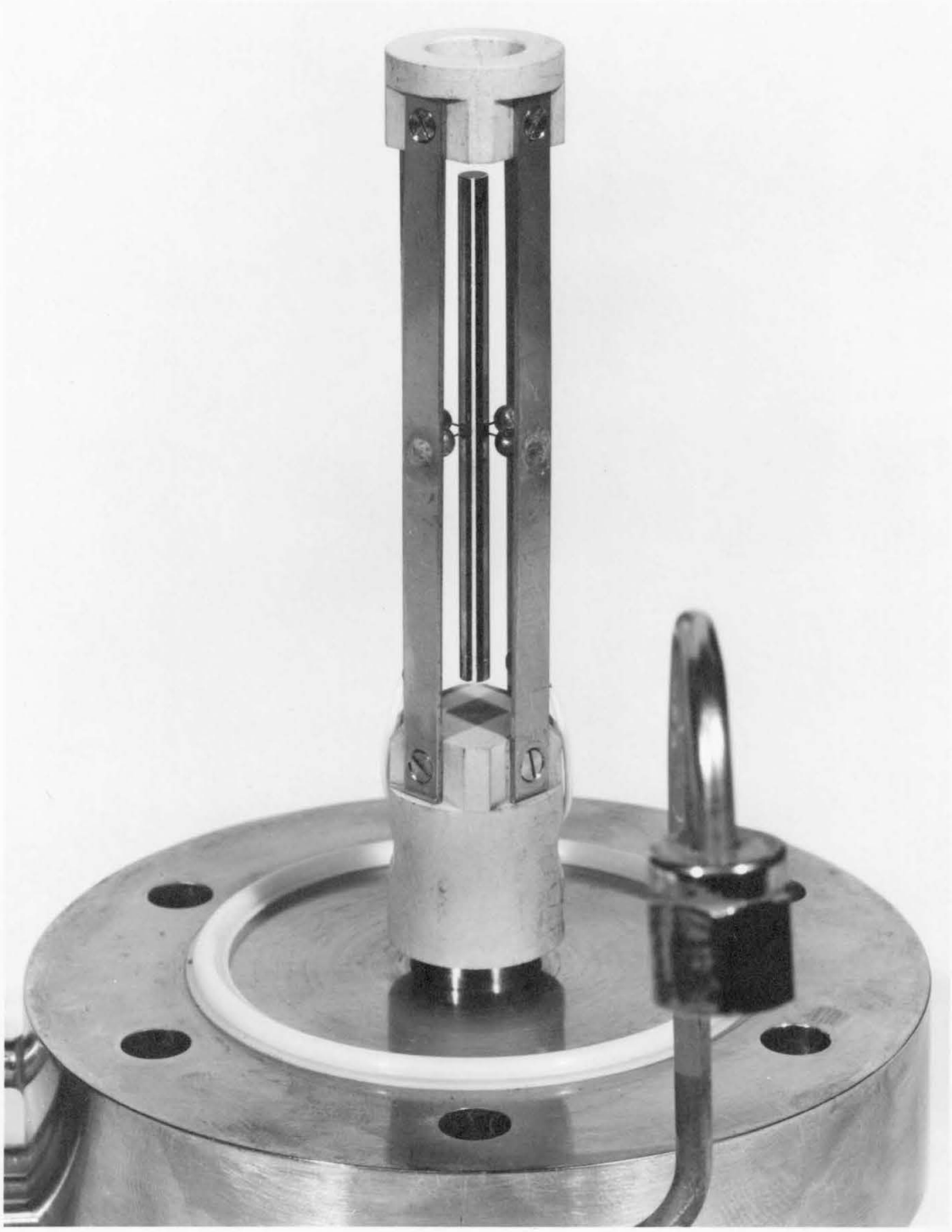

Figure 8. Torsional crystal and support

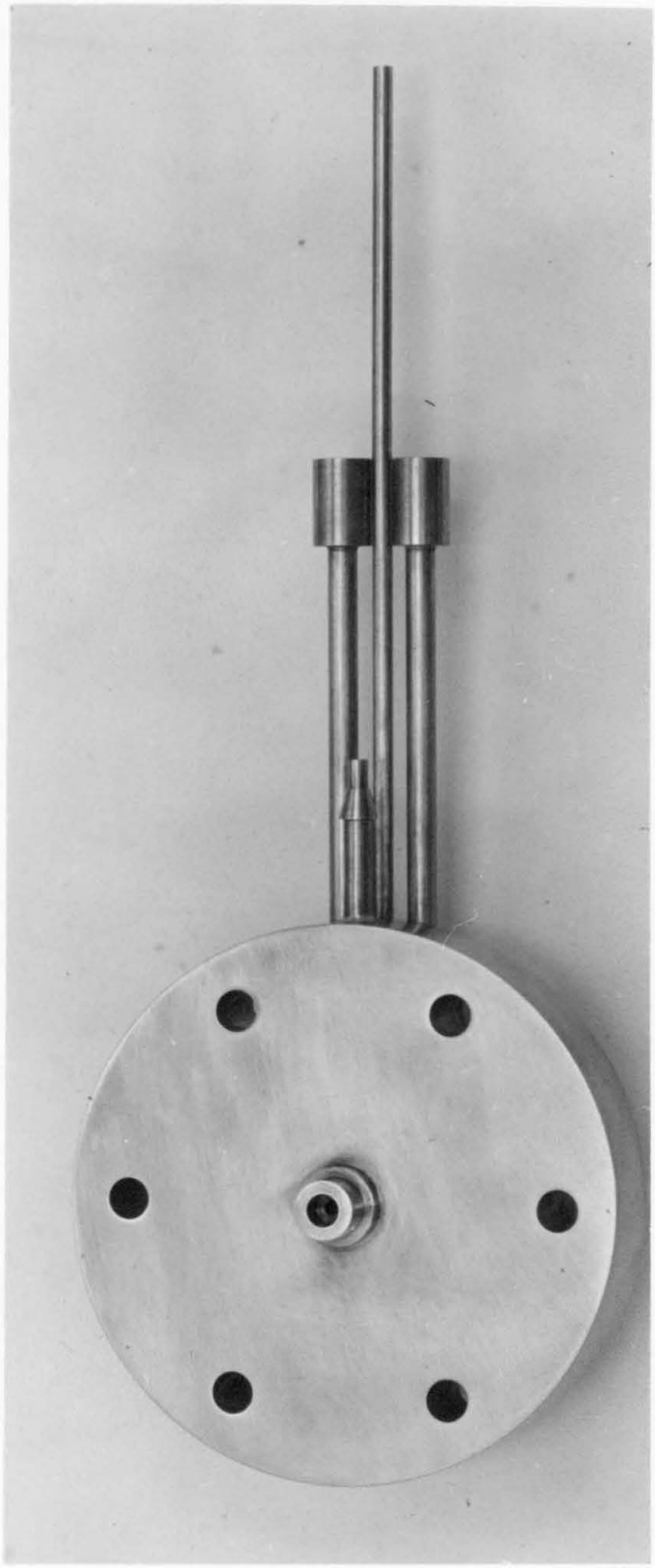

Figure 9. Inside view of flange

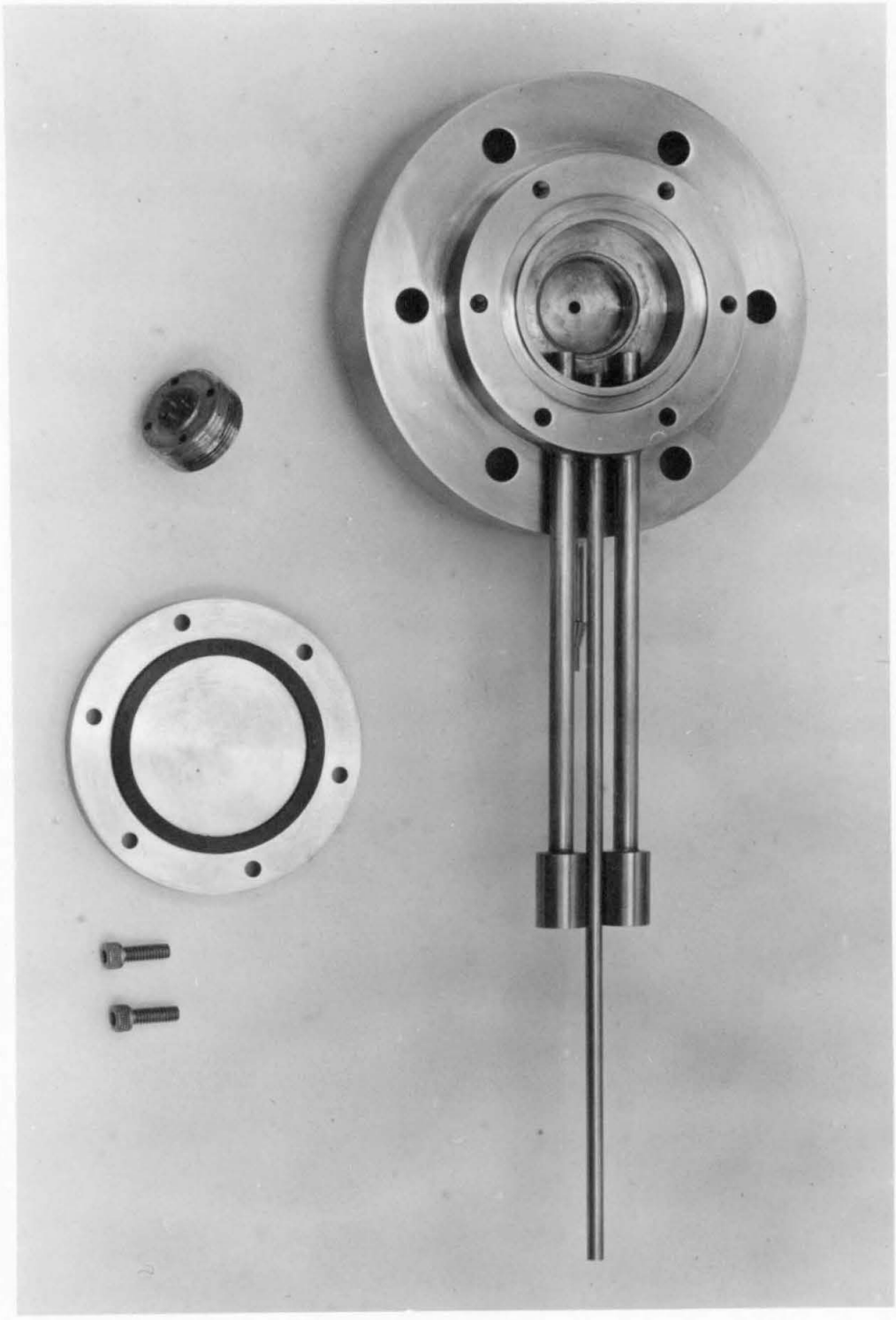

Figure 10. Back side view of flange and feed-through

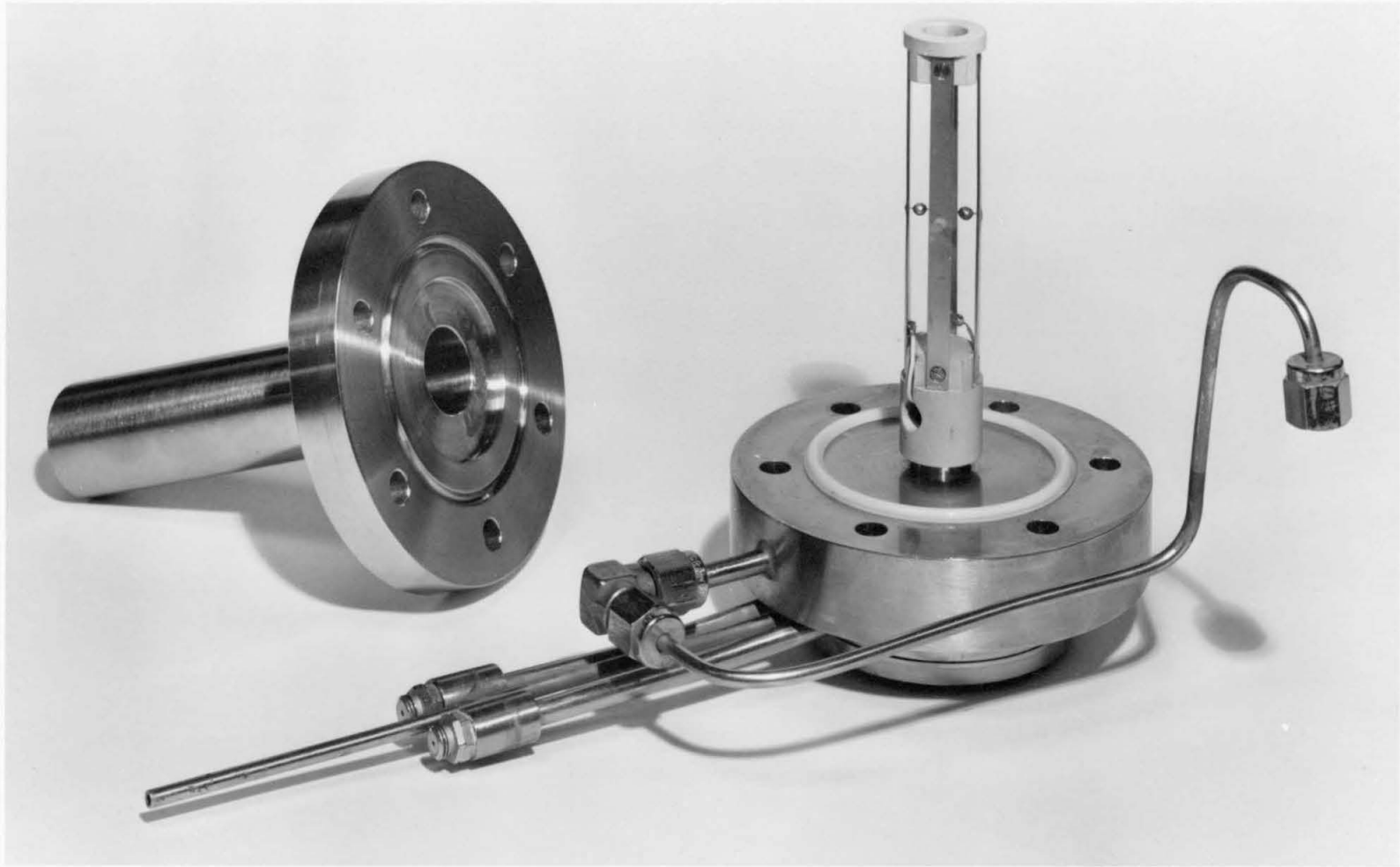

Figure 11. Crystal-cell assembly

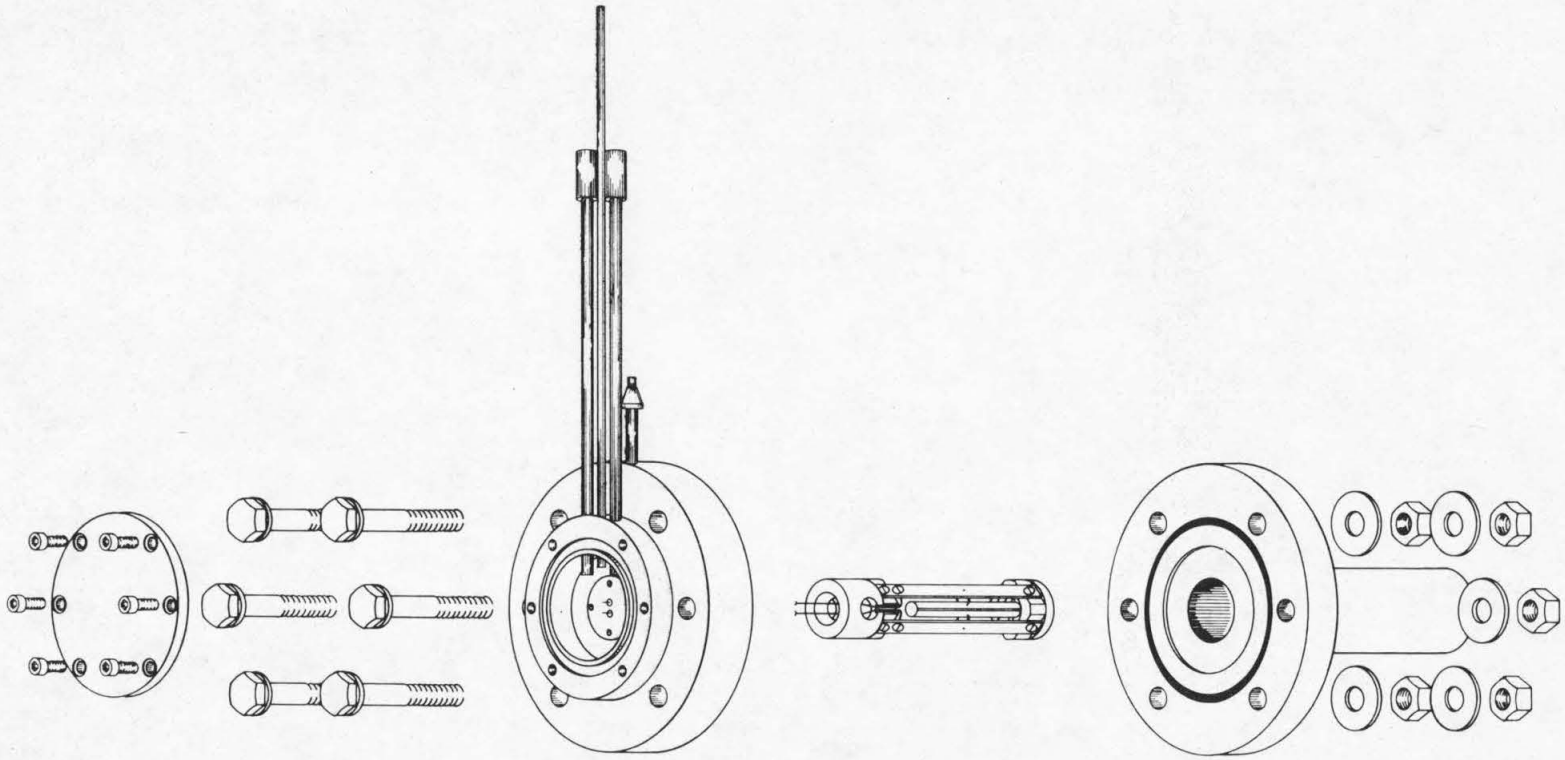

Figure 12. Exploded view of crystal and cell

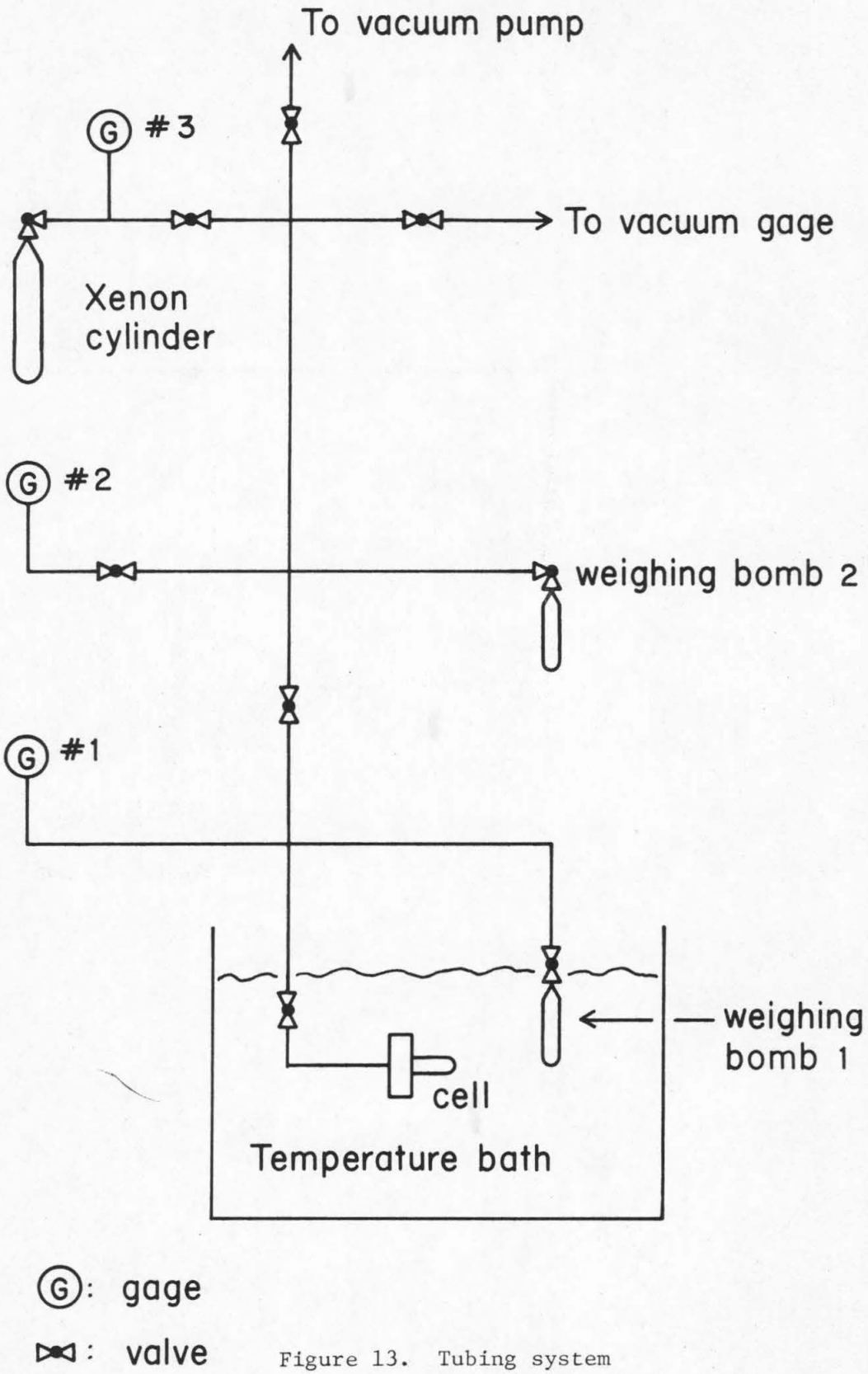

Figure 13. Tubing system

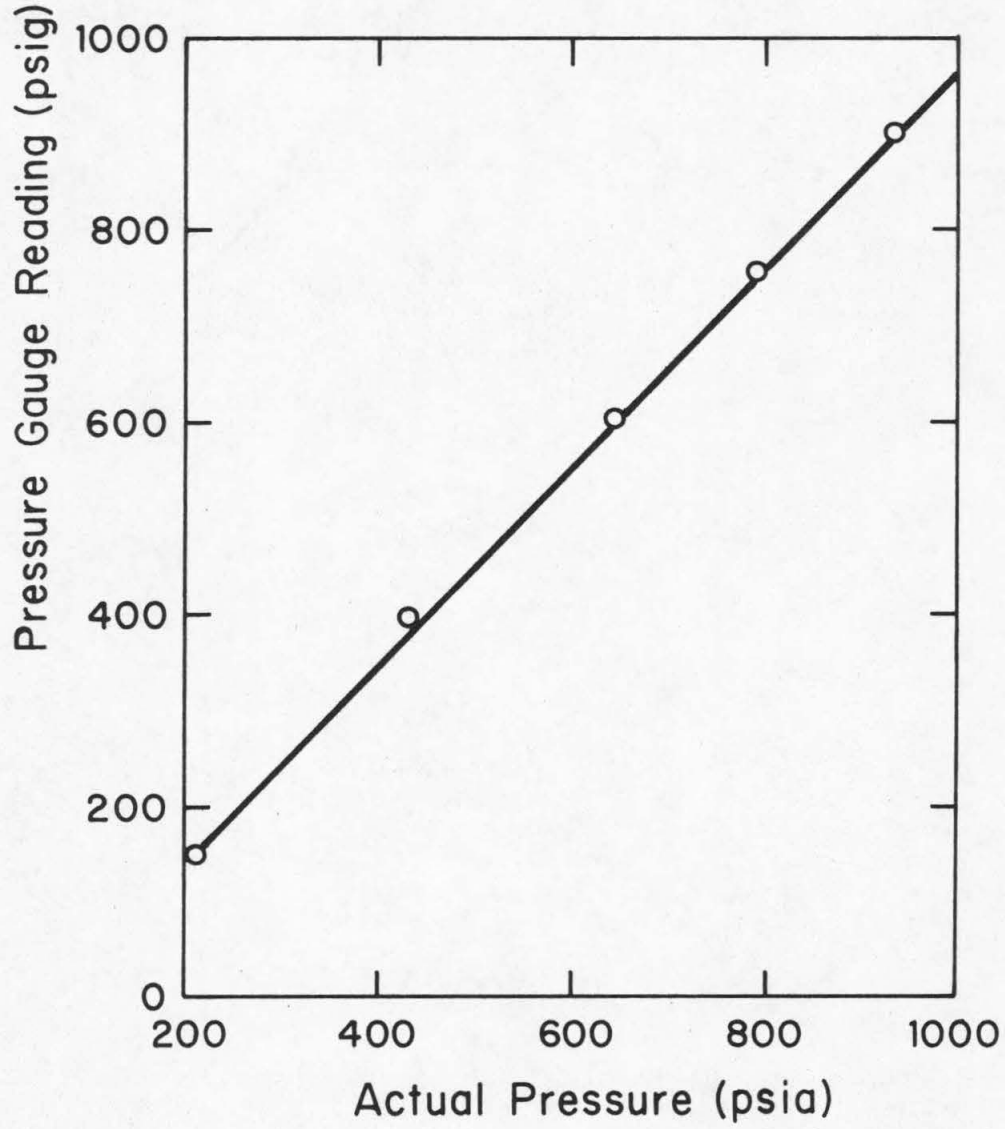

Figure 14. Calibration of pressure gauge #1

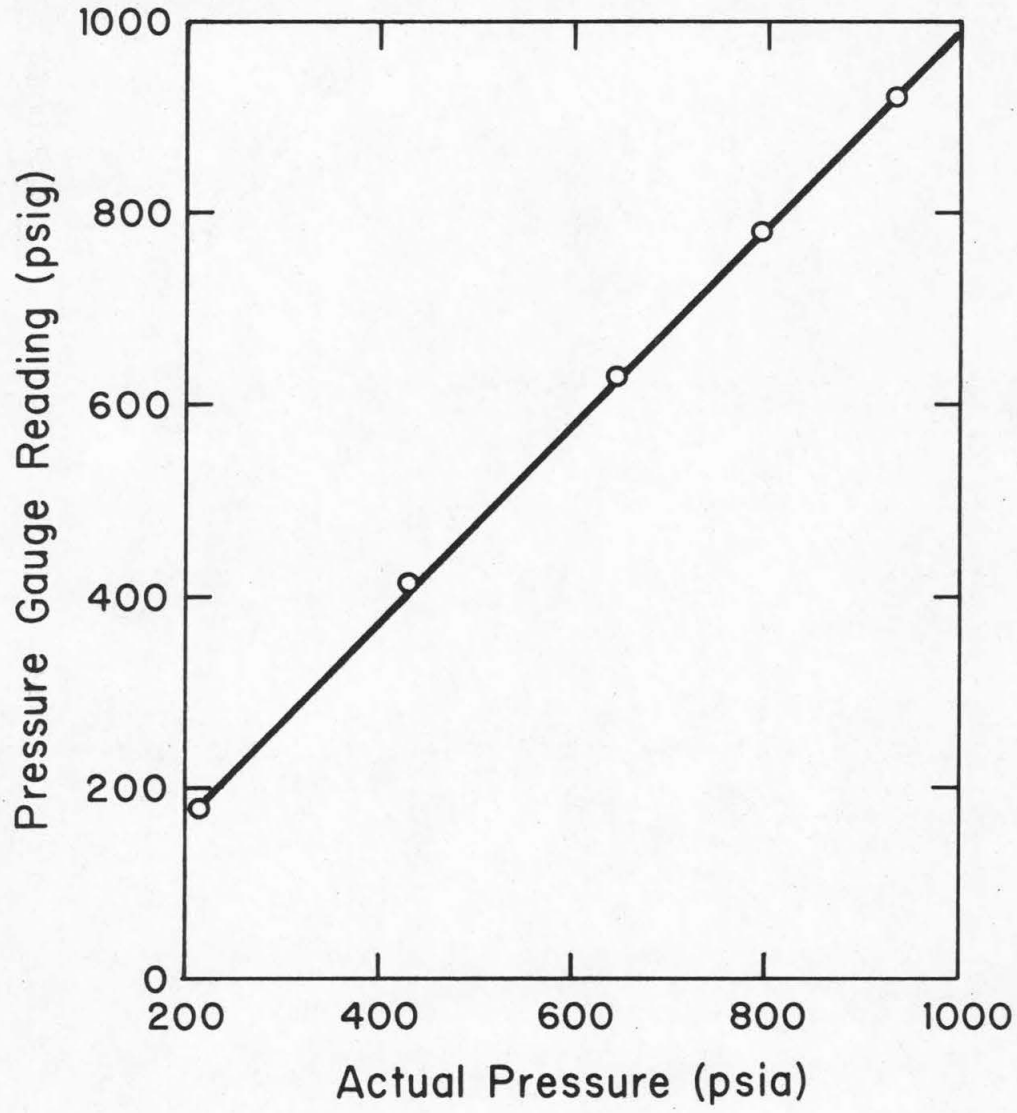

Figure 15. Calibration of pressure gauge #2

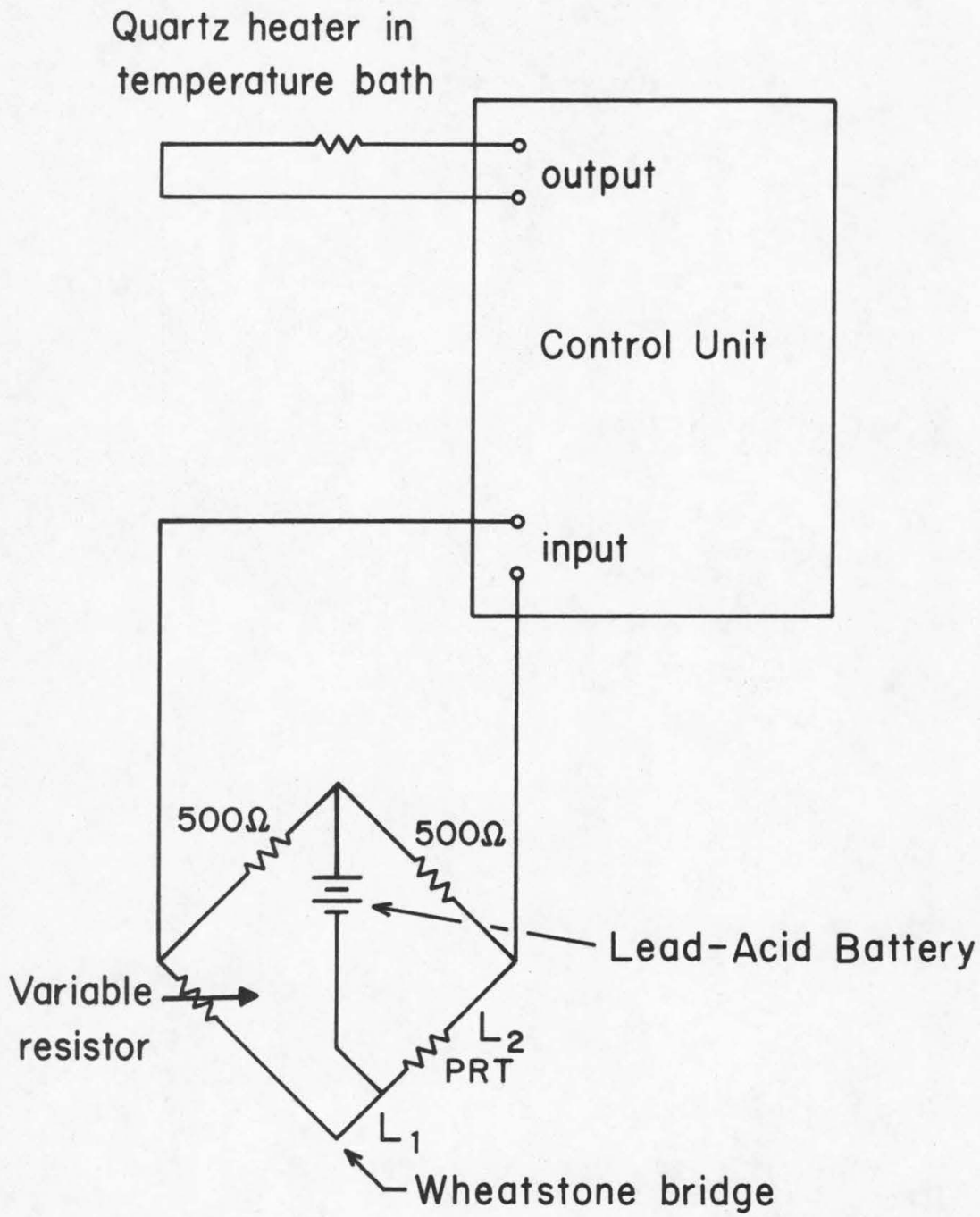

Figure 16. Temperature control circuit

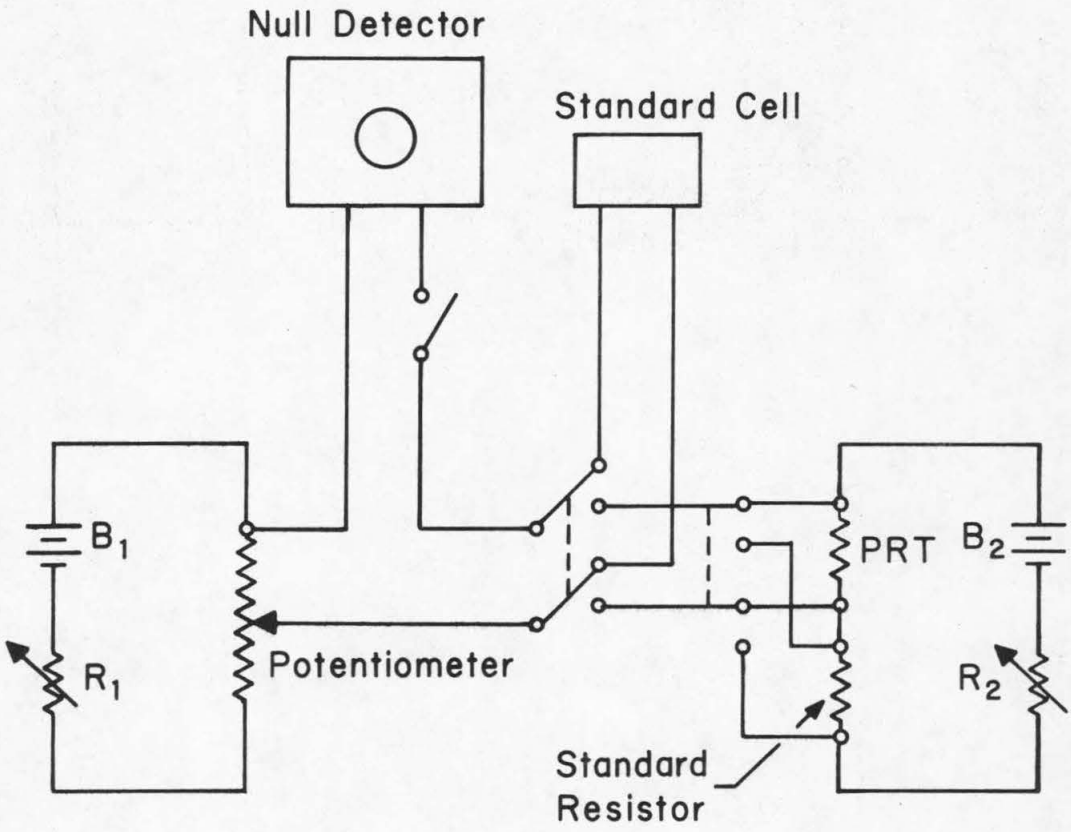

Figure 17. Temperature measuring circuit

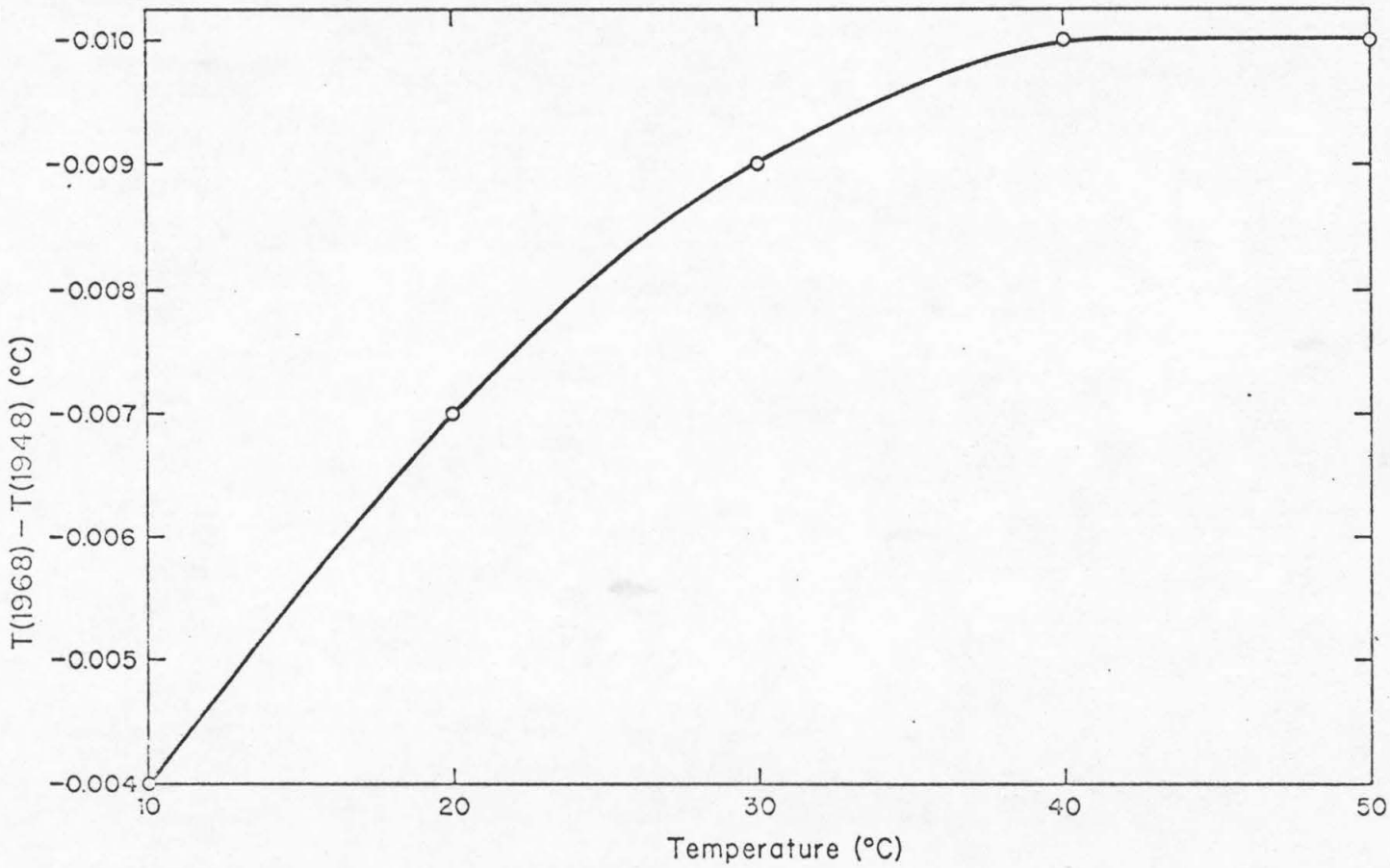

Figure 18. Relationship of 1968 IPTS to 1948 ITS

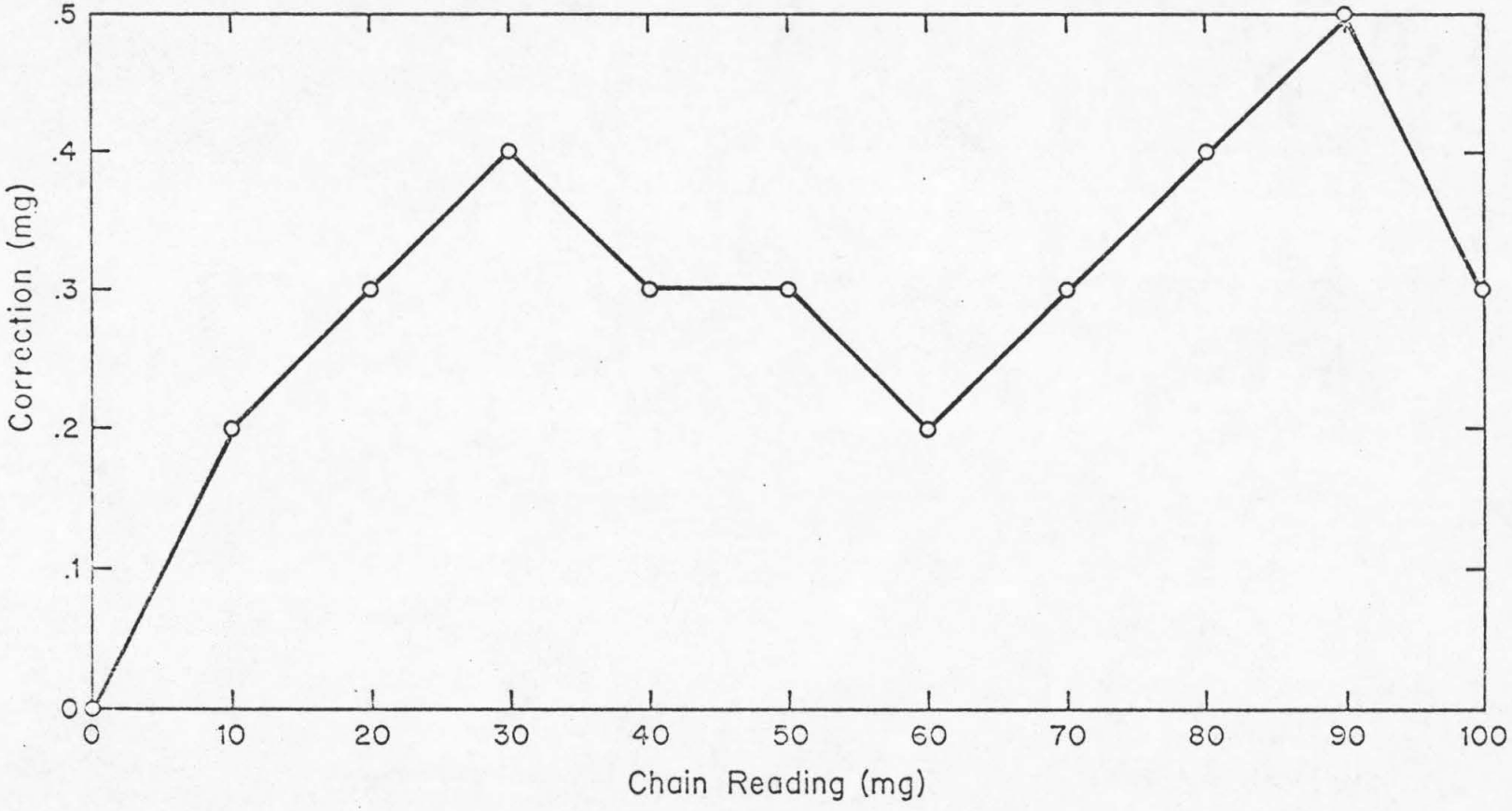

Figure 19. Calibration of analytical balance chain

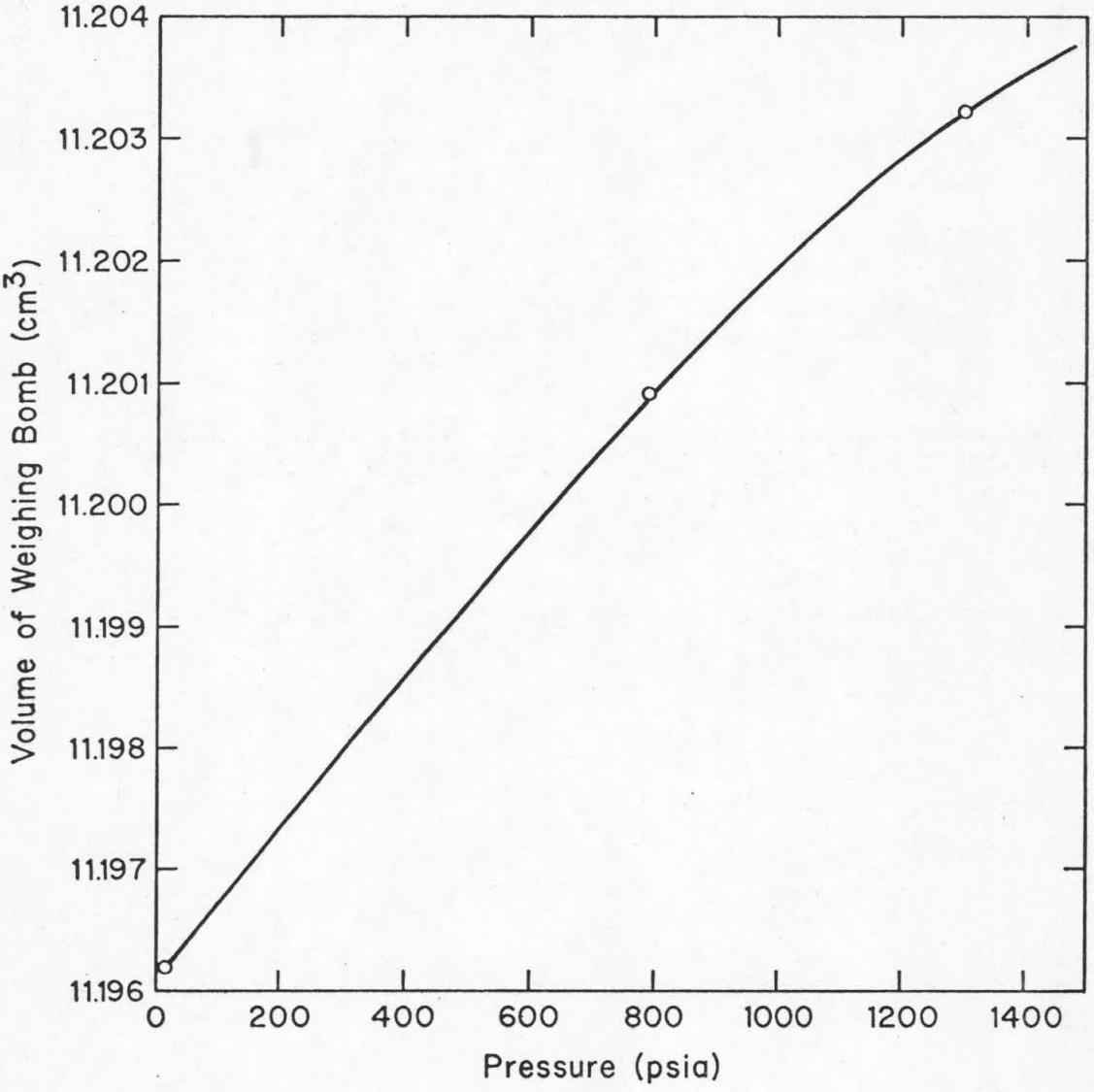

Figure 20. Volume of weighing bomb #1 as a function of pressure at 30°C

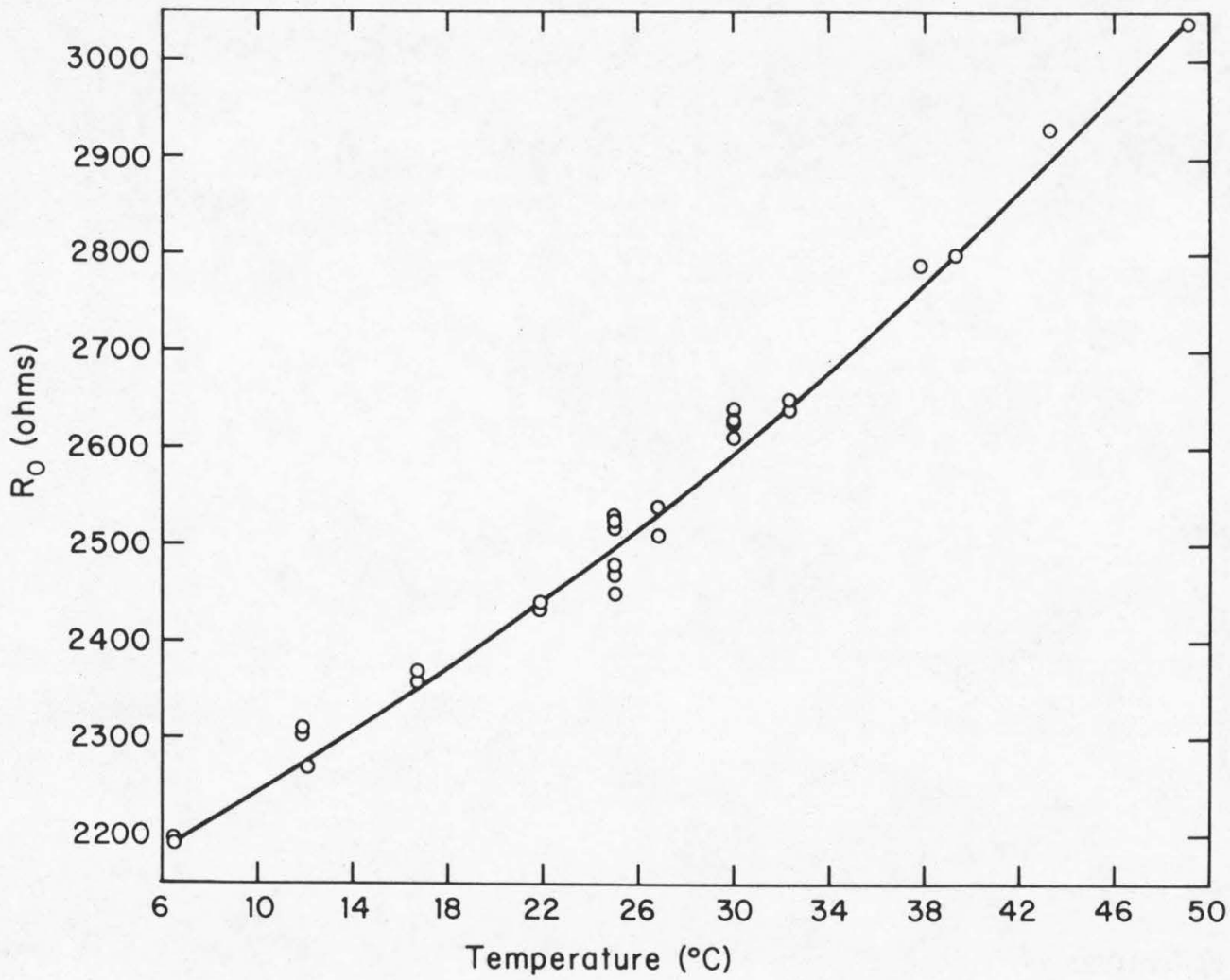

Figure 21. Resonant resistance in a vacuum as a function of temperature

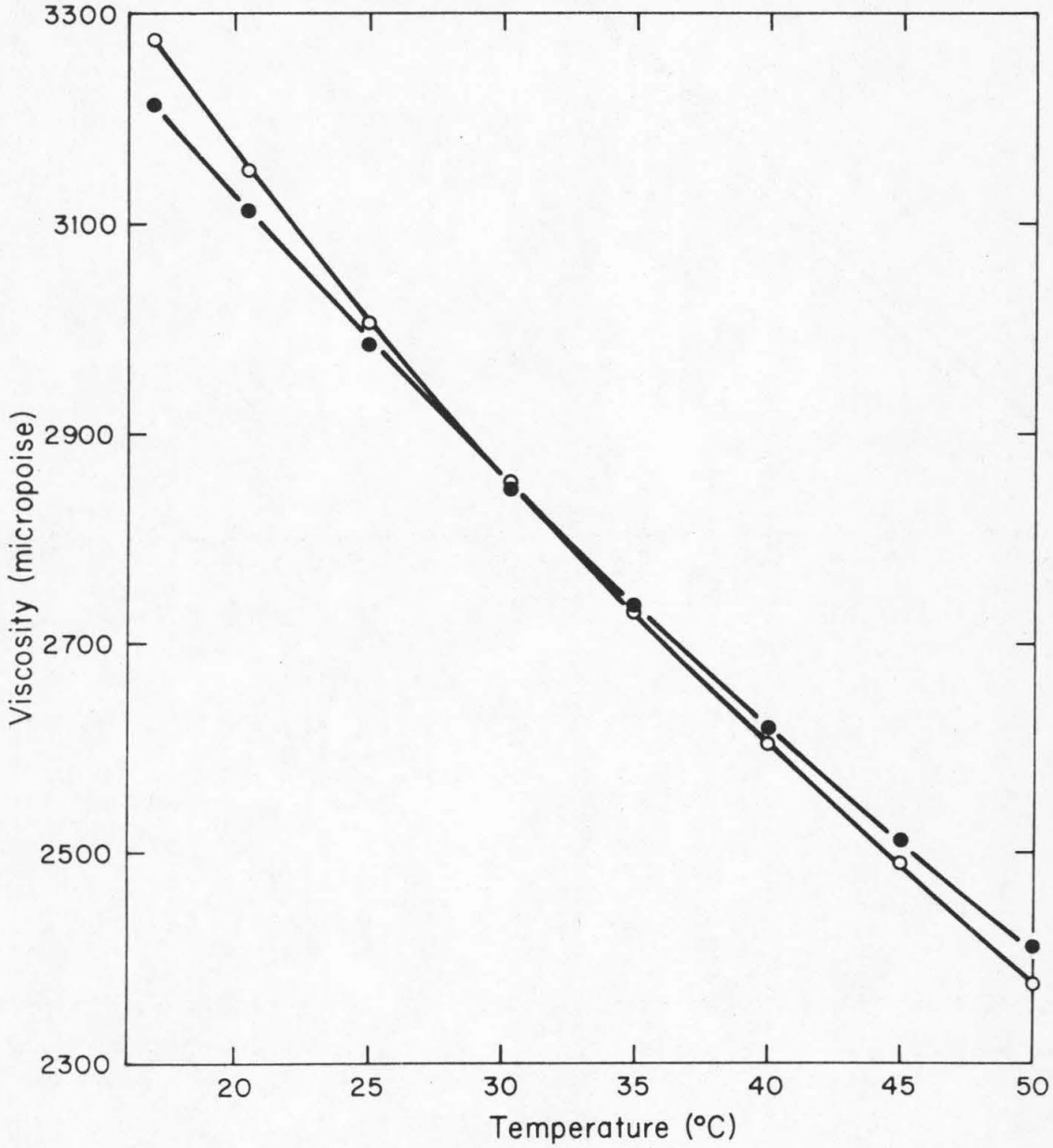

Figure 22. Viscosity of normal-hexane at atmospheric pressure
○ this investigation
● API Research Project 44[43]

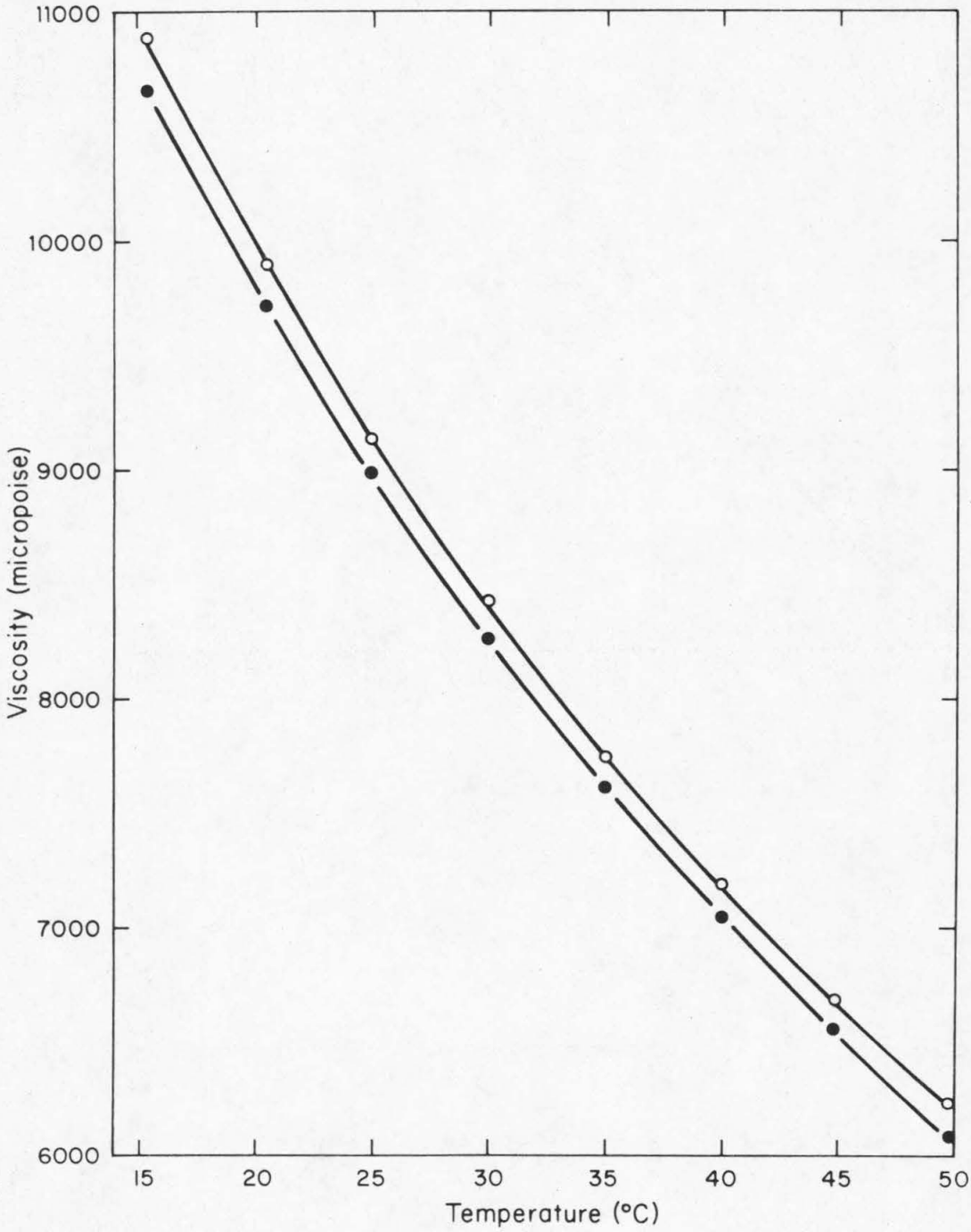

Figure 23. Viscosity of cyclohexane at atmospheric pressure
○ this investigation
● API Research Project 44[43]

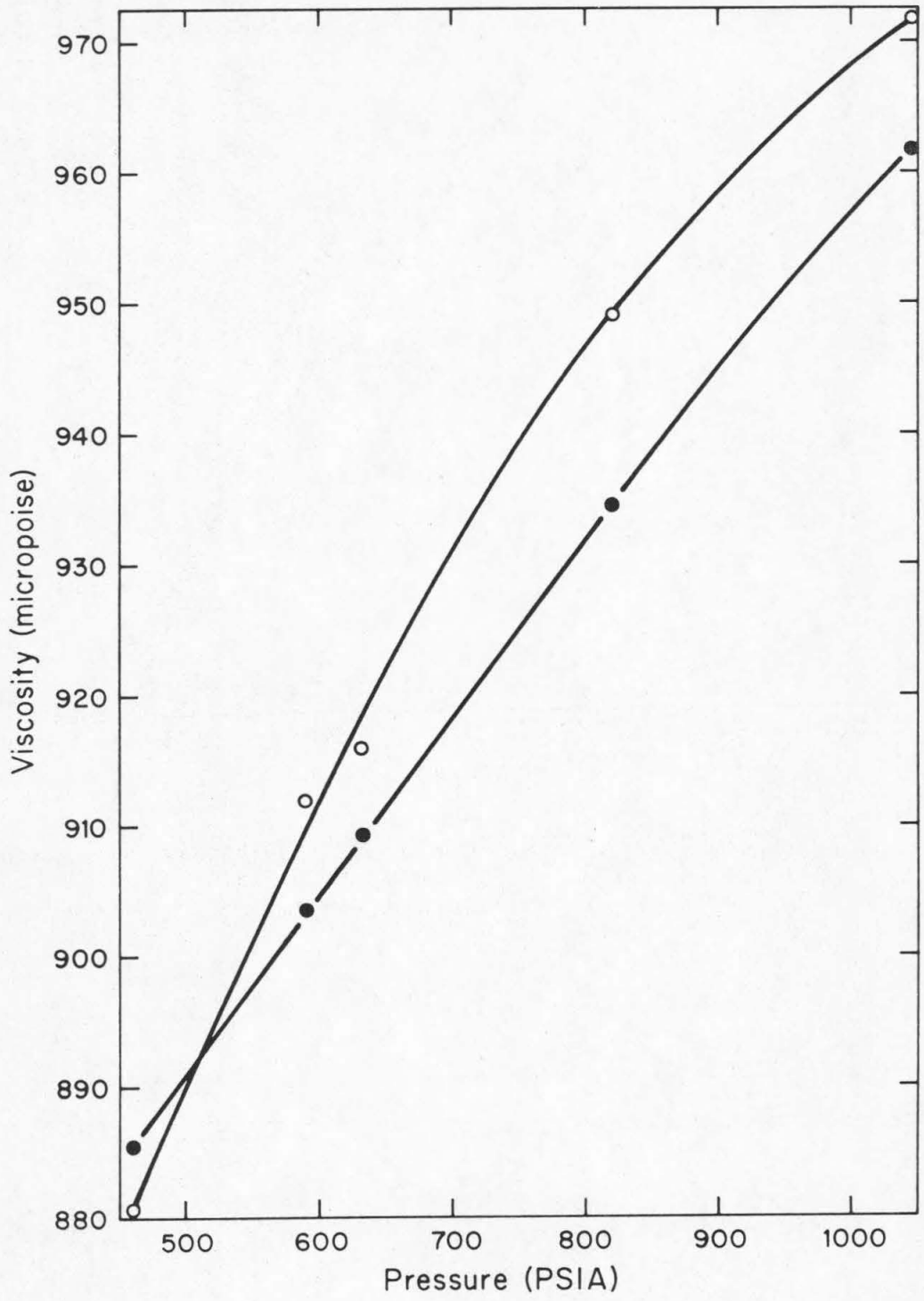

Figure 24. Viscosity of propane at 100°F (37.778°C)
○ this investigation
● Carmichael, et al.[45]

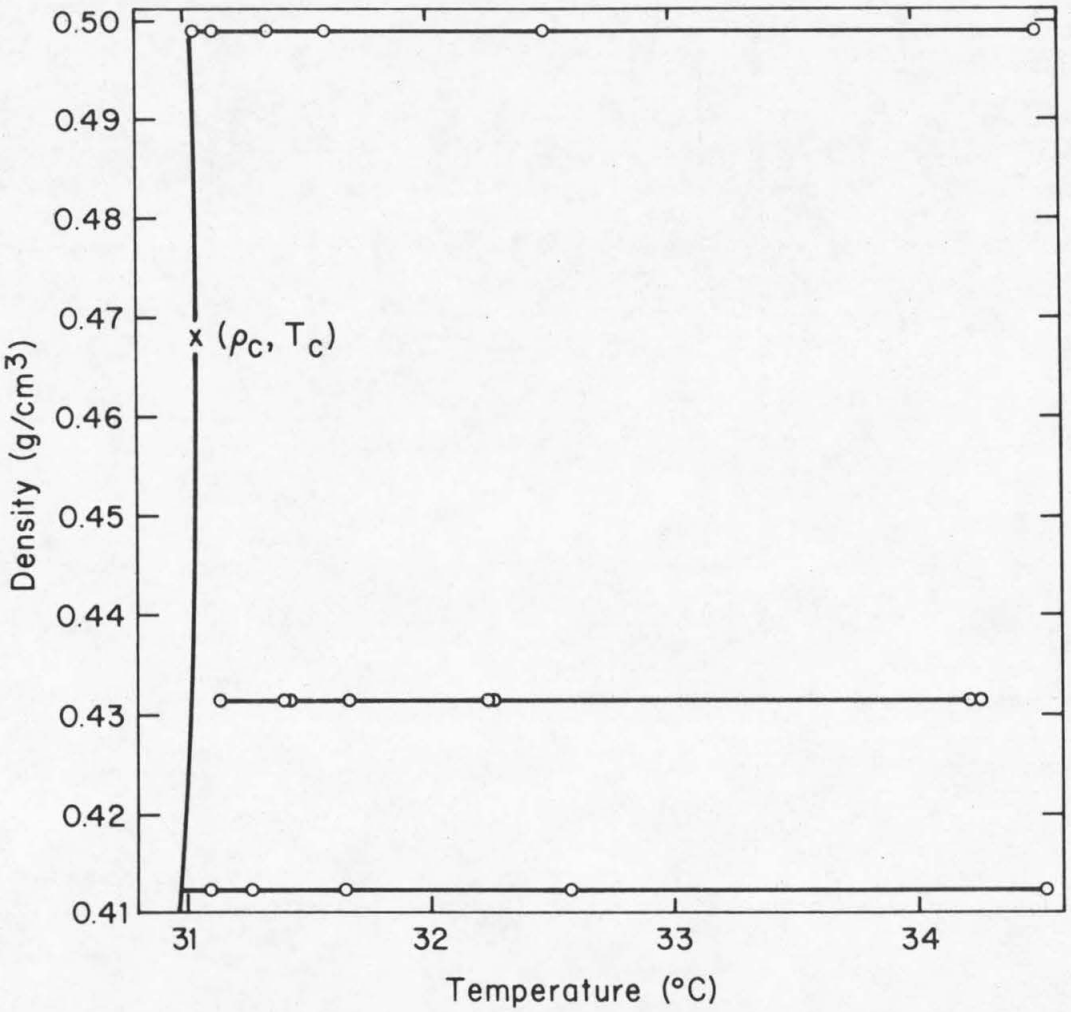

Figure 25. Location of carbon dioxide data points

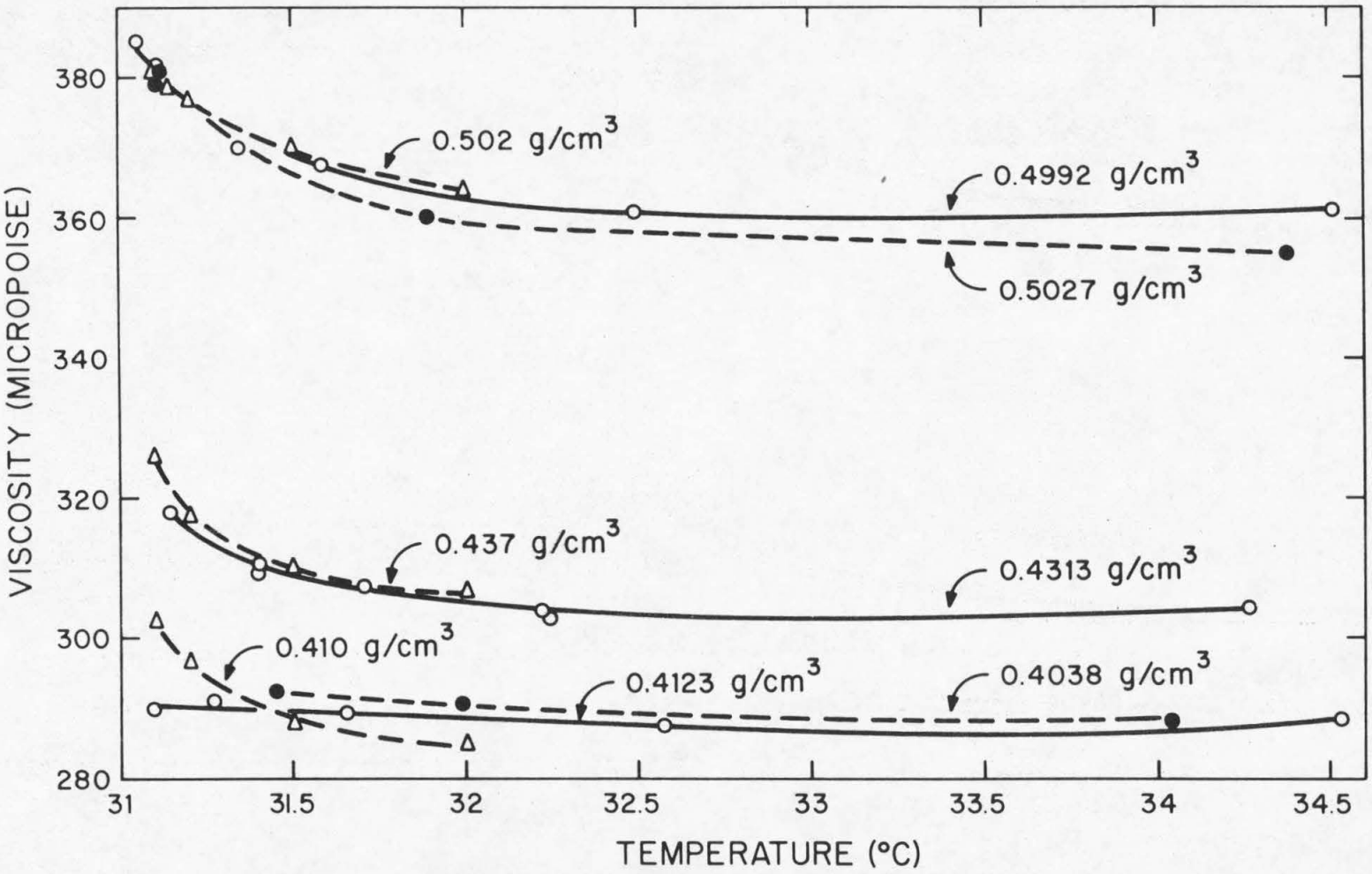

Figure 26. Viscosity of carbon dioxide along isochores
○ this investigation
△ Naldrett and Maass[12]
● Kestin, et al.[13]

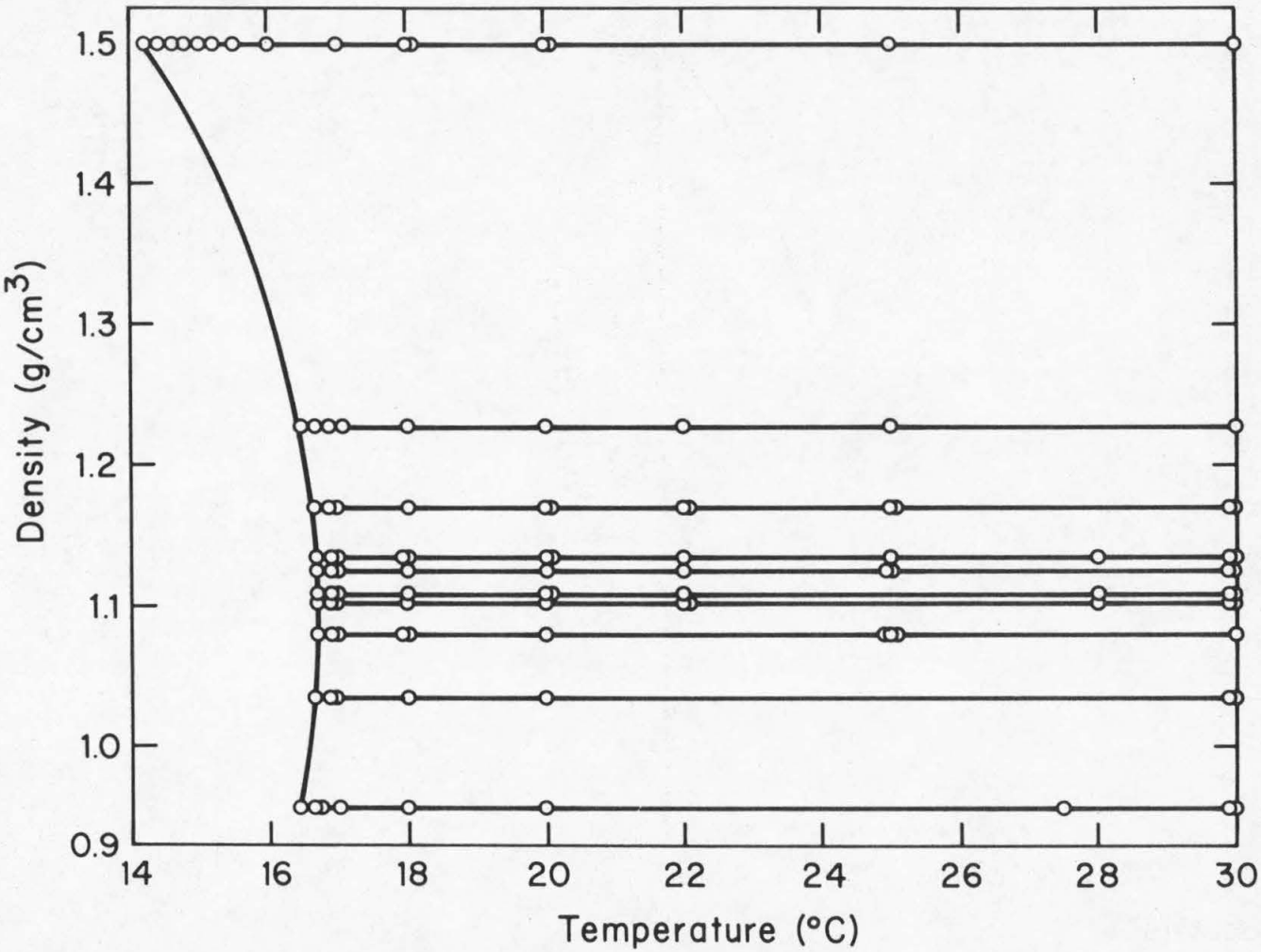

Figure 27. Location of xenon data points

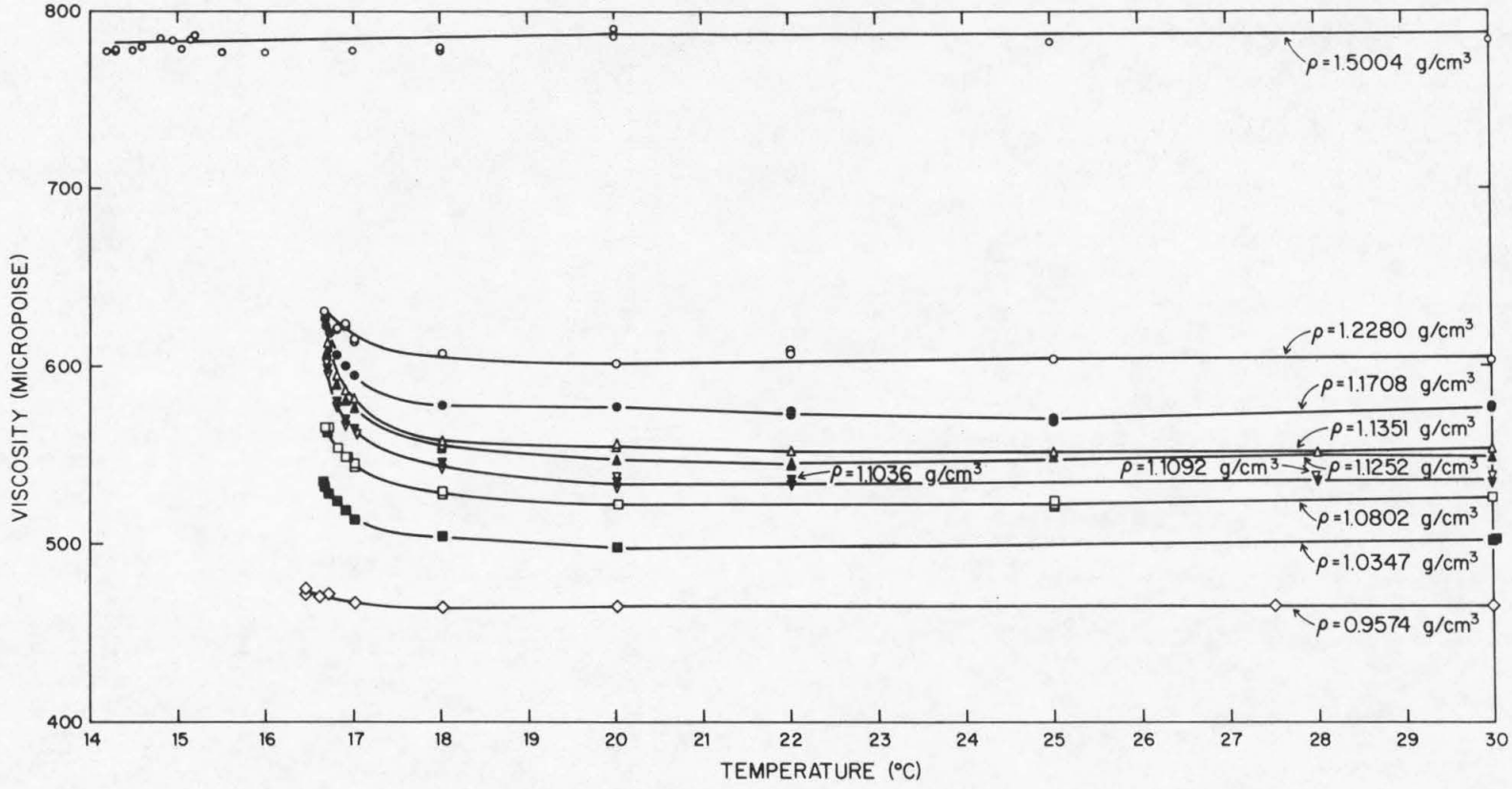

Figure 28. Viscosity of xenon along isochores

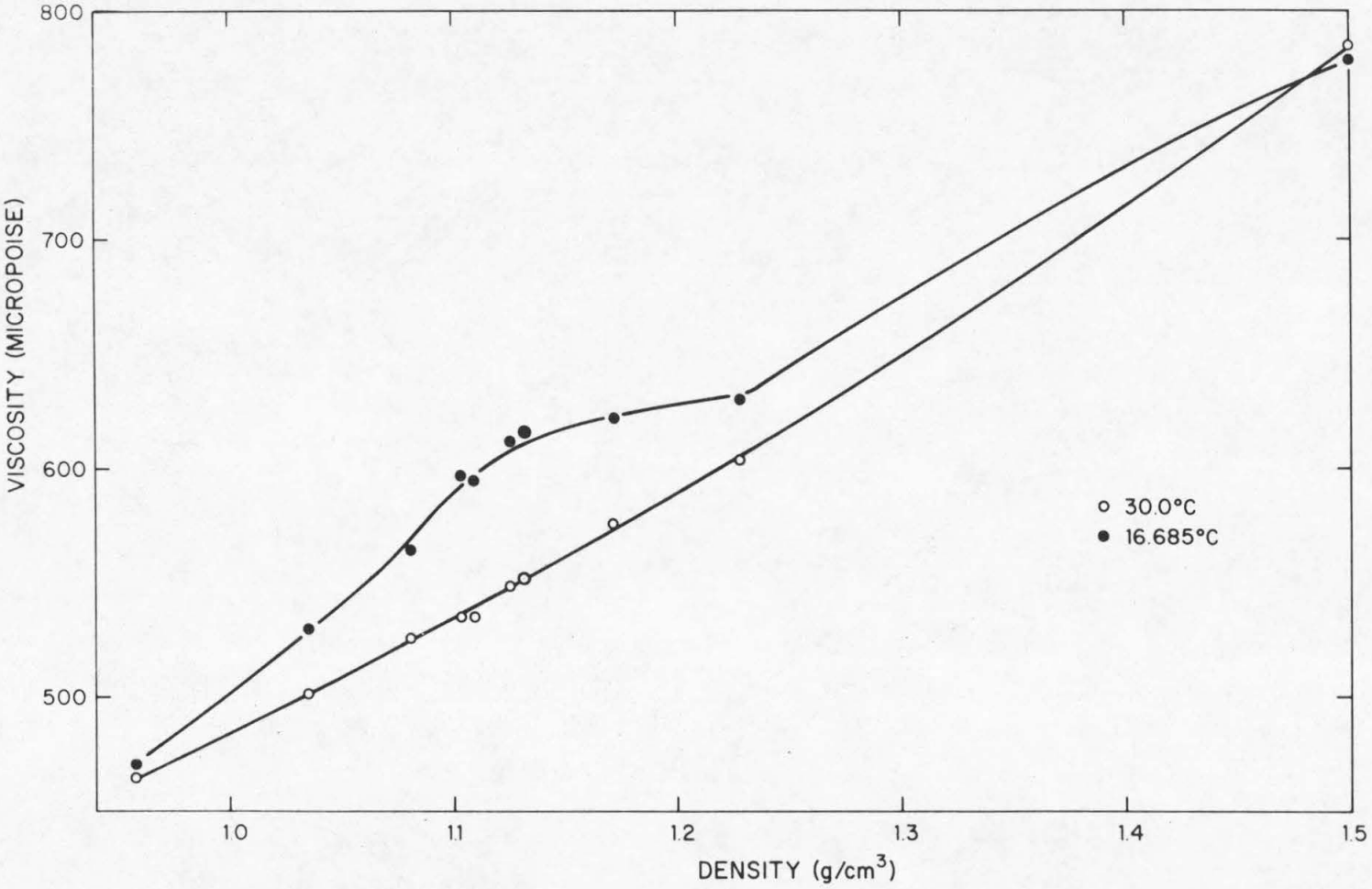

Figure 29. Viscosity of xenon along two isotherms at 30.0°C and 16.685°C

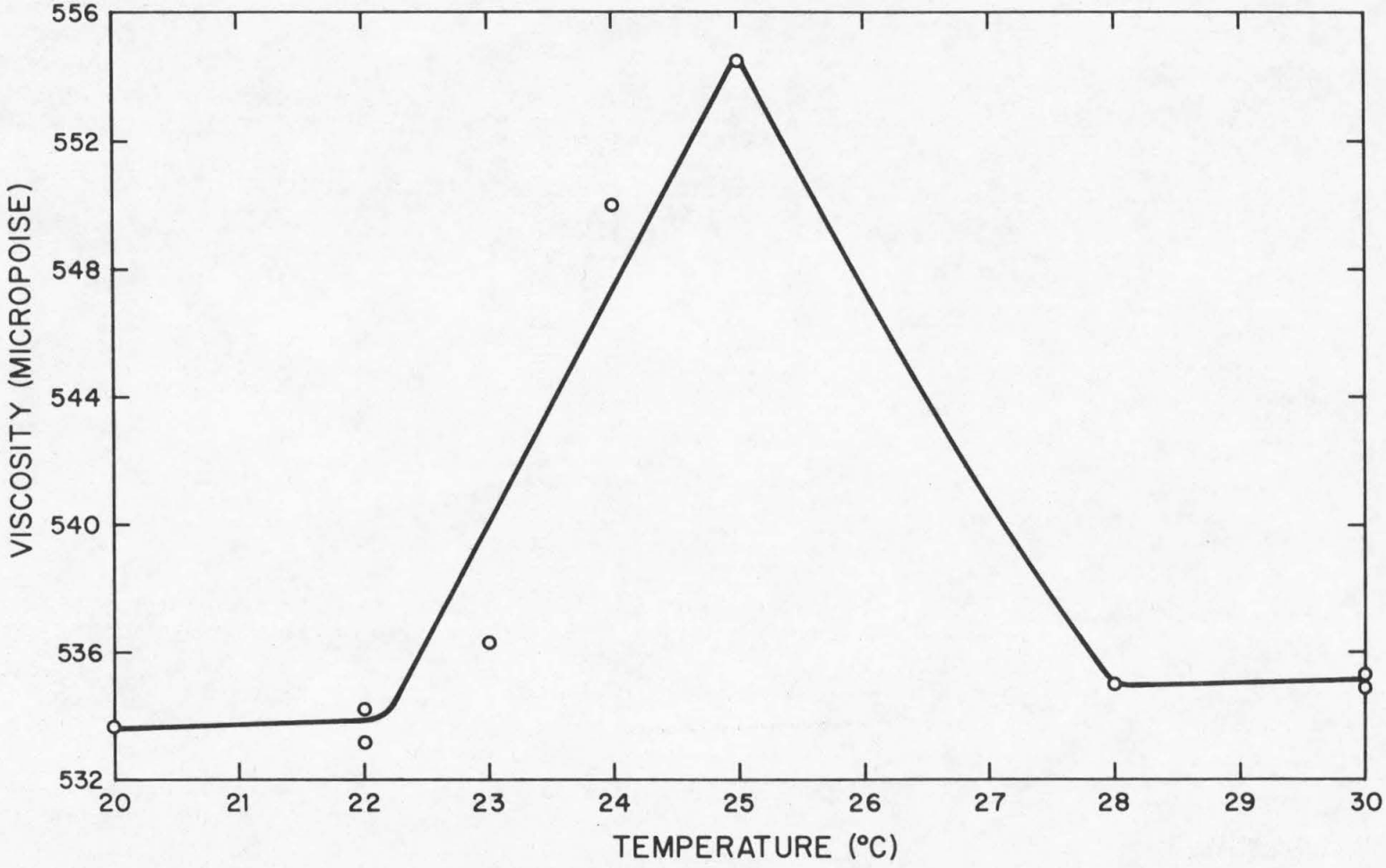

Figure 30. Spurious viscosities for xenon isochore at $\rho = 1.1036$ g/cm^3

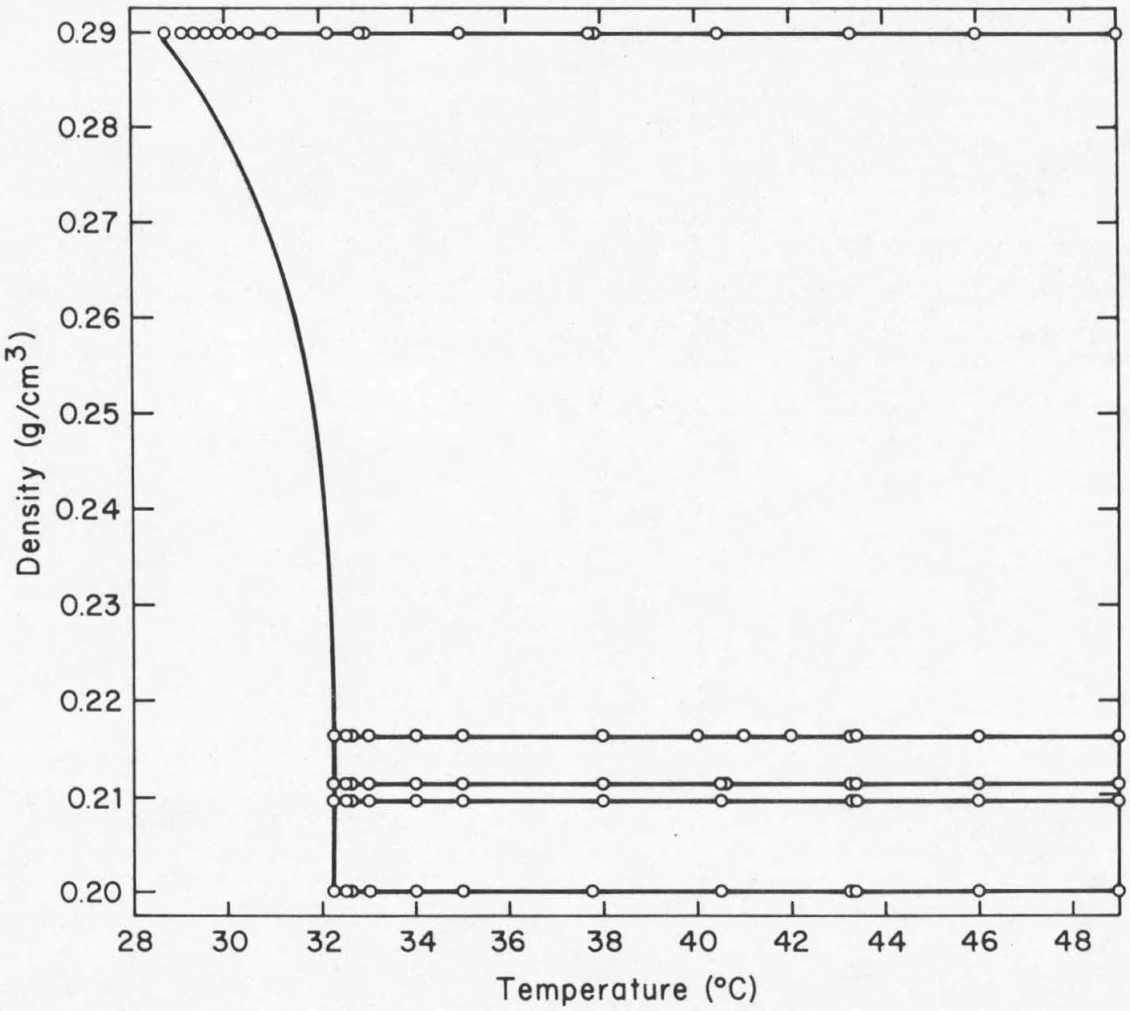

Figure 31. Location of ethane data points

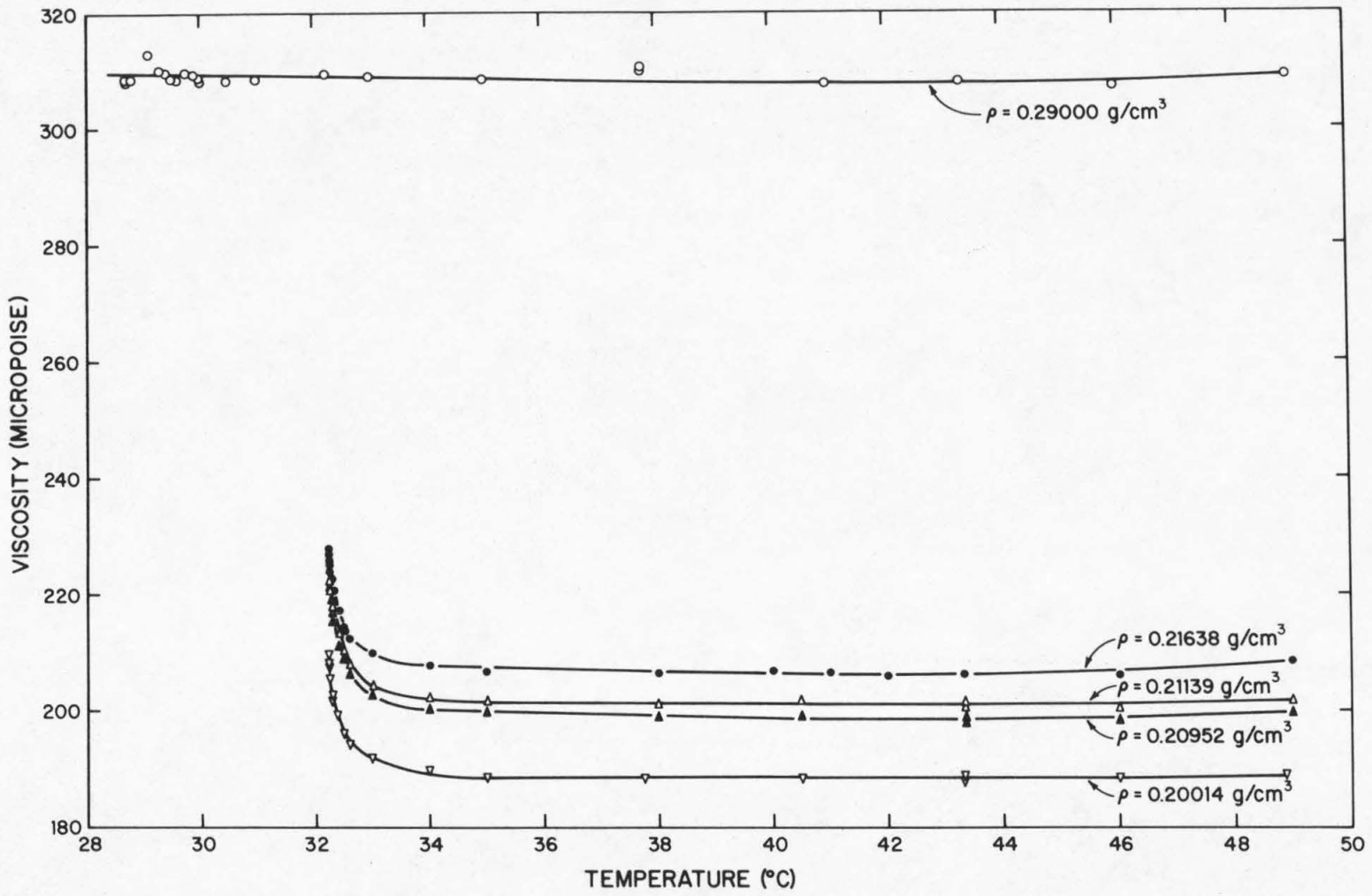

Figure 32. Viscosity of ethane along isochores

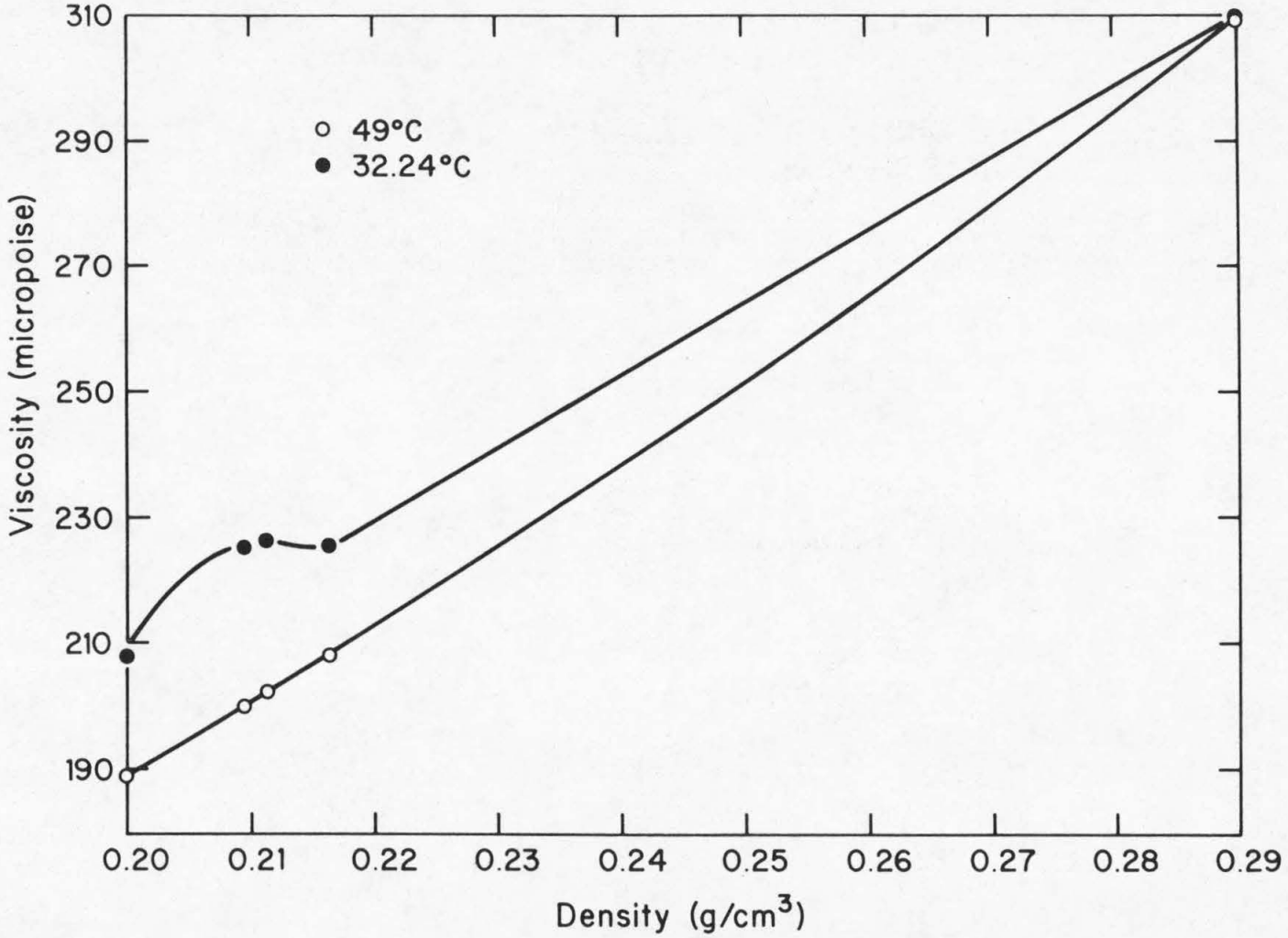

Figure 33. Viscosity of ethane along isotherms at 49°C and 32.24°C

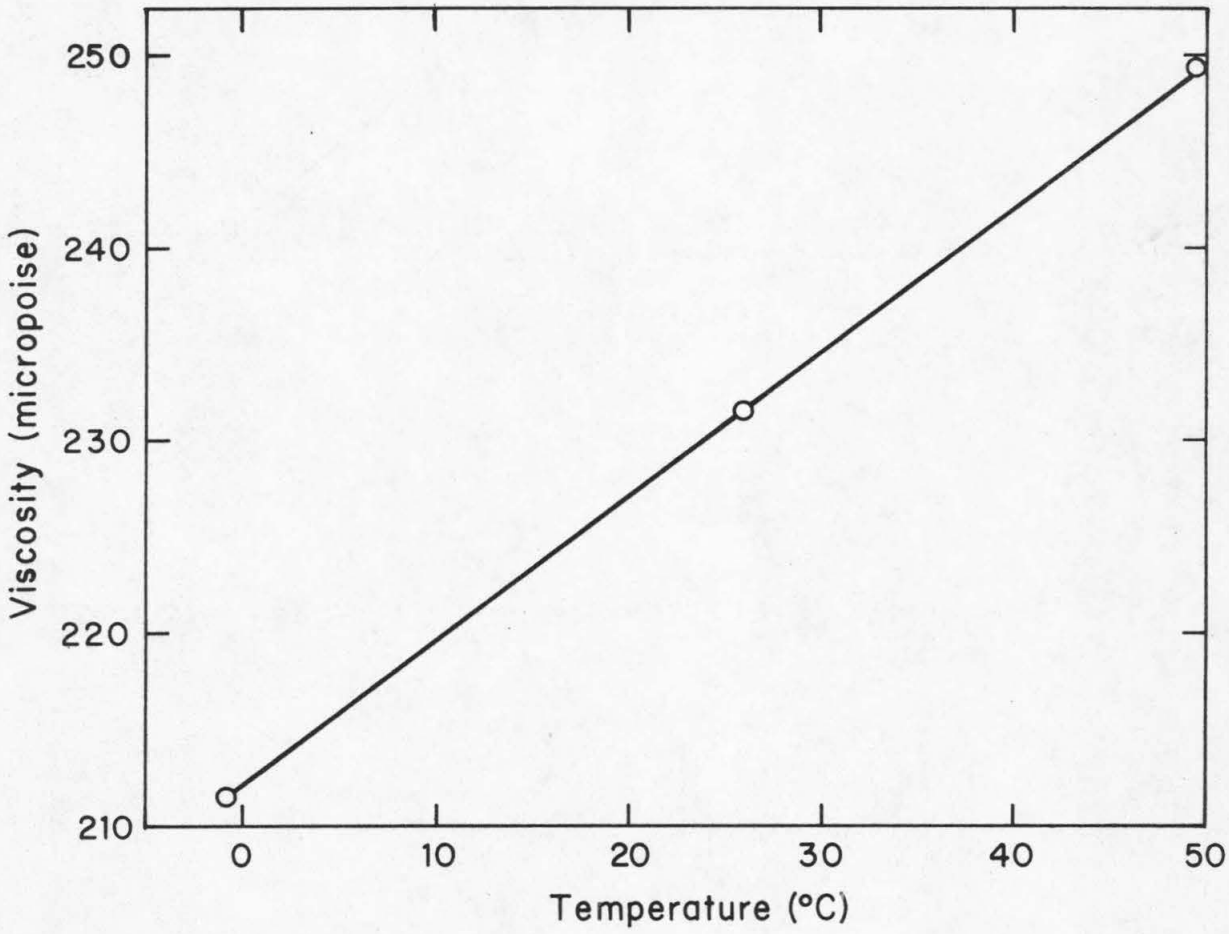

Figure 34. Zero density xenon viscosity from Clarke and Smith[52]

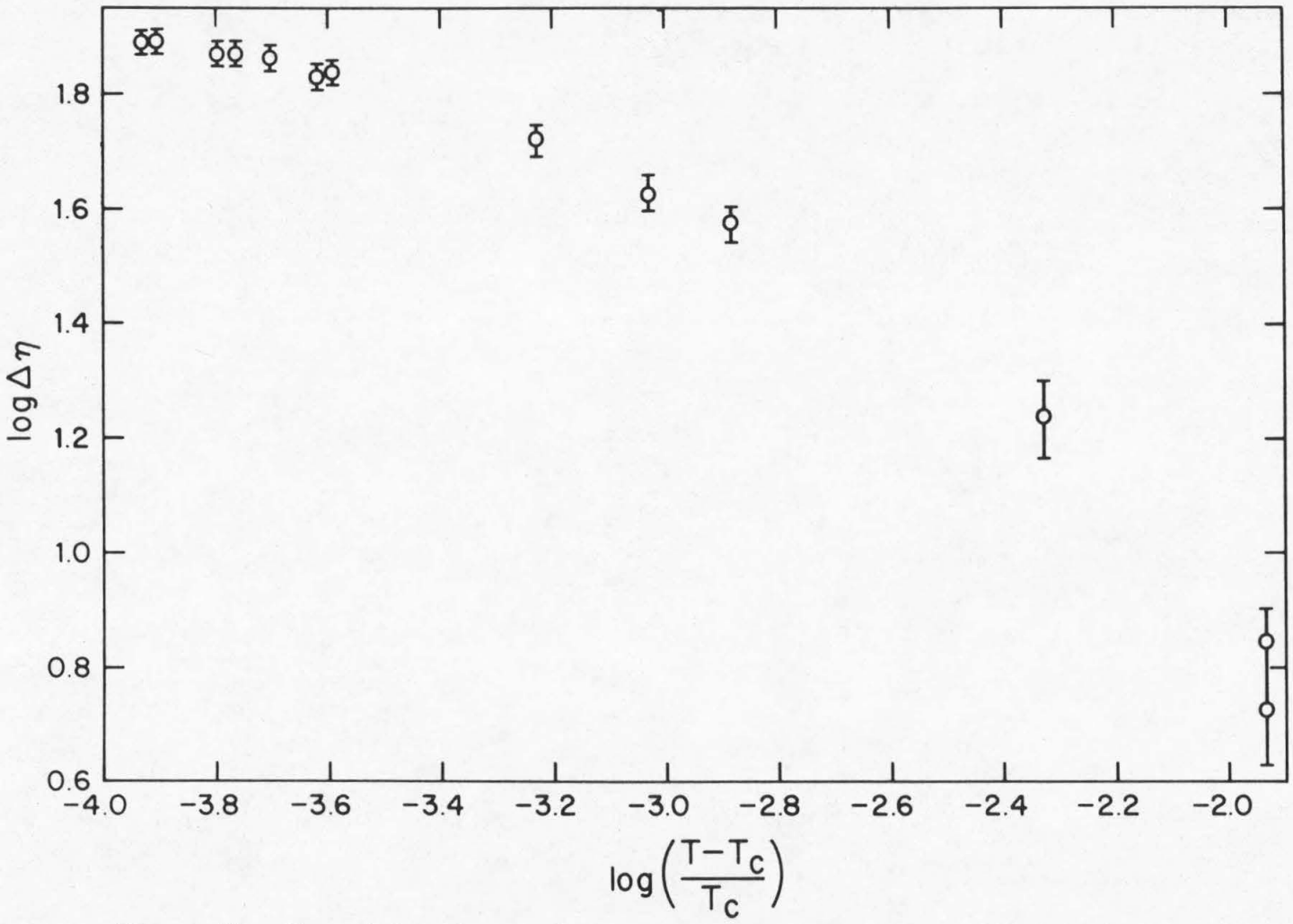

Figure 35. Logarithm of anomalous viscosity vs. logarithm of reduced temperature difference for xenon isochore at $\rho = 1.1092$ g/cm^3

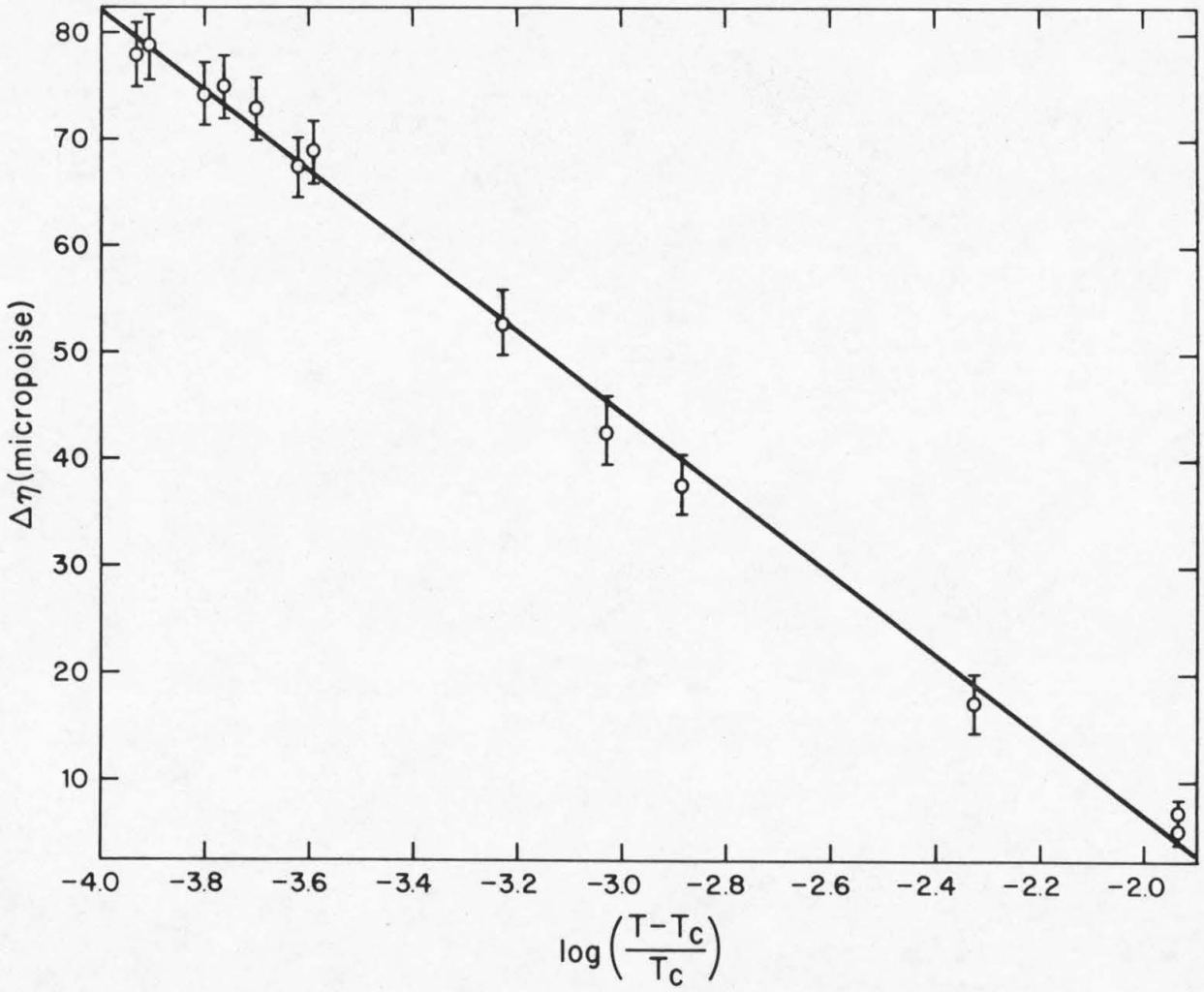

Figure 36. Anomalous viscosity vs. logarithm of reduced temperature difference for xenon isochore at $\rho = 1.1092$ g/cm^3

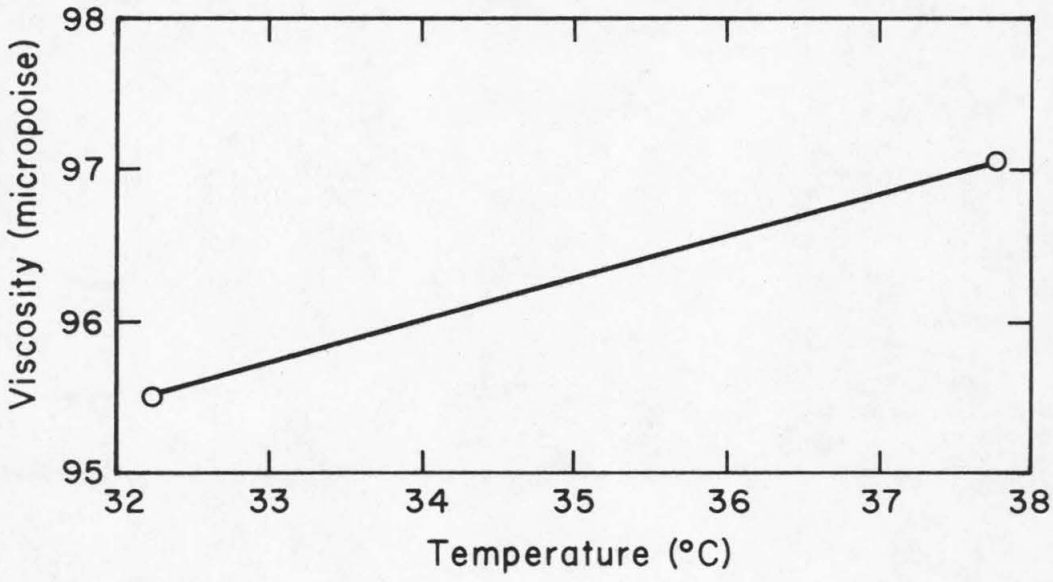

Figure 37. Zero density ethane viscosity from Carmichael and Sage[50]

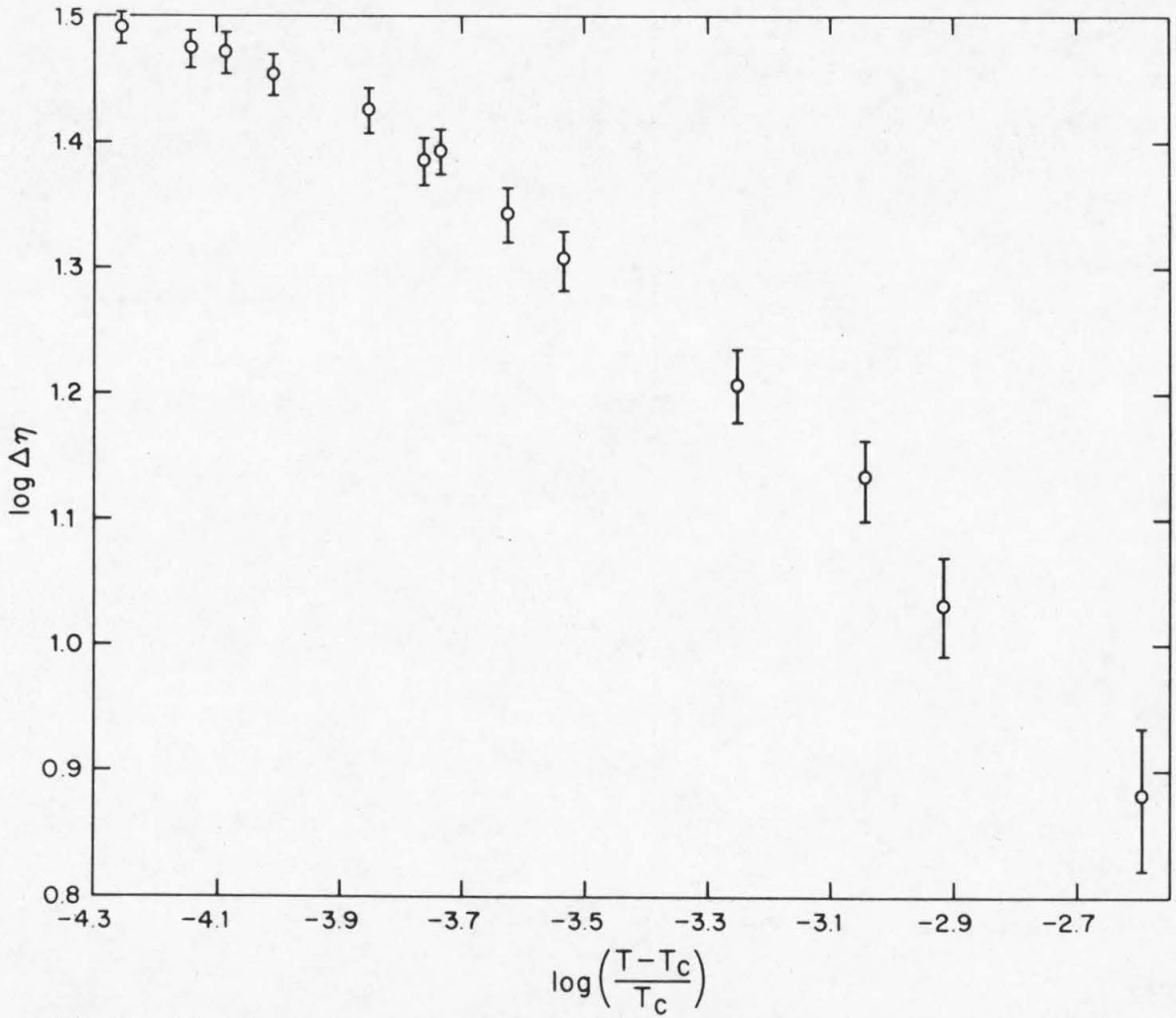

Figure 38. Logarithm of anomalous viscosity vs. logarithm of reduced temperature difference for ethane isochore at $\rho = 0.20952$ g/cm^3

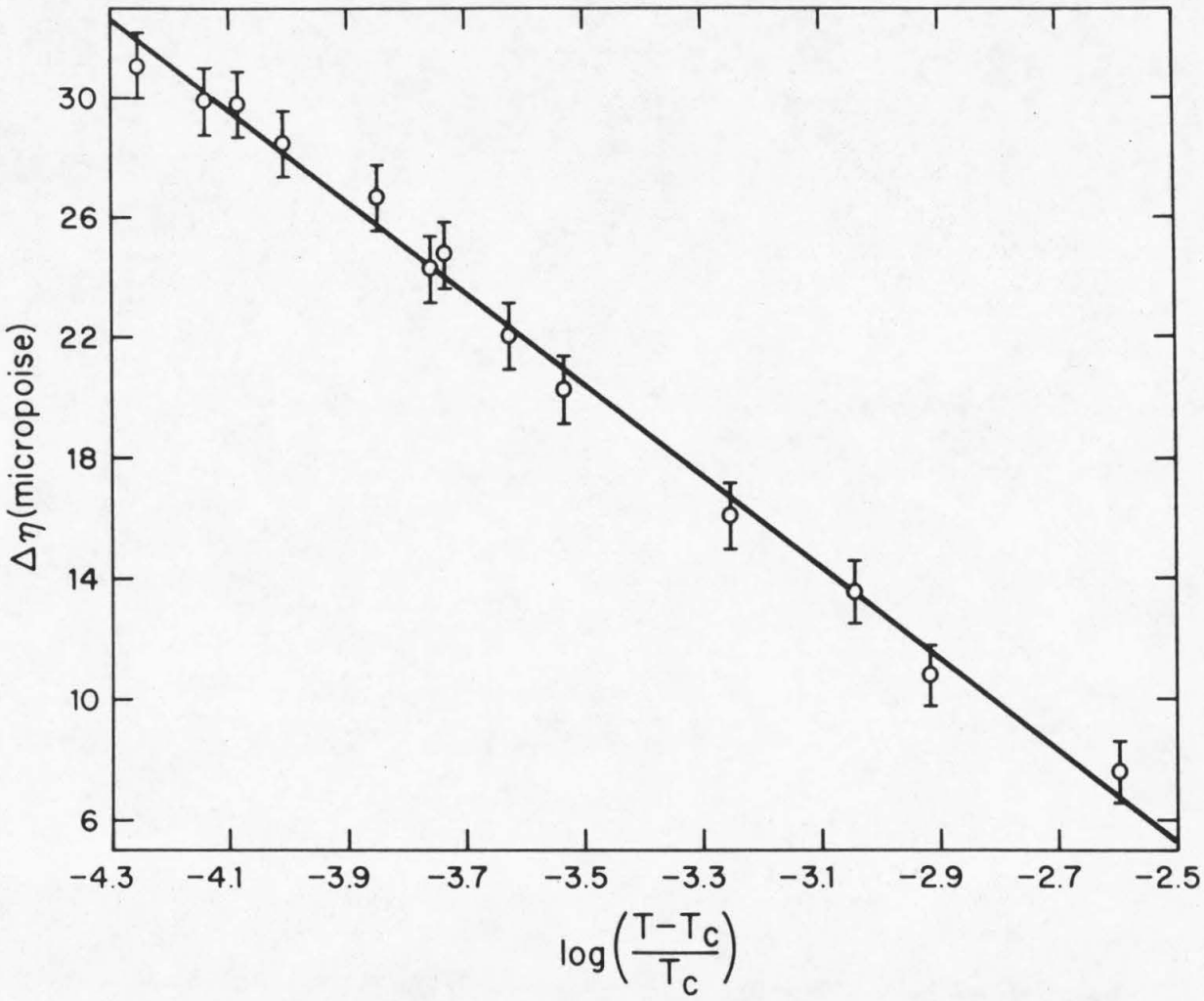

Figure 39. Anomalous viscosity vs. logarithm of reduced temperature difference for ethane isochore at $\rho = 0.20952$

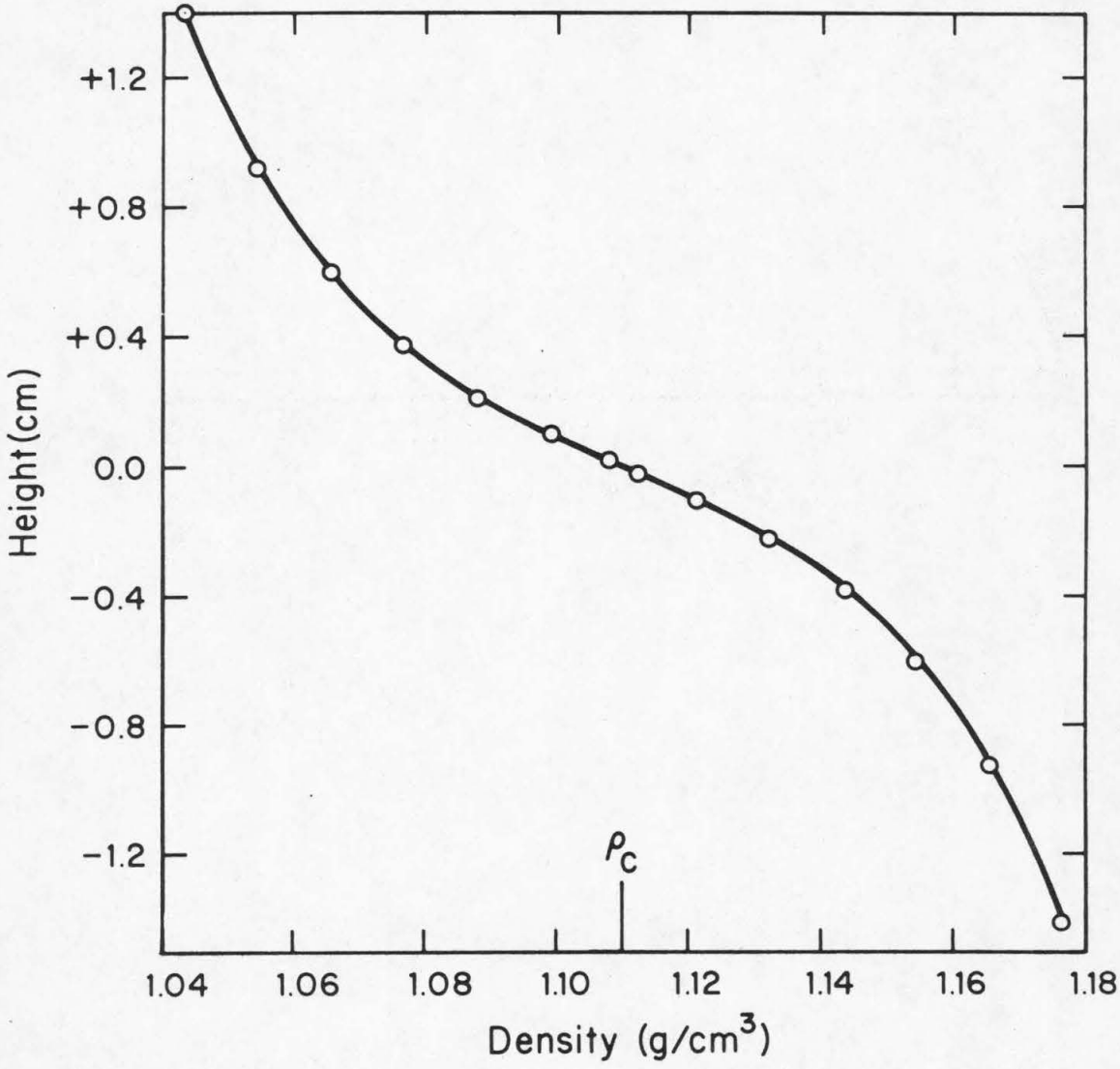

Figure 40. Density profile for xenon at $T - T_c = 0.034^{\circ}C$ ($\varepsilon = 1.17 \times 10^{-4}$)

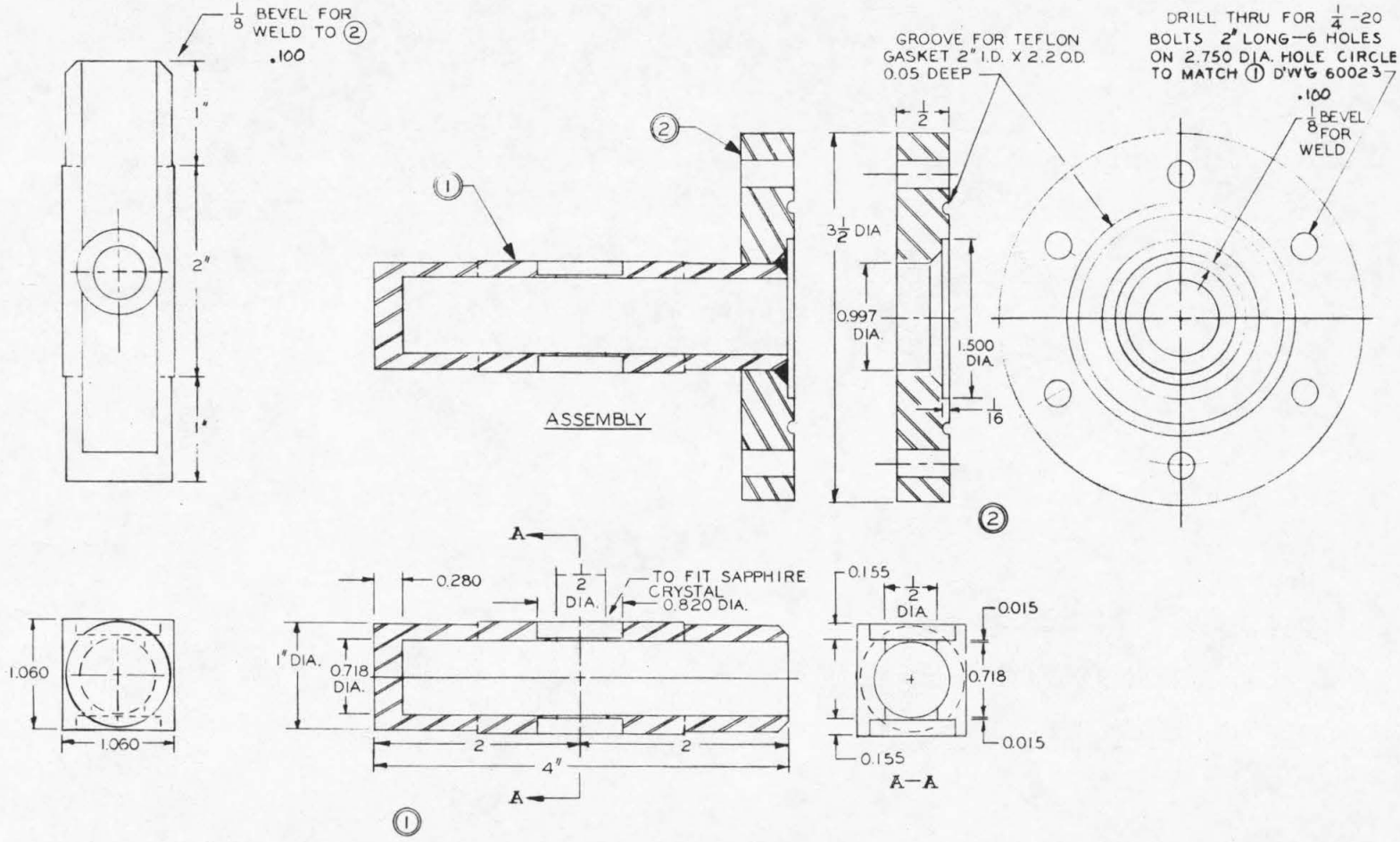

Figure 41. Drawing of cell with sapphire windows

Figure 42. Photograph of cell with sapphire windows

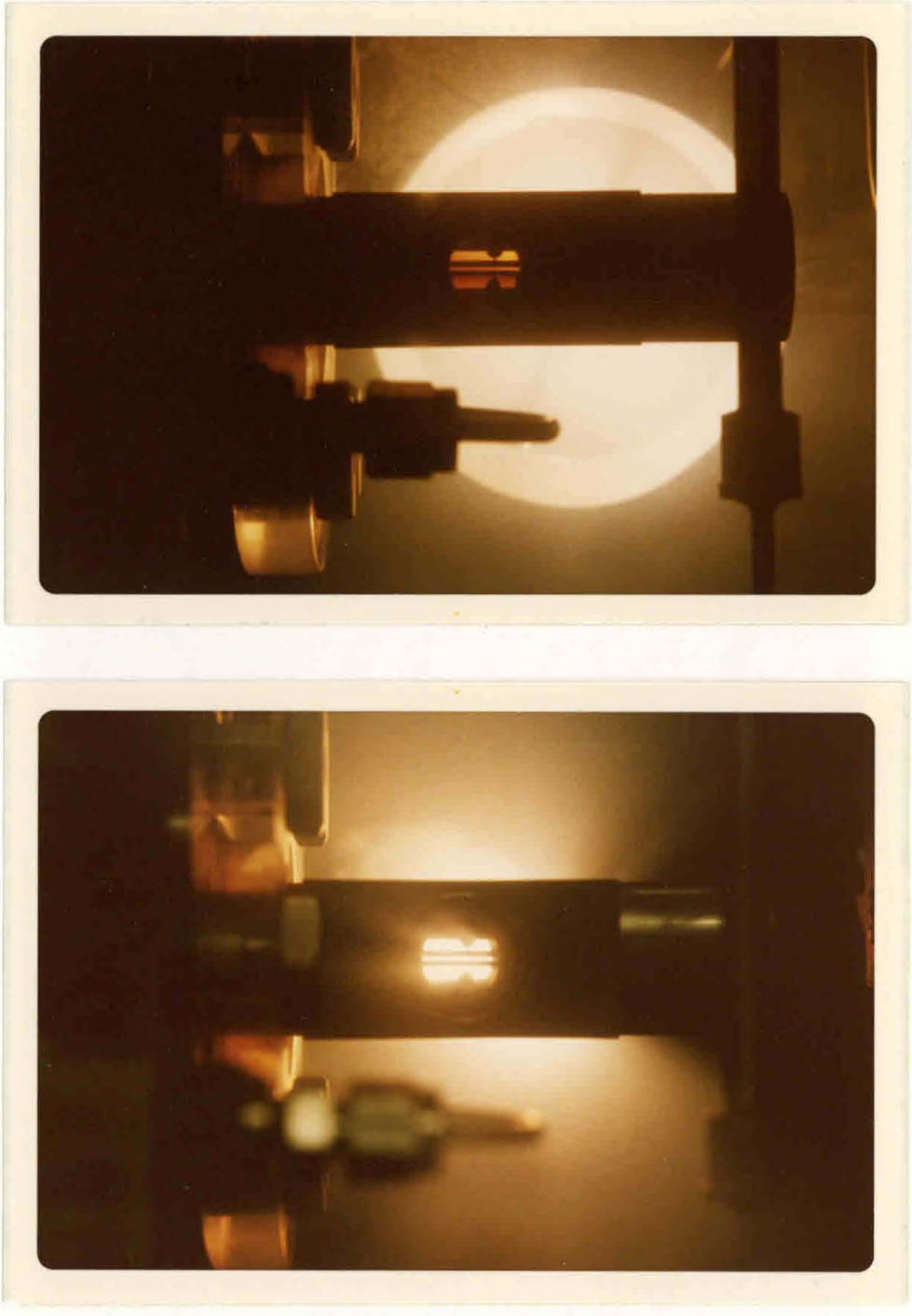

Figure 43. Critical opalescence of xenon

top: close to critical
bottom: far from critical

TABLE I

Calibration of pressure gauge #2

Pressure (psig)	Gauge Reading
0.00	0.000
50.00	10.310
100.00	20.604
150.00	30.907
200.00	41.193
250.00	51.442
300.00	61.706
350.00	71.960
400.00	82.198
450.00	92.416
500.00	102.630
550.00	112.822
600.00	123.005
650.00	133.173
700.00	143.335
750.00	153.465
800.00	163.578
850.00	173.703
900.00	183.850
950.00	193.934
1000.00	204.009

TABLE II

Resistance of Leeds and Northrup standard resistor

Temperature (°C)	Resistance (ohms)	Temperature (°C)	Resistance (ohms)
18.00	99.99374	20.10	99.99608
18.05	99.99381	20.15	99.99613
18.10	99.99387	20.20	99.99618
18.15	99.99393	20.25	99.99623
18.20	99.99399	20.30	99.99627
18.25	99.99405	20.35	99.99632
18.30	99.99411	20.40	99.99637
18.35	99.99417	20.45	99.99642
18.40	99.99423	20.50	99.99647
18.45	99.99429	20.55	99.99652
18.50	99.99435	20.60	99.99656
18.55	99.99441	20.65	99.99661
18.60	99.99447	20.70	99.99665
18.65	99.99453	20.75	99.99670
18.70	99.99458	20.80	99.99674
18.75	99.99464	20.85	99.99679
18.80	99.99470	20.90	99.99683
18.85	99.99476	20.95	99.99688
18.90	99.99482	21.00	99.99692
18.95	99.99487	21.05	99.99697
19.00	99.99492	21.10	99.99701
19.05	99.99498	21.15	99.99705
19.10	99.99503	21.20	99.99709
19.15	99.99509	21.25	99.99713
19.20	99.99514	21.30	99.99718
19.25	99.99520	21.35	99.99723
19.30	99.99525	21.40	99.99727
19.35	99.99531	21.45	99.99731
19.40	99.99537	21.50	99.99735
19.45	99.99542	21.55	99.99739
19.50	99.99547	21.60	99.99743
19.55	99.99553	21.65	99.99747
19.60	99.99558	21.70	99.99751
19.65	99.99563	21.75	99.99755
19.70	99.99568	21.80	99.99759
19.75	99.99573	21.85	99.99763
19.80	99.99578	21.90	99.99767
19.85	99.99583	21.95	99.99771
19.90	99.99588	22.00	99.99774
19.95	99.99593	22.05	99.99777
20.00	99.99598	22.10	99.99780
20.05	99.99603		

TABLE III

Calibration table for thermometer

Temperature ^{o}C	R/R_o	Difference
10	1.039076	0.003903
11	1.042978	0.003901
12	1.046878	0.003900
13	1.050778	0.003899
14	1.054676	0.003898
15	1.058573	0.003897
16	1.062468	0.003896
17	1.066363	0.003895
18	1.070257	0.003894
19	1.074149	0.003892
20	1.078041	0.003892
21	1.081931	0.003890
22	1.085820	0.003889
23	1.089708	0.003888
24	1.093595	0.003887
25	1.097481	0.003886
26	1.101365	0.003885
27	1.105249	0.003884
28	1.109131	0.003882
29	1.113012	0.003881
30	1.116893	0.003880
31	1.120772	0.003879
32	1.124650	0.003878
33	1.128526	0.003877
34	1.132402	0.003876
35	1.136276	0.003875
36	1.140150	0.003873
37	1.144022	0.003872
38	1.147893	0.003871
39	1.151763	0.003870
40	1.155632	0.003869
41	1.159500	0.003868
42	1.163367	0.003867
43	1.167232	0.003866
44	1.171097	0.003864
45	1.174960	0.003863
46	1.178822	0.003862
47	1.182683	0.003861
48	1.186543	0.003860
49	1.190402	0.003859
50	1.194260	0.003858
51	1.198116	0.003857

TABLE IV

Calibration of class S-2 masses

Nominal Mass (g)	Actual Mass (g)
50	49.9999
20	19.9999
10	9.9999
10*	9.9999
5	4.9998
2	1.9999
2*	1.9999
1	0.9998
0.5	0.4996
0.2	0.1998
0.1	0.0998
0.1*	0.0998
0.05	0.0498
0.02	0.0199

TABLE V

Volume of weighing bomb

Temperature (°C)	Pressure (psia)	Specific Volume of Water[37] (cm^3/g)	Volume of Weighing Bomb (cm^3)
30	14.7	1.004370	11.1962
30	1300	1.000445	11.2032
30	791	1.001978	11.2009
10	14.7	1.000301	11.1877

TABLE VI

Viscosity of n-hexane at 1 atm

Temperature °C	Measured Viscosity × 10^4 poise	API[43] Viscosity × 10^4 poise	% Difference
17.0	32.77	32.15	+ 1.9
20.5	31.50	31.12	+ 1.2
25.0	30.05	29.85	+ 0.7
30.3	28.54	28.47	+ 0.2
34.9	27.30	27.34	- 0.1
40.0	26.05	26.19	- 0.5
45.0	24.90	25.12	- 0.9
50.0	23.76	24.11	- 1.5

Viscosity of cyclohexane at 1 atm

15.4	108.90	106.56	+ 2.2
20.5	98.97	97.18	+ 1.8
25.0	91.39	89.80	+ 1.8
30.0	84.25	82.60	+ 2.0
35.0	77.46	76.10	+ 1.8
40.0	71.86	70.40	+ 2.1
44.8	66.80	65.50	+ 2.0
49.8	62.29	60.79	+ 2.5

TABLE VII

Viscosity of propane at 100°F (37.778°C)

Pressure (psia)	Measured Viscosity (micropoise)	Carmichael[45] Viscosity (micropoise)	% Difference
460	880.6	885.5	- 0.6
590	912.0	903.5	+ 0.9
632	916.0	909.3	+ 0.7
819	949.1	934.5	+ 1.6
1045	971.8	961.6	+ 1.0

TABLE VIII

Viscosity of carbon dioxide

Density g/cm^3	Temperature ^oC	Resonant Frequency Hz	Resonant Resistance ohms	Bandwidth Hz	Viscosity micropoise
0.4123	34.522	38782.134	37,970	6.759	288.4
0.4123	32.567	38781.873	37,880	6.747	287.8
0.4123	31.638	38781.688	37,950	6.762	289.4
0.4123	31.261	38781.594	38,020	6.783	291.3
0.4123	31.086	38781.540	37,970	6.766	289.8
0.4313	34.249	38781.912	39,790	7.081	304.6
0.4313	32.229	38781.610	39,680	7.070	304.2
0.4313	31.660	38781.480	39,880	7.106	307.6
0.4313	31.390	38781.395	40,020	7.134	310.2
0.4313	31.132	38781.256	40,480	7.216	318.0
0.4313	31.390	38781.420	39,950	7.122	309.1
0.4313	32.234	38781.625	39,600	7.055	302.8
0.4313	34.207	38781.913	39,720	7.075	304.1
0.4992	34.497	38781.232	46,140	8.213	361.0
0.4992	32.481	38780.952	46,060	8.205	360.8
0.4992	31.576	38780.775	46,420	8.273	367.4
0.4992	31.334	38780.704	46,570	8.299	370.0
0.4992	31.120	38780.635	47,210	8.416	381.1
0.4992	31.097	38780.628	47,220	8.420	381.4
0.4992	31.040	38780.588	47,430	8.458	385.2

TABLE IX

Viscosity of xenon

Density g/cm^3	Temperature ^oC	Resonant Frequency Hz	Resonant Resistance ohms	Bandwidth Hz	Viscosity micropoise
Isochore I					
0.9570	24.993	38776.762	71,400	12,764	476.9*
0.9572	19.990	38776.000	70,270	12.594	464.7
0.9573	17.994	38775.538	70,160	12.586	464.5
0.9573	16.996	38775.298	70,300	12.613	466.8
0.9574	16.693	38775.145	70,640	12.681	472.0
0.9574	16.591	38775.035	70,550	12.661	470.5
0.9574	16.434	38774.755	70,850	12.713	474.6
0.9568	29.991	38777.515	70,840	12.626	465.4
0.9569	27.480	38777.126	70,700	12.616	465.1
0.9570	24.992	38776.752	71,220	12.731	474.3*
0.9574	16.434	38774.805	70,660	12.684	472.3
0.9568	29.991	38777.514	70,790	12.622	465.0
Isochore II					
1.4997	24.997	38772.073	113,000	20.198	782.6
1.5000	19.989	38771.258	113,300	20.287	790.6
1.5002	17.996	38771.016	112,350	20.144	779.6
1.5002	16.993	38770.807	112,140	20.117	777.7
1.5003	15.993	38770.616	112,040	20.107	777.0
1.5003	15.506	38770.512	112,000	20.105	777.0
1.5004	15.198	38770.438	112,600	20.225	786.5
1.5004	15.143	38770.478	112,450	20.189	783.7
1.5004	15.048	38770.438	112,130	20.127	778.8
1.5004	14.945	38770.393	112,440	20.182	783.2
1.5004	14.801	38770.437	112,500	20.202	784.8
1.5004	14.598	38770.387	112,140	20.134	779.5
1.5004	14.298	38770.312	111,940	20.103	777.1
1.4993	29.993	38772.839	113,400	20.214	783.0
1.5000	19.993	38771.237	112,970	20.220	785.3
1.5002	17.993	38771.008	112,230	20.114	777.3
1.5004	14.488	38770.360	111,950	20.106	777.2
1.5004	14.294	38770.305	111,960	20.111	777.7
1.5004	14.195	38770.287	111,910	20.101	776.9

Note: Viscosities with asterisks are the spurious peak values (see Section IV).

TABLE IX continued

Density g/cm^3	Temperature ^oC	Resonant Frequency Hz	Resonant Resistance ohms	Bandwidth Hz	Viscosity micropoise
Isochore III					
1.0796	30.001	38776.508	79,630	14.200	526.0
1.0798	24.996	38775.768	79,190	14.153	523.4
1.0801	20.002	38774.965	78,800	14.123	522.0
1.0802	17.996	38774.536	79,200	14.207	528.8
1.0802	16.996	38774.160	80,250	14.404	544.2
1.0802	16.900	38774.105	80,570	14.459	548.5
1.0802	16.800	38774.013	80,900	14.524	553.7
1.0802	16.702	38773.875	81,760	14.675	565.6
1.0798	24.992	38775.770	79,100	14.140	522.4
1.0802	17.993	38774.538	79,150	14.198	528.1
1.0802	16.994	38774.158	80,220	14.396	543.6
1.0802	16.894	38774.098	80,560	14.463	548.8
1.0802	16.794	38774.015	80,850	14.508	552.4
1.0802	16.694	38773.876	81,680	14.662	564.6
1.0802	16.650	38773.797	81,590	14,647	563.4
1.0798	24.992	38775.778	79,050	14.128	521.5
1.0802	16.699	38773.893	81,500	14.632	562.2
1.0802	16.689	38773.870	81,640	14.658	564.2
1.0802	16.681	38773.855	81,670	14.663	564.6
1.0802	16.672	38773.836	81,740	14.671	565.3
1.0802	16.658	38773.802	81,810	14.685	566.4
Isochore IV					
1.0345	19.994	38775.314	75,460	13.520	498.0
1.0346	17.997	38774.888	75,840	13.600	504.5
1.0347	16.992	38774.521	76,440	13.717	513.7
1.0347	16.894	38774 461	76,800	13.784	518.9
1.0347	16.795	38774.375	77,150	13.849	524.0
1.0347	16.700	38774.255	77,470	13.906	528.4
1.0347	16.647	38774.121	77,910	13.985	534.7
1.0341	29.999	38776.867	76,230	13.591	501.6
1.0343	25.002	38776.094	76,270	13.634	505.8*
1.0347	16.786	38774.371	77,050	13.837	523.0
1.0347	16.693	38774.255	77,350	13.885	526.8
1.0347	16.644	38774.128	77,740	13.957	532.4
1.0347	16.635	38774.095	77,840	13.975	533.9
1.0341	29.992	38776.871	76,200	13.591	501.6

TABLE IX continued

Density g/cm^3	Temperature ^oC	Resonant Frequency Hz	Resonant Resistance ohms	Bandwidth Hz	Viscosity micropoise
Isochore V					
1.1088	24.992	38775.532	81,560	14.575	541.6*
1.1090	20.003	38774.793	80,760	14.472	534.6
1.1091	17.992	38774.350	81,270	14.582	543.4
1.1092	17.004	38773.985	82,630	14.833	563.0
1.1092	16.898	38773.923	83,000	14.894	567.8
1.1092	16.798	38773.817	83,680	15.021	577.9
1.1092	16.701	38773.679	84,800	15.224	594.1
1.1092	16.684	38773.646	85,130	15.275	598.2
1.1092	16.677	38773.636	85,250	15.301	600.3
1.1092	16.663	38773.607	85,470	15.347	604.0
1.1086	29.990	38776.327	81,380	14.507	535.4
1.1087	27.976	38776.030	81,250	14.500	535.2
1.1088	24.993	38775.506	81,500	14.555	540.1*
1.1089	21.992	38775.127	80,760	14.456	533.1
1.1090	19.988	38774.769	80,660	14.450	532.9
1.1092	16.696	38773.669	84,720	15.207	592.7
1.1092	16.673	38773.621	85,180	15.292	599.5
1.1092	16.661	38773.592	85,450	15.337	603.2
1.1086	29.991	38776.329	81,350	14.502	535.1
Isochore VI					
1.1704	24.992	38775.082	85,830	15.341	570.2
1.1705	21.995	38774.647	85,940	15.390	574.5
1.1707	19.994	38774.250	86,060	15.428	577.8
1.1708	17.996	38773.882	85,970	15.427	578.1
1.1708	16.991	38773.558	87,160	15.644	595.1
1.1708	16.892	38773.507	87,540	15.712	600.5
1.1708	16.796	38773.442	87,960	15.787	606.4
1.1708	16.694	38773.341	88,860	15.952	619.5
1.1708	16.675	38773.313	89,080	15.992	622.7
1.1708	16.665	38773.295	89,270	16.025	625.4
1.1708	16.660	38773.287	89,350	16.042	626.7
1.1708	16.648	38773.262	89,590	16.087	630.4
1.1708	16.639	38773.252	89,760	16.116	632.7
1.1708	16.636	38773.238	89,890	16.145	635.0
1.1701	29.994	38775.794	86,500	15.424	575.7
1.1704	24.993	38775.063	85,650	15.312	568.0
1.1705	21.992	38774.630	85,810	15.365	572.6
1.1707	19.993	38774.245	86,030	15.428	577.7
1.1701	29.991	38775.794	86,520	15.430	576.2

TABLE IX continued

Density g/cm^3	Temperature ^oC	Resonant Frequency Hz	Resonant Resistance ohms	Bandwidth Hz	Viscosity micropoise
Isochore VII					
1.1033	21.991	38775.178	80,620	14.435	534.2
1.1034	19.991	38774.820	80,520	14.424	533.7
1.1035	17.995	38774.383	81,080	14.547	543.5
1.1036	16.999	38774.016	82,450	14.798	563.1
1.1036	16.896	38773.953	82.780	14.862	568.1
1.1036	16.794	38773.843	83,490	14.992	578.5
1.1036	16.696	38773.696	84,720	15.207	595.7
1.1036	16.686	38773.675	84,920	15.239	598.3
1.1036	16.683	38773.662	85,000	15.255	599.6
1.1036	16.673	38773.647	85,100	15.278	601.4
1.1036	16.661	38773.618	85,350	15.320	604.8
1.1036	16.658	38773.620	85,280	15.307	603.8
1.1036	16.652	38773.598	85,420	15.337	606.2
1.1030	29.991	38776.365	81,160	14.469	535.3
1.1031	27.987	38776.068	81,020	14.461	535.0
1.1032	24.996	38775.549	82,060	14.708	554.5*
1.1032	23.990	38775.495	81,830	14.646	550.0*
1.1033	22.992	38775.327	80,850	14.465	536.3*
1.1033	21.994	38775.167	80,540	14.422	533.2
1.1036	16.700	38773.703	84,460	15.159	591.8
1.1036	16.685	38773.675	84,770	15.221	596.8
1.1036	16.665	38773.630	85,120	15.280	601.6
1.1036	16.658	38773.621	85,060	15.267	600.6
1.1036	16.655	38773.612	85,110	15.277	601.4
1.1030	29.992	38776.365	81,120	14.464	534.9
Isochore VIII					
1.1348	21.993	38774.935	83,000	14.862	551.5
1.1350	19.988	38774.575	83,200	14.914	555.8
1.1351	17.994	38774.139	83,310	14.942	558.3
1.1351	16.994	38773.782	84,860	15.237	581.4
1.1351	16.893	38773.725	85,200	15.293	585.9
1.1351	16.795	38773.628	85,880	15.418	595.8
1.1351	16.701	38773.510	86,970	15.612	611.3
1.1351	16.684	38773.476	87,370	15.680	616.8
1.1351	16.682	38773.470	87,450	15.698	618.3
1.1351	16.663	38773.433	87,980	15.796	626.2
1.1351	16.652	38773.409	88,320	15.854	631.0
1.1344	29.996	38776.118	83,600	14.910	553.7
1.1345	27.991	38775.805	83,360	14.880	551.7
1.1347	24.992	38775.332	83,190	14.875	551.9
1.1350	19.996	38774.557	83,090	14.894	554.2
1.1351	17.998	38774.127	83,200	14.927	557.2
1.1344	29.988	38776.117	83,580	14.905	553.3

TABLE IX continued

Density g/cm^3	Temperature ^oC	Resonant Frequency Hz	Resonant Resistance ohms	Bandwidth Hz	Viscosity micropoise
Isochore IX					
1.2276	24.993	38774.585	90,280	16.137	603.3
1.2277	21.993	38774.061	90,470	16.198	608.6
1.2278	19.992	38773.805	89,840	16.103	601.6
1.2280	17.996	38773.374	90,150	16.171	607.2
1.2280	16.994	38773.154	90,700	16.280	615.8
1.2280	16.897	38773.112	91.280	16.386	624.1
1.2280	16.799	38773.067	91,000	16.350	621.3
1.2280	16.701	38773.033	91,360	16.417	626.6
1.2280	16.594	38772.948	92,100	16.544	636.6
1.2280	16.544	38772.910	92,510	16.624	642.9
1.2280	16.516	38772.876	92,810	16.674	646.9
1.2280	16.494	38772.815	93,220	16.753	653.2
1.2280	16.472	38772.778	93,580	16.817	658.4
1.2280	16.450	38772.728	93,900	16.874	663.0
1.2273	29.986	38775.320	90,460	16.140	602.6
1.2277	21.997	38774.058	90,290	16.182	607.3
1.2280	16.998	38773.148	90,490	16.254	613.8
1.2280	16.896	38773.120	91,020	16.353	621.5
1.2280	16.794	38773.063	90,980	16.344	620.9
1.2280	16.693	38773.026	91,330	16.406	625.7
Isochore X					
1.1248	24.994	38775.415	82,760	14.797	550.8
1.1249	21.988	38774.986	82,260	14.723	545.7
1.1250	19.990	38774.642	82,300	14.746	547.8
1.1251	17.990	38774.195	82,690	14.837	555.2
1.1252	16.992	38773.840	84,160	15.107	576.3
1.1252	16.893	38773.785	84,500	15.168	581.1
1.1252	16.796	38773.688	85,170	15.290	590.8
1.1252	16.694	38773.549	86,480	15.518	609.1
1.1252	16.687	38773.533	86,660	15.557	612.3
1.1252	16.677	38773.517	86,910	15.600	615.8
1.1252	16.667	38773.489	84,845	15.655	620.2
1.1252	16.664	38773.489	87,280	15.675	621.8
1.1252	16.661	38773.474	87,390	15.690	623.1
1.1252	16.659	38773.468	87,500	15.709	624.6
1.1252	16.655	38773.460	87,590	15.723	625.8
1.1252	16.657	38773.464	87,550	15.718	625.4
1.1252	16.655	38773.459	87,640	15.734	626.7
1.1252	16.654	38773.458	87,660	15.736	626.8
1.1252	16.653	38773.455	87,720	15.748	627.8
1.1252	16.652	38773.449	87,740	15.752	628.1
1.1246	29.992	38776.187	82,900	14.780	548.5
1.1248	24.991	38775.407	82,650	14.778	549.3
1.1249	21.995	38774.982	82,190	14.711	544.8
1.1246	29.990	38776.186	82,900	14.780	548.5

TABLE X

Viscosity of ethane

Density g/cm^3	Temperature ^oC	Resonant Frequency Hz	Resonant Resistance ohms	Bandwidth Hz	Viscosity micropoise
Isochore I					
0.20004	43.332	38784.732	22,950	4.058	189.0
0.20009	37.768	38784.050	22,750	4.035	188.8
0.20011	34.991	38783.677	22,650	4.025	188.8
0.20012	33.990	38783.527	22,680	4,033	190.1
0.20013	32.989	38783.386	22,750	4.048	192.0
0.20013	32.591	38783.300	22,870	4.070	194.6
0.20013	32.490	38783.271	22,960	4.086	196.3
0.20013	32.388	38783.243	23,110	4.113	199.4
0.20013	32.292	38783.195	23,310	4.146	203.0
0.20014	32.245	38783.153	23,550	4.194	208.4
0.19999	48.882	38785.360	23,140	4.082	189.3
0.20002	45.989	38785.040	23,030	4.068	189.0
0.20004	43.322	38784.733	22,940	4.057	188.9
0.20006	40.493	38784.401	22,840	4.047	188.9
0.20013	32.295	38783.200	23,270	4.141	202.5
0.20014	32.261	38783.173	23,430	4.170	205.8
0.20014	32.242	38783.154	23,540	4.191	208.1
0.20014	32.232	38783.137	23,630	4.206	209.8
Isochore II					
0.20942	43.322	38784.648	23,960	4.238	199.3
0.20945	40.488	38784.312	23,860	4.228	199.3
0.20947	37.989	38783.994	23,770	4.217	199.2
0.20949	34.992	38783.593	23,700	4.212	199.9
0.20950	33.988	38783.442	23,700	4.214	200.5
0.20951	32.991	38783.300	23,800	4.235	203.1
0.20952	32.587	38783.215	23,950	4.261	206.2
0.20952	32.493	38783.190	24,080	4.287	209.0
0.20952	32.389	38783.162	24,210	4.308	211.4
0.20952	32.274	38783.107	24,640	4.386	220.1
0.20952	32.261	38783.100	24,730	4.402	222.0
0.20952	32.243	38783.090	24,890	4.430	225.1
0.20952	32.235	38783.083	24,960	4.441	226.4
0.20937	48.989	38785.293	24,190	4.268	200.2
0.20939	45.994	38784.958	24,030	4.245	199.0
0.20942	43.321	38784.648	23,940	4.235	199.0
0.20952	32.307	38783.124	24,420	4.346	215.6
0.20952	32.290	38783.117	24,510	4.362	217.4
0.20952	32.271	38783.107	24,620	4.381	219.6
0.20952	32.248	38783.092	24,820	4.418	223.8
0.20952	32.240	38783.088	24,880	4.431	225.2

Note: Viscosities with asterisks are the spurious peak values (see Section IV).

TABLE X continued

Density g/cm^3	Temperature °C	Resonant Frequency Hz	Resonant Resistance ohms	Bandwidth Hz	Viscosity micropoise
Isochore III					
0.28988	37.769	38783.000	33,610	5.966	310.9
0.28992	34.992	38782.632	33,370	5.935	308.6
0.28994	32.994	38782.352	33,320	5.932	309.1
0.28988	32.221	38782.245	33,320	5.934	309.7
0.28997	30.991	38782.070	33.230	5.920	308.6
0.28998	30.482	38781.992	33,180	5.915	308.4
0.28999	29.973	38781.915	33,190	5.917	308.9
0.28999	29.592	38781.872	33,170	5.914	308.6
0.28999	29.492	38781.850	33.160	5.915	308.8
0.28999	29.394	38781.834	33,210	5.924	309.8
0.29000	29.294	38781.812	33,230	5.927	310.2
0.29000	29.098	38781.812	33,360	5.951	313.0
0.29000	28.702	38781.744	33,130	5.911	308.6
0.28973	48.996	38784.353	33,950	5.996	309.6
0.28977	45.992	38784.018	33,730	5.966	307.4
0.28980	43.322	38783.698	33,680	5.964	308.3
0.28984	40.495	38783.355	33,530	5.950	307.9
0.28988	37.775	38783.001	33,540	5.958	310.0
0.28999	30.001	38781.916	33,150	5.911	308.2
0.28999	29.895	38781.888	33,210	5.923	309.2
0.28999	29.750	38781.900	33,230	5.924	309.8
0.29000	28.796	38781.756	33,120	5.912	308.6
0.29000	28.697	38781.740	33,100	5.907	308.1
Isochore IV					
0.21628	43.321	38784.576	24,660	4.365	206.3
0.21631	40.492	38784.226	24,760	4.391	210.2*
0.21633	37.996	38783.923	24,490	4.347	206.6
0.21636	34.994	38783.521	24,410	4.340	207.0
0.21637	34.002	38783.373	24,430	4.346	208.1
0.21638	32.991	38783.234	24,490	4.361	210.1
0.21638	32.597	38783.152	24,610	4.382	212.5
0.21638	32.489	38783.126	24,710	4.400	214.5
0.21638	32.401	38783.108	24,850	4.425	217.3
0.21638	32.293	38783.072	25,010	4.458	220.9
0.21638	32.271	38783.063	25,090	4.467	222.1
0.21638	32.255	38783.054	25,190	4.485	224.1
0.21638	32.243	38783.048	25,280	4.499	225.7
0.21638	32.237	38783.048	25,310	4.504	226.2
0.21638	32.229	38783.044	25,380	4.517	227.7
0.21638	32.219	38783.040	25,470	4.535	229.7
0.21623	48.993	38785.235	25,020	4.412	209.1
0.21625	45.988	38784.888	24,760	4.375	206.4
0.21628	43.329	38784.582	24,650	4,360	205.8
0.21629	42.002	38784.422	24,620	4.360	206.3
0.21630	41.007	38784.298	24,620	4.360	206.8

TABLE X continued

Density g/cm^3	Temperature ^oC	Resonant Frequency Hz	Resonant Resistance ohms	Bandwidth Hz	Viscosity micropoise
Isochore IV (continued)					
0.21631	40.492	38784.233	24,770	4.390	210.1*
0.21631	39.999	38784.188	24,600	4.359	207.1
0.21638	32.493	38783.132	24,700	4.396	214.1
Isochore V					
0.21129	43.324	38784.636	24,150	4.271	201.0
0.21132	40.490	38784.300	24.070	4.269	201.9
0.21134	37.991	38783.980	23,960	4.253	201.2
0.21137	34.996	38783.581	23,880	4.246	201.7
0.21138	33.993	38783.430	23,880	4.247	202.3
0.21138	32.994	38783.289	23,980	4.267	204.8
0.21139	32.596	38783.205	24,130	4.296	208.1
0.21139	32.495	38783.176	24,270	4.321	210.8
0.21139	32.392	38783.153	24,400	4.344	213.4
0.21139	32.293	38783.110	24,670	4.391	218.7
0.21139	32.272	38783.100	24,790	4.413	221.2
0.21139	32.260	38783.093	24,870	4.429	223.0
0.21139	32.251	38783.088	24,940	4.442	224.5
0.21139	32.240	38783.081	25,040	4.458	226.3
0.21139	32.232	38783.077	25,120	4.472	227.9
0.21124	48.999	38785.280	24,400	4.305	202.4
0.21126	46.001	38784.945	24,230	4.281	201.1
0.21129	43.328	38784.635	24,150	4.272	201.1
0.21132	40.498	38784.302	24,070	4.267	201.7

TABLE XI

Anomalous viscosity of xenon for $\rho = 1.1092 g/cm^3$

T(°C)	$\frac{T-T_c}{T_c}$	$\log(\frac{T-T_c}{T_c})$	η micropoise	$\Delta\eta$ micropoise	$\log \Delta\eta$
20.003	1.165×10^{-2}	-1.934	534.6	7.0	0.845
17.992	4.711×10^{-3}	-2.327	543.4	17.2	1.236
17.004	1.301×10^{-3}	-2.886	563.0	37.6	1.575
16.898	9.352×10^{-4}	-3.029	567.8	42.5	1.628
16.798	5.901×10^{-4}	-3.229	577.9	52.7	1.722
16.701	2.554×10^{-4}	-3.593	594.1	68.9	1.838
16.684	1.967×10^{-4}	-3.706	598.2	73.0	1.863
16.677	1.725×10^{-4}	-3.763	600.3	75.1	1.876
16.663	1.242×10^{-4}	-3.906	604.0	78.8	1.897
19.988	1.160×10^{-2}	-1.936	532.9	5.3	0.724
16.696	2.381×10^{-4}	-3.623	592.7	67.5	1.829
16.673	1.587×10^{-4}	-3.799	599.5	74.3	1.871
16.661	1.173×10^{-4}	-3.931	603.2	78.0	1.892

TABLE XII

Anomalous viscosity of ethane for $\rho = 0.20952 g/cm^3$

$T(^{o}C)$	$\frac{T-T_c}{T_c}$	$\log(\frac{T-T_c}{T_c})$	η (micropoise)	$\Delta\eta$ (micropoise)	$\log \Delta\eta$
32.991	2.531×10^{-3}	-2.597	203.1	7.6	0.881
32.587	1.208×10^{-3}	-2.918	206.2	10.8	1.033
32.493	9.006×10^{-4}	-3.045	209.0	13.6	1.134
32.389	5.600×10^{-4}	-3.252	211.4	16.1	1.207
32.274	1.834×10^{-4}	-3.737	220.1	24.8	1.394
32.261	1.408×10^{-4}	-3.851	222.0	26.7	1.427
32.243	8.187×10^{-5}	-4.087	225.1	29.8	1.474
32.235	5.567×10^{-5}	-4.254	226.4	31.1	1.493
32.307	2.915×10^{-4}	-3.535	215.6	20.3	1.307
32.290	2.358×10^{-4}	-3.627	217.4	22.1	1.344
32.271	1.736×10^{-4}	-3.761	219.6	24.3	1.386
32.248	9.824×10^{-5}	-4.008	223.8	28.5	1.455
32.240	7.204×10^{-5}	-4.142	225.2	29.9	1.476

TABLE XIII

Viscosity of xenon with sapphire window cell

Density (g/cm^3)	Temperature (^oC)	Resonant Frequency (Hz)	Resonant Resistance (ohms)	Bandwidth (Hz)	Viscosity (micropoise)
1.0990	29.993	38776.445	81,150	14.470	537.3
1.0991	27.996	38776.149	80,960	14.450	536.1
1.0992	24.995	38775.645	81.120	14.500	540.5
1.0992	24.008	38775.568	81,820	14.642	551.6
1.0993	23.019	38775.349	81,150	14.517	542.2
1.0993	21.993	38775.250	80,450	14.403	533.7
1.0996	16.798	38773.906	83.170	14.935	576.7

TABLE XIV

Viscosity of ethane with sapphire window cell

Density (g/cm^3)	Temperature (^oC)	Resonant Frequency (Hz)	Resonant Resistance (ohms)	Bandwidth (Hz)	Viscosity (micropoise)
0.21568	43.324	38784.640	24,700	4.372	207.6
0.21570	41.002	38784.359	24,610	4.361	207.4
0.21571	40.492	38784.305	24,670	4.372	208.8
0.21571	40.641	38784.325	24,610	4.361	207.6
0.21571	40.346	38784.298	24,620	4.362	207.8

REFERENCES

1. P. Heller, Rep. Prog. Phys. 30, 731 (1967).

2. J. V. Sengers in Critical Phenomena, eds. M. S. Green and J. V. Sengers, National Bureau of Standards Misc. Publ. No. 273, Washington, D. C., 1966.

3. B. L. Smith, Contemp. Phys. 10, 305 (1969).

4. B. J. Widom, J. Chem. Phys. 46, 3324 (1967).

5. J. V. Sengers and A. Michels in Progress in International Research on Thermodynamic and Transport Properties (ASME, Princeton, N.J., 1962).

6. J. V. Sengers, to be published in Ber. Bunsenges Physik. Chem.

7. H. M. Leister, J. C. Allegra, and G. F. Allen, J. Chem. Phys. 51, 3701 (1969).

8. M. E. Fisher, Rep. Prog. Phys. 30, 615 (1967).

9. L. P. Kadanoff and J. Swift, Phys. Rev. 166, 89 (1968).

10. A. Michels, A. Botzen, and W. Schuurman, Physica 23, 95 (1957).

11. K. E. Starling, B. E. Eakin, J. P. Dolan, and R. T. Ellington, in Progress in International Research on Thermodynamic and Transport Properties (ASME, Princeton, N.J., 1962).

12. S. N. Naldrett and O. Maass, Can. J. Res. 18B, 322 (1940).

13. J. Kestin, J. H. Whitelaw and T. F. Zien, Physica 30, 161 (1964).

14. D. E. Diller, J. Chem. Phys. 42, 2089 (1965).

15. W. P. Mason, Trans. ASME 69, 359 (1947).

16. P. E. Rouse, E. D. Bailey and J. A. Minkin, API Symposium Anal. Res. (1950).

17. Proc. IRE 37, 1378 (1949).

18. R. N. Thurston and P. Andreatch, IRE Natl. Conv. Record 3, Part 9, 45 (1957).

19. W. G. Cady, Piezoelectricity (McGraw-Hill, New York City, 1946), p. 4.

20. A. F. Collings, Ph.D. Thesis, University of London, 1966.

21. W. P. Mason, Piezoelectric Crystals and Their Application to Ultrasonics (Van Nostrand, Princeton, N.J., 1950), p. 91.

22. R. W. Thurston in Physical Acoustics, ed. by W. P. Mason, Vol. 1A (Academic Press, New York City, 1964), p. 64.

23. R. B. Bird, W. E. Stewart, and E. N. Lightfoot, Transport Phenomena (John Wiley & Sons, New York City, 1960), p. 79.

24. W. P. Mason, Piezoelectric Crystals and Their Application to Ultrasonics (Van Nostrand, Princeton, N.J., 1950), p. 67 .

25. W. R. Smythe, Static and Dynamic Electricity (McGraw-Hill, New York City, 1950), p. 329.

26. L. F. Phillips, Electronics for Experimenters (John Wiley & Sons, New York City, 1966), p. 6.

27. D. Halliday and R. Resnick, Physics for Students of Science and Engineering, Part II, 2nd edition (John Wiley & Sons, New York City, 1962), p. 877.

28. Ibid., Part I, p. 292.

29. A. J. Barlow, G. Harrison, J. Richter, H. Seguin, and J. Lamb, Laboratory Practice 11, 786 (1961).

30. W. P. Mason and H. J. McSkimin, Bell Sys. Tech. J. 31, 122 (1952).

31. A. Smakula and V. Sils, Phys. Rev. 99, 1744 (1955).

32. R. A. Heising, Quartz Crystals for Electrical Circuits (Van Nostrand Co., New York, 1946) , p. 280.

33. Ibid., p. 451.

34. H. F. Stimson, J. Res. NBS 42, 209 (1949).

35. Comité International des Poids et Mesures, Metrologia 5, 35 (1969).

36. D. A. Skoog and D. M. West, Fundamentals of Analytical Chemistry, (Holt, Rinehart, and Winston, New York City, 1963), p. 95.

37. G. S. Kell and E. Whalley, Royal Soc. Lond. Phil. Trans. 258A, 565 (1965).

38. "Stainless Steel Handbook", Allegheny Ludlum Steel Corporation, 1951.

39. S. Timoshenko and D. H. Young, Elements of Strength of Materials, 4th edition (D. Van Nostrand Co., Inc., Princeton, N.J., 1962), p. 23.

40. A. Michels, B. Blaisse, and C. Michels, Proc. Roy. Soc. London A160, 358 (1937).

41. H. H. Reamer, R. H. Olds, B. H. Sage, and W. N. Lacey, Ind. and Eng. Chem. 36, 956 (1944).

42. A. Michels and C. Michels, Proc. Roy. Soc. London 153A, 201 (1935).

43. F. D. Rossini, ed., "Selected Values of Physical and Thermodynamic Properties of Hydrocarbons and Related Compounds", API Research Project 44, Carnegie Press, Pittsburgh, 1953.

44. H. H. Reamer, B. H. Sage, and W. N. Lacey, Ind. and Eng. Chem. 41, 482 (1949).

45. L. T. Carmichael, V. M. Berry, and B. H. Sage, J. Chem. and Eng. Data 9, 411 (1964).

46. F. Din, Thermodynamic Functions of Gases, Vol. 1, Butterworths Scientific Publications, 1956.

47. B. Welber, Phys. Rev. 119, 1816 (1960).

48. D. S. Betts, D. W. Osborne, B. Welber, and J. Wilks, Phil. Mag. 8, 977 (1963).

49. R. Sallavanti and M. Fixman, J. Chem. Phys. 48, 5326 (1968).

50. L. T. Carmichael and B. H. Sage, J. Chem. and Eng. Data 8, 94 (1963).

51. J. V. Sengers, Varenna Lectures on Critical Phenomena, ed. M. S. Green (Academic Press, New York City, in press).

52. A. G. Clarke and E. B. Smith, J. Chem. Phys. 48, 3988 (1968).

53. M. A. Weinberger and W. G. Schneider, Can. J. Chem. 30, 422 (1952).

54. V. M. Miniovich and G. A. Sorina, Russian J. Phys. Chem. 45, 306 (1971).

55. E.H.W. Schmidt in Critical Phenomena, eds. M. S. Green and J. V. Sengers, National Bureau of Standards Misc. Publ. No. 273, Washington, D. C. (1966).

56. M. Vicentini-Missoni and J.M.H. Levelt Sengers, Phys. Rev. Lett. 9, 389 (1969).

57. J.W.S. Rayleigh, Theory of Sound, Vol. II, 2nd Ed. (Macmillan and Company, London 1926), p. 317.

58. R. B. Bird, W. E. Stewart, and E. N. Lightfoot, Transport Phenomena (John Wiley & Sons, New York City, 1960), p. 315.

59. Ibid., p. 744.

Proposition I

It is proposed that the predictions made by information theory for the distribution of winners in horse racing are a good representation of the actual results. Information theory enables one to make a "best-guess" of a probability distribution on the basis of a limited amount of information. The guess made is the least biased estimate possible, and is maximally noncommittal with regard to the missing information.

- - - - - - -

Much of the groundwork for information theory was developed by Shannon[1] in 1948. The heart of the theory, known as Shannon's postulate, yields a quantity which is a measure of uncertainty. This quantity H is positive, increases with increasing uncertainty, is additive for independent sources of uncertainty, and is given by

$$H(p_i) = -K \sum_{i=1}^{n} p_i \ln p_i \qquad (1)$$

where p_i is the probability of event i

K is a positive constant.

In the transmission of information, a greater uncertainty implies a greater amount of information transferred. If the uncertainty is decreased, say by imposing restrictions on the system, the amount of information transferred is decreased, since the restrictions are already known. A good discussion of the basics of information theory can be found in Science and Information Theory by Leon

Brillouin[2]. The uncertainty in Eq. (1) is equivalent to the thermodynamic entropy[3].

The relationship between Shannon's postulate and statistical mechanics is discussed by Jaynes[4]. Jaynes shows that for a system in which the probabilities are unknown, the best assignment of probabilities is that which maximizes the entropy or uncertainty, subject to any restraints on the system. By "best assignment" is meant "least biased guess." The restraints are usually in the form of data for the system. This formulation is known as the maximum entropy postulate, and is the basis for the present work.

If nothing is known about the system, the maximum uncertainty assigns equal a priori probabilities to all states of the system. This results from the maximization of entropy or uncertainty in Eq. (1). The p_i's are all equal to $1/n$ and the entropy is equal to $\ln n$. However, if the expectation value of some function of the system is known, Eq. (1) can be maximized subject to this restraint, to yield probabilities which are better guesses than the equal probabilities. The maximization yields the best possible guess for the given information. The value of the entropy is decreased, since additional information has been given.

To clarify this, assume, with Jaynes[4], a given quantity x which takes on discrete values x_i $(i = 1,\cdots,n)$. The corresponding probabilities are not known. However, there is a function $f(x)$ whose expectation value, given by $\langle f(x) \rangle$, is known,

$$\langle f(x) \rangle = \sum_{i=1}^{n} p_i \, f(x_i) \qquad (2)$$

In addition, the sum of the probabilities equals one

$$\sum_{i=1}^{n} p_i = 1 \qquad (3)$$

Using Eqs. (2) and (3), Eq. (1) can be maximized by introducing Lagrangian multipliers, to yield the maximum entropy probability distribution for the system. With $f(x_i)$ defined as the energy of a state i, Jaynes derives the canonical partition function of the system, using only the value of the average energy $<f(x)>$ and no other information.

The present problem is concerned with the distribution of payoffs in horse racing. Under the pari-mutuel betting system (which is used at all American tracks) the payoffs for winning horses, and indeed, the odds for all horses, are determined by the percentage of money bet on a given horse out of the total money bet, after taxes and the track's profit are subtracted. Over the long run, the odds as determined by the bettors represent a fairly good appraisal of the abilities of the horses, as evidenced by the fact that year after year the percentage of horses that have been favorites in a race and have won, remains remarkably constant. This also holds true for second and third favorites[5]. Thus, it would seem that the payoffs for winning horses follow some pattern, at least in the long run, and this pattern might possibly be predicted by the maximum entropy postulate.

In defining the problem, analogies are made between the horse racing parameters and certain parameters in statistical mechanics, e.g., energy levels, molecular states, partition functions, etc. This

is done to aid in the solution of the problem and will become clear as the development is presented.

The quantities in Eqs. (1), (2), and (3) are defined as follows. The quantity x represents a winning of a race, and its states x_i $(i = 1, \cdots, n)$ represent the state of the system such that the winner of a given race is horse i. The probability of finding the system in state x_i is given by p_i. The interpretation of the meaning of the probabilities is important. Choose a horse k, which is known to have raced exactly once at Santa Anita racetrack during a racing season. Choose a race at random; the probability that the winner of this race is horse k is p_k. A horse is assigned a new index every time it races, so that the i's might more precisely be called starts rather than horses.

The function $f(x)$ is the profit function; $f(x_i)$ is defined as the profit of horse i on a one dollar bet. An equivalent definition of $f(x_i)$ is the odds on horse i, defined only if horse i wins; otherwise, $f(x_i)$ is zero. Since a horse usually doesn't win every race it enters, $f(x_i)$ will very often be equal to zero. The expectation value $\langle f(x) \rangle$, is equal to the average profit for winning horses.

With the definitions set, Eq. (1) can be maximized using Lagrangian multipliers. This is done by defining functions $F(p_i)$ and $G(p_i)$ as follows:

$$F(p_i) = \sum_{i=1}^{n} p_i \, f(x_i) - \langle f(x) \rangle = 0 \qquad (4)$$

$$G(p_i) = \sum_{i=1}^{n} p_i - 1 = 0 \tag{5}$$

Since there are two restraints, two Lagrangian multipliers are necessary; they are λ' and μ. Using these, a linear combination of $H(p_i)$, $F(p_i)$, and $G(p_i)$ is formed,

$$H(p_i) - \lambda' G(p_i) - \mu F(p_i) = L(p_i) \tag{6}$$

where $L(p_i)$ is now the function which is to be maximized.

The condition for maximization of $L(p_i)$ is,

$$\frac{\partial(H - \lambda' G - \mu F)}{\partial p_i} = 0 \tag{7}$$

The differentiation is performed for all $i = 1,\cdots,n$. Substituting Eqs. (1), (4), and (5) into (7) yields

$$\frac{\partial[-\sum_{i=1}^{n} p_i \ln p_i - \lambda'(\sum_{i=1}^{n} p_i - 1) - \mu(\sum_{i=1}^{n} p_i f(x_i) - \langle f(x)\rangle]}{\partial p_i} = 0$$

$$i = 1,\cdots,n \tag{8}$$

where K in Eq. (1) has been set equal to one. This only has the effect of changing the values of the multipliers.

The differentiation yields,

$$-\ln p_i - 1 - \lambda' - \mu f(x_i) = 0$$

$$p_i = \exp[-\lambda - \mu f(x_i)] \tag{9}$$

where $\lambda = \lambda' + 1$.

One of the multipliers can be eliminated by substituting Eq. (9) into Eq. (5) to give,

$$\sum_{i=1}^{n} e^{-\lambda - \mu f(x_i)} = 1$$

$$e^{\lambda} = \sum_{i=1}^{n} e^{-\mu f(x_i)} = Z \tag{10}$$

e^{λ} is defined as the system partition function Z which is a function only of μ [4]. Substituting Eq. (9) into Eq. (4) yields

$$\langle f(x) \rangle = e^{-\lambda} \sum_{i=1}^{n} e^{-\mu f(x_i)} f(x_i) \tag{11}$$

From Eq. (10) it can be seen that

$$\frac{\partial Z(\mu)}{\partial \mu} = \sum_{i=1}^{n} - f(x_i) e^{-\mu f(x_i)} \tag{12}$$

Combining Eqs. (11) and (12) gives

$$\langle f(x) \rangle = - \frac{1}{Z} \frac{\partial Z(\mu)}{\partial \mu}$$

$$\langle f(x) \rangle = - \frac{\partial \ln Z(\mu)}{\partial \mu} \tag{13}$$

The multiplier μ must be chosen so that Eq. (13) holds. The next step is to solve for μ using Eqs. (10) and (13). At this point the analogies to statistical mechanics come in handy. The $f(x_i$'s) can be considered analogous to energy levels and the i's analogous to molecular states. A density of states function w_i is defined. This is simply the degeneracy of a level $f(x_i)$; i.e., the

number of states in a given level. Thus, the summation in Eq. (10), which is over states, can be transformed to a summation over levels by[6]

$$Z(\mu) = \sum_{i=1}^{n} e^{-\mu f(x_i)} = \sum_{f(x_i)} w_i \, e^{-\mu f(x_i)} \tag{14}$$

The levels, which represent the profit for winning horses, can be approximately treated as a continuous variable, since the intervals are as small as \$1 out of, say, \$200,000 bet on a single race. Thus,

$$Z(\mu) \simeq \int_0^{\infty} w(y) \, e^{-\mu y} \, dy \tag{15}$$

where $y \equiv f(x)$.

From Eq. (9):

$$P_i = \frac{e^{-\mu f(x_i)}}{Z(\mu)} = \frac{e^{-\mu f(x_i)}}{\sum_{i=1}^{n} e^{-\mu f(x_i)}} \tag{16}$$

The probability given by Eq. (16) is the probability of the system being in state x_i . To transform to the probability of the system being in level $f(x_i)$ or $f(x) + df(x)$, since $f(x)$ is being treated as continuous, multiplication by the density of states function is necessary[6],

$$p_{f(x_i)} = wp_i$$

$$p_{f(x)} \equiv p_y = \frac{w(y) \, e^{-\mu y}}{\int_0^{\infty} w(y) e^{-\mu y} dy} = \frac{w(y) e^{-\mu y}}{Z(\mu)} \tag{17}$$

The meaning of the density of states function should be clear. It is the degeneracy of a given odds level, i.e., out of all horses, $w[f(x)]$ of these horses go off at odds $f(x) + df(x)$. It has nothing to do with winners, but is a function of all the horses. It is not extra "information" but part of the statement of the problem. The density of states function indicates where the states of the system are located, but says nothing about how these states are filled. It is simply a scheme to group the energy levels.

To determine the expectation value $\langle f(x) \rangle$ data were collected for the first 120 racing days of the 1967 season at Aqueduct racetrack in New York City. A total of 1075 races were analyzed. The odds were reported to the nearest \$0.10. These are not discrete values but comprise odds intervals \$0.10 in size. For example, odds of 2.10 to 1 actually represent the entire interval 2.10 to 2.1999. The average odds of a winning horse were calculated and found to be equal to \$5.76930232 to \$1. The complete data are not presented here.

The density of states function was computed as follows. Out of the 120 racing days, 15 were chosen using a table of random numbers. This comprised 135 races and approximately 1200 horses. The data were the odds of each horse in the 135 race sample. In order to treat the data more easily, they were grouped into a histogram, following the method of Hald[7]. The histogram is used so that the characteristic features of the distribution can be shown.

The data were grouped into 25 intervals to form the histogram. The sizes of the intervals, called the class lengths, were \$1 at the lower odds. At higher odds, where there were less data, it was found

necessary to have larger class lengths, in order to maintain a relatively smooth distribution. The assignment of interval lengths is, of course, somewhat arbitrary. However, various combinations were tried and the results did not vary too greatly. Table I shows the grouping of the data. Class length, interval midpoint, number of points in each interval, and number of points in the interval per $0.10 are shown. A midpoint of $1.50 and a class length of $1 means that the interval includes all the data from $1.00 to $1.9999. The few data points over $100 have been left out.

The histogram itself is the graphical representation of the grouped data. It is in the form of a step function whose value, over a particular interval, is the number of data points in that interval per unit class length. The histogram has the property that the area of each step on a plot of frequency per unit class length versus odds, is equal to the frequency of points in that interval; the total area of all the steps is equal to one. The frequency can be found from the data points by dividing by the total sample.

A more useful form of the histogram is the frequency polygon. In this representation, the midpoints of the intervals are connected by straight lines. This figure can be approximated by constructing a smooth curve through the midpoints.

The density of states function $w[f(x)]$ depends also on the number of data points considered in the total sample. However, it will vary only by some constant factor. It can be seen from Eq. (17), that in the calculation of the probabilities, this constant is canceled out. Thus, for simplicity, the density function will be taken as the number

of data points in an interval per \$0.10, as is tabulated in Table I.

An attempt was made to describe the data for $w[f(x)]$ by some analytical function. For various reasons, this did not prove to be useful. The only curve which gave a good representation of the data was a high order polynomial. This had to be multiplied by an exponential and integrated, as in Eq. (15). However, the limits of integration would in this case, have to be finite, and the results of the integration were not amenable to further manipulation. A graphical scheme was thus decided upon.

The first step in the determination of the probabilities is to determine the multiplier μ from Eqs. (13) and (15). From Eq. (15),

$$\frac{dZ(\mu)}{d\mu} = \frac{d}{d\mu} \int_0^\infty w(y)\, e^{-\mu y}\, dy \tag{18}$$

where again $y = f(x)$. Differentiating with respect to μ inside the integral yields

$$\frac{dZ(\mu)}{d\mu} = \int_0^\infty -y\, w(y)\, e^{-\mu y}\, dy \tag{19}$$

From Eq. (13),

$$\int_0^\infty -y\, w(y)\, e^{-\mu y}\, dy = - \langle y \rangle Z(\mu) \tag{20}$$

Substitution of Eq. (15) yields,

$$\int_0^\infty [y - \langle y \rangle]\, w(y)\, e^{-\mu y}\, dy = 0 \tag{21}$$

since $\langle y \rangle$ is a constant.

An iteration was performed on the IBM 7094 computer, calculating the value of the integrand of Eq. (21) for different values of μ. The expectation value $\langle y \rangle$ had already been found to be 5.769. The values for y and $w(y)$ were taken from Table I, with $w(y)$ identified with the number of points per \$0.10 and y with the interval midpoint. Intermediate values of $w(y)$ were calculated on the computer by a third order Aitken polynomial interpolation scheme. The results were plotted as the value of the integrand I versus y for various values of μ. Integration was performed by counting the squares under each curve. The correct value of μ is found from the curve whose area is zero. Figure 1 shows the curves in the region of interest. Figure 2 shows the area under the curves as a function of μ. The area equals zero at $\mu = 0.108$.

The next step is to calculate the partition function $Z(\mu)$ from Eq. (15). This is done by plotting the integrand of Eq. (15) with $\mu = 0.108$ and counting the squares underneath the curve, as is shown in Figure 3. The area under the curve Z equals 44.06.

With Z known, the probability $p_{f(x)}$ in Eq. (17) can now be determined. This is plotted in Figure 4. The other curve in Figure 4 is a plot of the distribution of winners from the original sample of 1075 races. The data were grouped in a histogram by the method previously described. The grouping of the data is tabulated in Table II. The few data over \$35.00 have been left out.

It is important to realize what the probabilities in Figure 4 represent. They are probabilities per unit class length, and they represent the probability of a point being anyplace in the entire

interval. However, since the curve is continuous, it can be used to determine the probability of being in an interval of any desired size. For example, the probability of being in the interval \$2.00 to \$2.0999 is given by the ordinate at \$2.05 multiplied by 0.10, which is the length of the interval. In the limit, the probability of being in the interval $f(x) + df(x)$ is given by $p_{f(x)}df(x)$, where $p_{f(x)}$ is the ordinate of the graph.

It can be seen from Figure 4, that the predicted distribution is quite similar to the actual distribution. It is felt that with more data, for both the experimental probabilities and the density of states function, the agreement would be even better, and that the maximum entropy postulate does indeed predict a distribution that closely resembles the true one.

It may be of practical interest to the horseplayer to calculate the probability of a horse, that is going off at a particular odds, winning a race. This can be determined quite easily from either of the probability curves in Figure 4.

Consider two events, A and B, where A is the event of going off at a particular odds, say, $f(x_k)$ to 1, and B is the event of winning a race. What the horseplayer desires to calculate is the conditional probability of winning, given that a horse is going off at a certain odds, or $p(B|A)$. The curves in Figure 4 represent the conditional probability of a horse going off at $f(x_k)$ to 1, given that it has won, or $p(A|B)$. The two probabilities are related by

$$p(B|A) = p(A|B) \cdot p(B)/p(A) \qquad (22)$$

where p(A) is the probability of a horse going off at a particular odds, which is simply the density of states function expressed on a percentage or probability base; p(B) is the probability of winning, which is simply the reciprocal of the average number of horses per race. This can be determined easily from the data. With the conditional probabilities calculated, the horseplayer can easily determine the expectation value of any given bet by multiplying the probability by the profit for a winner at the given odds. In this way, the "best" bet in any given race can be determined, based only on the odds. It remains for the horseplayer to determine whether any odds interval will actually produce a profit (by overcoming the 15-17% "take" of the state and track).

Recently, Rowlinson[8] has criticized the indiscriminate use of the maximum entropy postulate for predicting probability distributions. He claims that knowledge of the physics of the problem is necessary to determine whether maximization of the entropy will yield probabilities consistent with the experimental results. Rowlinson does not suggest what physical characteristics are necessary, save that the probabilities can be defined as frequencies in an ensemble. In the present problem, the probabilities can certainly be construed as frequencies and the use of information theory to predict the distribution would presumably be valid in Rowlinson's view.

It does seem, however, that Rowlinson takes a somewhat narrow view of the application of information theory. It is only claimed that the maximum entropy postulate yields the least biased guess of the probability distribution for the information given. This point is not

disproved by Rowlinson. His idea that indiscriminate use of information theory may yield basically useless results should be well taken, however.

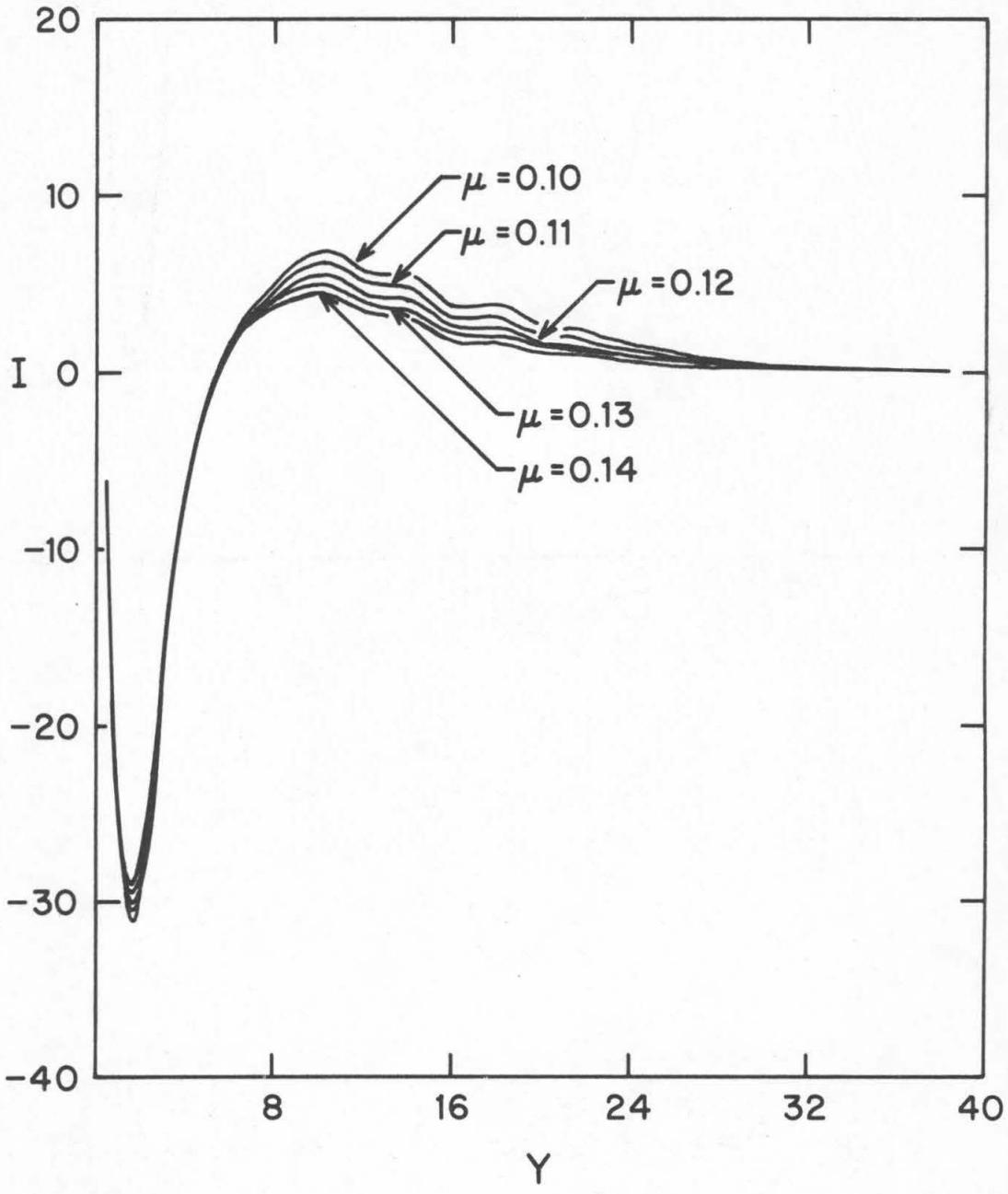

Figure 1. Traced computer plot of I vs. y for different values of μ where $I = (y - 5.769)\, w(y)\, e^{-\mu y}$

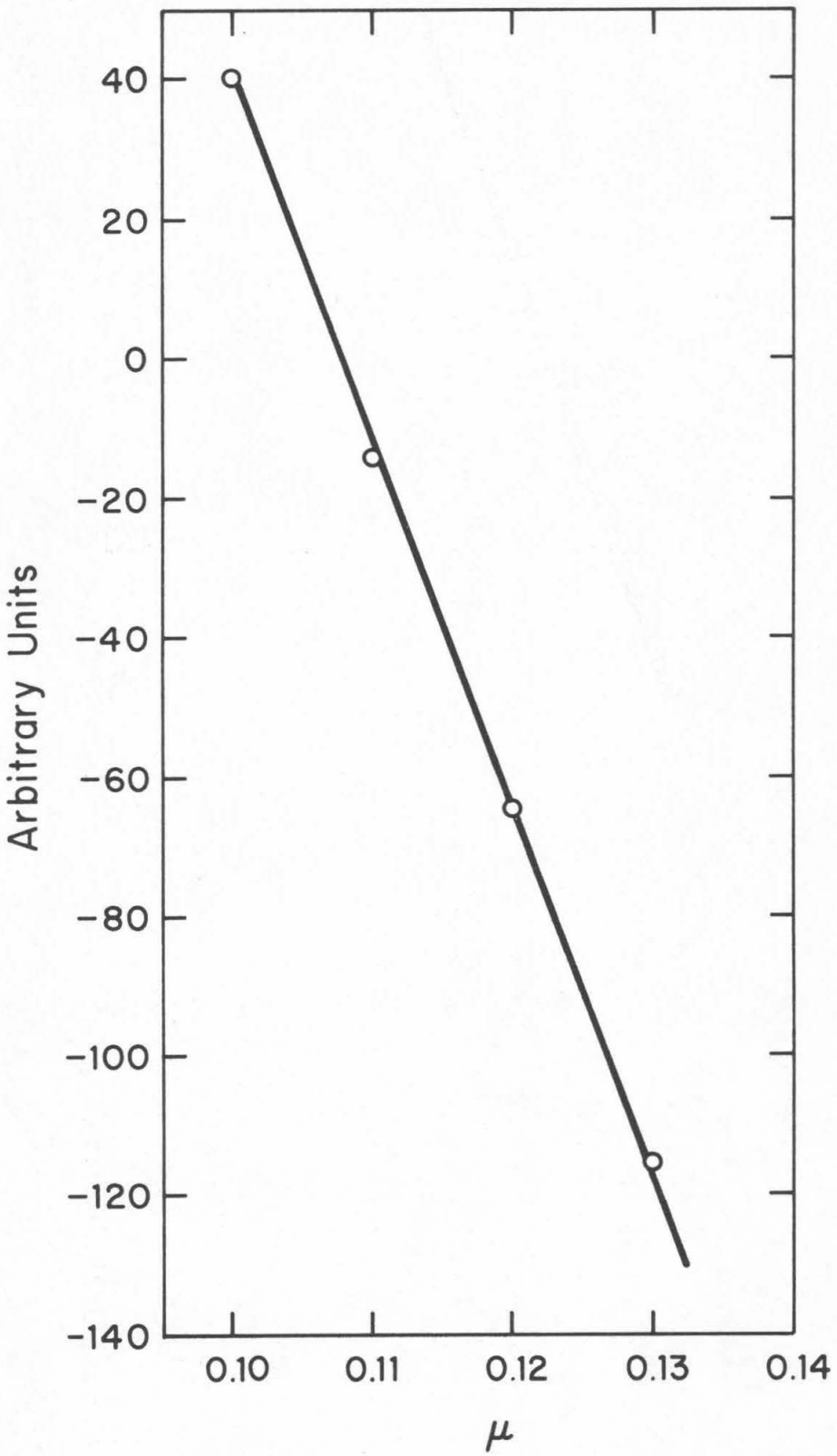

Figure 2. Area under curves in Figure 1, arbitrary units

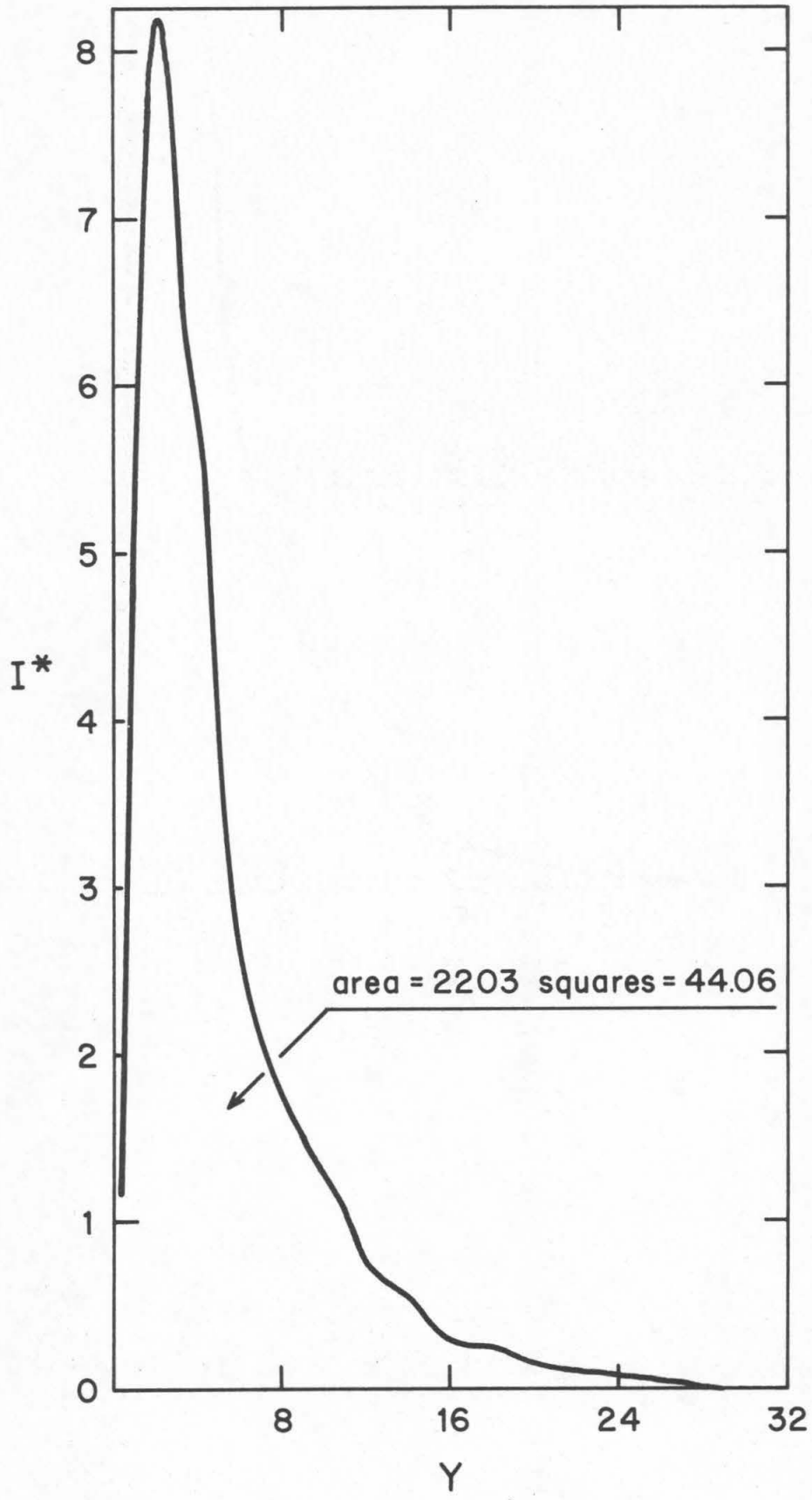

Figure 3. Traced computer plot of I^* vs. y where $I^* = w(y)\ e^{-0.108y}$

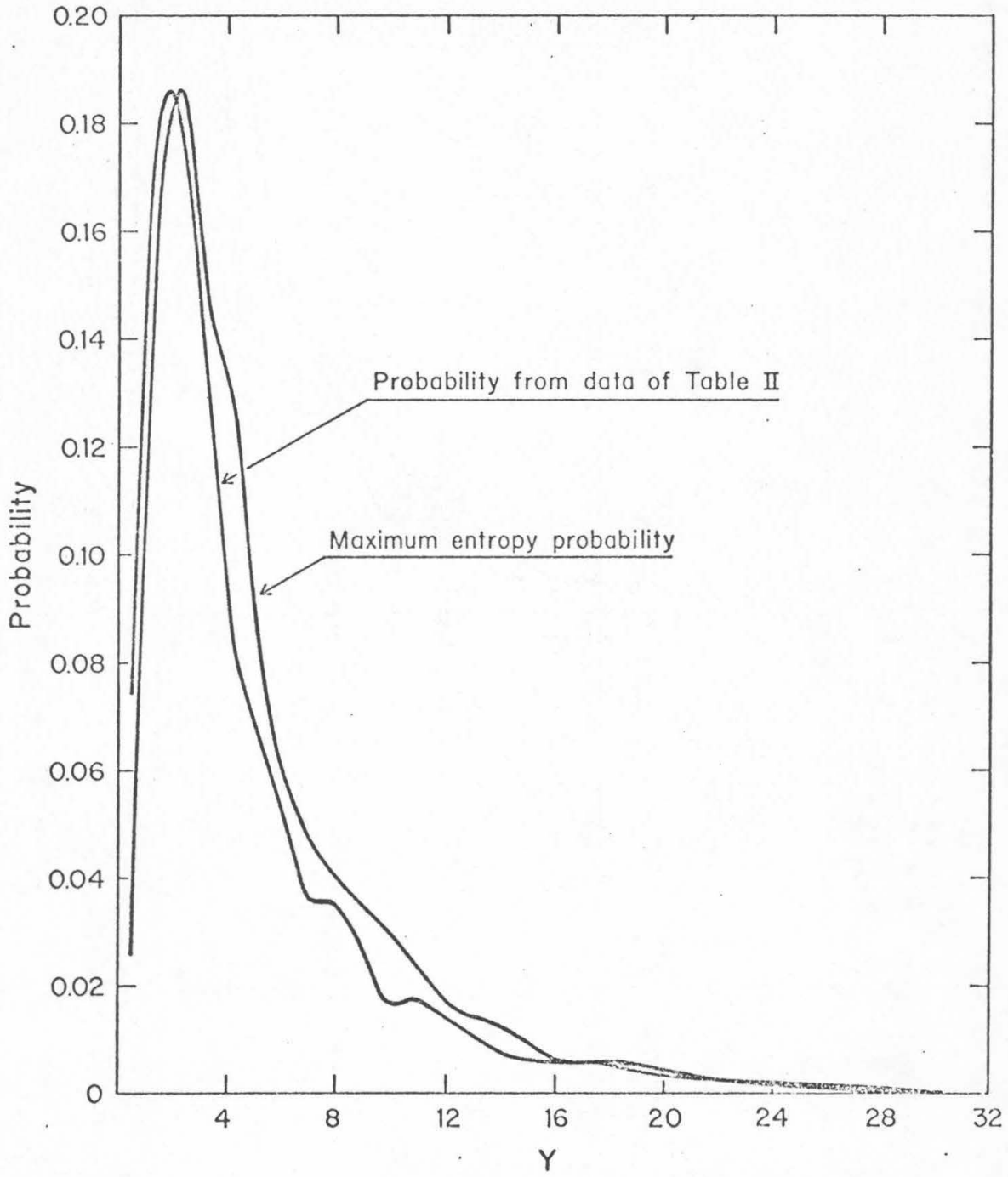

Figure 4. Traced computer plot of experimental and maximum entropy probabilities

TABLE I

Histogram grouping for odds of all horses

Midpoint ($) f(x)	Class Length ($)	# of Points	Points per $0.10 w[f(x)]
0.50	1	12	1.2
1.50	1	81	8.2
2.50	1	107	10.7
3.50	1	93	9.3
4.50	1	91	9.1
5.50	1	65	6.5
6.50	1	53	5.3
7.50	1	47	4.7
9.00	2	88	4.4
11.00	2	81	4.05
13.00	2	58	2.9
15.00	2	55	2.75
17.00	2	36	1.8
19.00	2	40	2.0
21.00	2	31	1.55
23.00	2	28	1.4
25.00	2	24	1.2
27.00	2	19	0.95
29.00	2	14	0.7
35.00	10	43	0.43
45.00	10	34	0.34
55.00	10	21	0.21
65.00	10	18	0.18
75.00	10	13	0.13
90.00	20	21	0.105

TABLE II

Histogram grouping for winners

Midpoint ($) f(x)	Class Length ($)	# of Points	Probability per $1 Class Length
0.50	1	80	0.0745
1.50	1	191	0.1775
2.50	1	189	0.1759
3.50	1	139	0.1292
4.50	1	90	0.0837
5.50	1	72	0.0670
6.50	1	55	0.0512
7.50	1	39	0.0362
8.50	1	38	0.0354
9.50	1	30	0.0279
10.50	1	18	0.0167
11.50	1	19	0.0177
12.50	1	16	0.0149
15.00	4	32	0.0074
19.00	4	27	0.0063
23.00	4	13	0.0030
27.00	4	9	0.0021
32.00	6	2	0.0003

Nomenclature

F	Function defined by Eq. (4)
$f(x)$	Profit function
G	Function defined by Eq. (5)
H	Uncertainty function
K	Positive constant
L	Function defined by Eq. (6)
$p(B\|A)$	Conditional probability of event B given event A
p_i	Probability of event i
w	Density of states function
y	$f(x)$
Z	Partition function
λ'	Lagrangian multiplier
λ	$\lambda' + 1$
μ	Lagrangian multiplier
$< >$	Expectation value

References

1. C. E. Shannon, Bell Sys. Tech. J. 27, 379, 623 (1948).

2. L. Brillouin, Science and Information Theory (Academic Press, New York City, 1962).

3. M. Tribus, Thermodynamics and Thermostatics (Van Nostrand, Princeton, N.J., 1961), p. 77.

4. E. T. Jaynes, Phys. Rev. 106, 620 (1957).

5. W. Steele, Bet the Horses and Win (Pyramid Books, New York City, 1962), p. 68.

6. T. L. Hill, Introduction to Statistical Thermodynamics (Addison-Wesley, Reading, Mass., 1960), p. 65.

7. A. Hald, Statistical Theory with Engineering Applications (John Wiley & Sons, New York City, 1952), p. 44.

8. J. S. Rowlinson, Nature 225, 1196 (1970).

Proposition II

It is proposed that the platinum resistance thermometer calibration apparatus designed by Dr. C. M. Knobler[1] be modified to afford better temperature control and allow more accurate calibration.

A cross-section of the existing apparatus is shown in Figure 1[1]. Basically, the apparatus consists of a cylindrical copper block D which houses the platinum resistance elements to be calibrated C. There are six elements in all, spaced 60 degrees apart. The elements are doped platinum wires, wound on a glass core and covered with a thin layer of glass[2]. Each element is approximately 25 mm long and 2 mm in diameter. The thermometers have a nominal ice point resistance of 100 ohms. Silicone oil is used in the thermometer wells to assure good thermal contact between the thermometers and the block.

The elements are calibrated against a strain-free Leeds and Northrup platinum resistance thermometer H which has a National Bureau of Standards calibration certificate. The nominal ice point resistance of the standard thermometer is 25.5 ohms. The standard thermometer was mounted in a tapered copper plug with Wood's metal. The plug was pressed firmly into a hole in the copper block; silicone oil was again used to promote thermal contact. Heater wires were wound around the plug to heat the copper block.

The block is completely enclosed within an adiabatic temperature shield G. Heater wires and thermocouples are used to control

the temperature of the shield to be the same as that of the block. Two additional radiation shields B and J are also used.

The block is supported by the top shield with silk threads. The shields and block are in turn supported by three lucite rods F which are connected to the support lid A . The support lid rests on a brass flange soldered to the inside of a steel vacuum jacket E .

A lucite end plate K with an O-ring seal provides the closure for the vacuum jacket. All thermometer, thermocouple, and heater wires are bundled together and passed through the end plate by soldering to copper pins epoxied into holes in the plate. The outlet L is connected to a helium source and vacuum station.

The entire assembly is immersed in a coolant, which can be either liquid nitrogen, acetone - dry ice, or water, depending on the temperature range.

The vacuum jacket is initially filled with helium, which acts as a heat transfer agent for the cooling of the block. When the block reaches the temperature of the bath, the jacket is evacuated to about 5×10^{-4} torr with an oil diffusion pump. Calibration points are taken at approximately $10^{\circ}C$ intervals. The calibration temperature is reached by heating the block with heater wires wound around the tapered plug.

The resistances of the standard and unknown thermometers are determined with a Leeds and Northrup Wenner potentiometer. The potentiometer measures potential differences rather than resistances. The resistances are determined from the potential measurements and current measurements, which are calculated by measuring the potential drop

across a standard resistor. It is required to repeat all measurements with the direction of the current reversed, in order to eliminate the effects of stray electromotive forces. The six elements to be calibrated and the standard thermometer are all connected in series. The calibration current is 1 ma. A schematic diagram of the potentiometer circuit is shown in Figure 2 [3].

The sequence of measurements is as follows: current determination, standard thermometer, current, unknown thermometer, current, standard thermometer, current, and so on, for all six unknown thermometers. Each measurement is taken for both forward and reverse current direction, with the two results averaged. Current and temperature interpolations are required to calculate the exact temperature at which the resistance readings are taken.

Three modifications to the present design are proposed. First, the cooling fluids in which the vacuum jacket is immersed should be replaced by a variable temperature bath, whose temperature is adjustable to that of the copper block. Second, heater wires should be attached to the outside surface of the copper block, replacing the present heaters at the center of the block. The third modification is the replacement of the potentiometer by a bridge which can measure resistances directly.

During the calibration, the temperature of the block was as much as 100^{o}C above the temperature of the coolant. Even when the block was only 20^{o}C above the coolant temperature, it was found that the block temperature continuously dropped, as a result of its losing heat[4]. This heat loss was probably due to the inability of the

radiation shield heaters to keep up with the heat lost by the shields to the bath, thus causing the block to lose heat to the shields. Heat is transferred by three main mechanisms: radiation, residual gas conduction, and conduction along wires and supports.

It is felt that increasing the resistance of the heater wires in the shields to increase the rate of heating is not the answer because of increased control problems, especially overheating of the shields. In any case, a temperature difference as large as 50-100^{o}C must cause some heat losses in the system.

The proposed solution here is the use of a variable temperature bath. The major advantages will be both increased accuracy and decreased measurement time. The procedure followed with the cooling fluids was to allow the level of the coolant to drop below the level of the calibration apparatus, thus increasing the temperature of the steel vacuum jacket and decreasing the heat lost from the shields. Measurements were taken when the temperature of the block remained relatively constant. This trial and error procedure proved to be very time consuming. A variable temperature bath could be set at the desired temperature, thus greatly reducing the waiting time. The drifting of the block temperature could be significantly reduced during the measurements, thus improving the calibration accuracy.

The most common types of variable, low temperature baths have employed a liquid hydrocarbon cooled by liquid nitrogen[5]. However, these methods have an inherent fire hazard. In addition, the proper hydrocarbon must be found for the temperature range of interest. Since it is desired to calibrate the thermometers over a wide temperature

range, a number of different hydrocarbons would be required. The present proposal employs gaseous nitrogen cooled by liquid nitrogen to cool the vacuum jacket.

The gaseous nitrogen, from a pressurized tank, would pass through liquid nitrogen in a Dewar vessel and be cooled. The cold nitrogen would then pass through cooling coils which would be placed on the vacuum jacket. The nitrogen can be recycled if desired.

The temperature of the gas stream can be controlled by a previously calibrated thermocouple, used in conjunction with a heating element. One end of the thermocouple can be connected to the radiation shield, the other end to the inside of the vacuum jacket. The heater should be placed in the gas stream. In this way the copper block, radiation shields, and vacuum jacket will all be at approximately the same temperature. A schematic diagram of the proposed system is shown in Figure 3.

Temperature control in this system should be good. If the control system used is similar to the one presently used for controlling the radiation shield temperature, temperature control to within $\pm$ 0.01^{o}C should be possible for a low heating rate.

With this temperature difference, the heat transfer rate between the shields and the bath should be considerably reduced. There should be no problem in attaining a stable, steady-state temperature in the block, probably to within a few thousandths of a degree.

The second modification is the addition of heater wires to be would evenly around the surface of the copper block. The block is heated when a new calibration temperature is desired. The present

heater wires, which are wound around the tapered copper plug in the center of the block, have proved to be quite inefficient. With the present heaters, it takes about two hours to raise the temperature at the center of the block $10^{o}C$. An additional hour, or more, is required to eliminate the radial temperature gradient in the block a after the heater is shut off.

The probable reason for this inefficiency is the inability of the heater to disperse its heat effectively. The heater wires are packed tightly around the plug and are coated with heavy layers of varnish. Thus, much of the heat is probably trapped and unable to get to the block.

The proposed heater wires can be wound evenly around the surface of the block, with a minimal amount of insulation. The heating of the block should be considerably more rapid with this configuration.

The third proposal is to replace the potentiometer by a Mueller bridge. The Mueller bridge consists of a Wheatstone bridge type circuit and measures the resistance directly, without the necessity of measuring potential differences and currents. With the potentiometer, the current was found to vary with time, and interpolations were necessary to determine the current at a particular time.

The method for determining resistances using a Mueller bridge is illustrated in Figure 4 [6]. Two measurements A and B are necessary to determine an unknown resistance X. The ratio arms R_1 and R_2 are adjusted to equality. The leads of the platinum thermometer are designated as C, c, t, and T. The resistances required to balance the bridge for measurements A and B are given by R_a and R_b

respectively. From balance A ,

$$R_a + C = X + T \tag{1}$$

and from balance B ,

$$R_b + T = X + C \tag{2}$$

Adding Eqs. (1) and (2) yields

$$X = (R_a + R_b) / 2 \tag{3}$$

Accuracies of up to $\pm$ 100 micro-ohms are not unreasonable with a good bridge[7]. Over the whole temperature range, a change of $1^{o}C$ is equivalent to a change of about 0.4 ohms for the platinum elements. Thus $\pm$ 100 micro-ohms is equivalent to about $\pm\ 2.5 \times 10^{-4o}C$. This is about five to ten times the estimated accuracy of a potentiometric reading. It should be mentioned, however, that these figures do not represent the over-all accuracy of a temperature measurement. A determination of this figure must include, among other things, an estimation of the accuracy of the standard thermometer, and possible temperature interpolation errors, if there is some change in the block temperature.

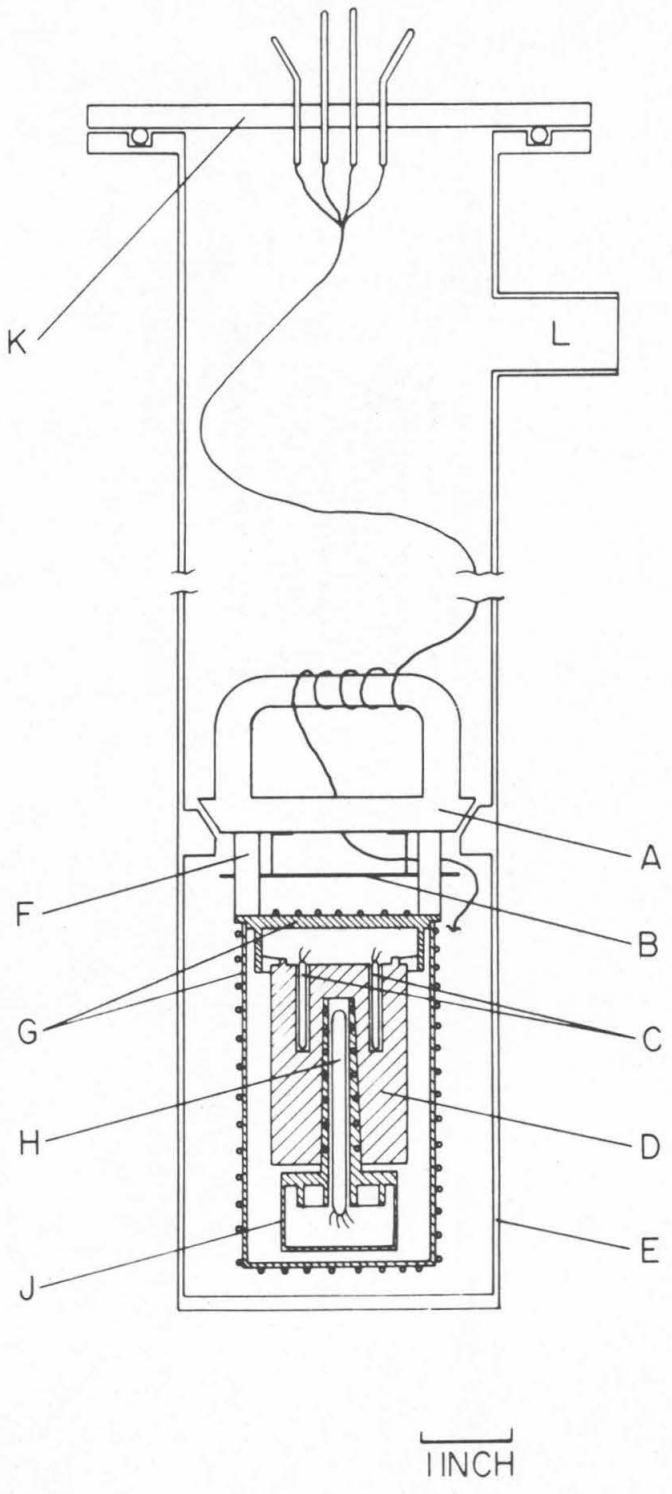

Figure 1. Existing thermometer calibration apparatus[1]

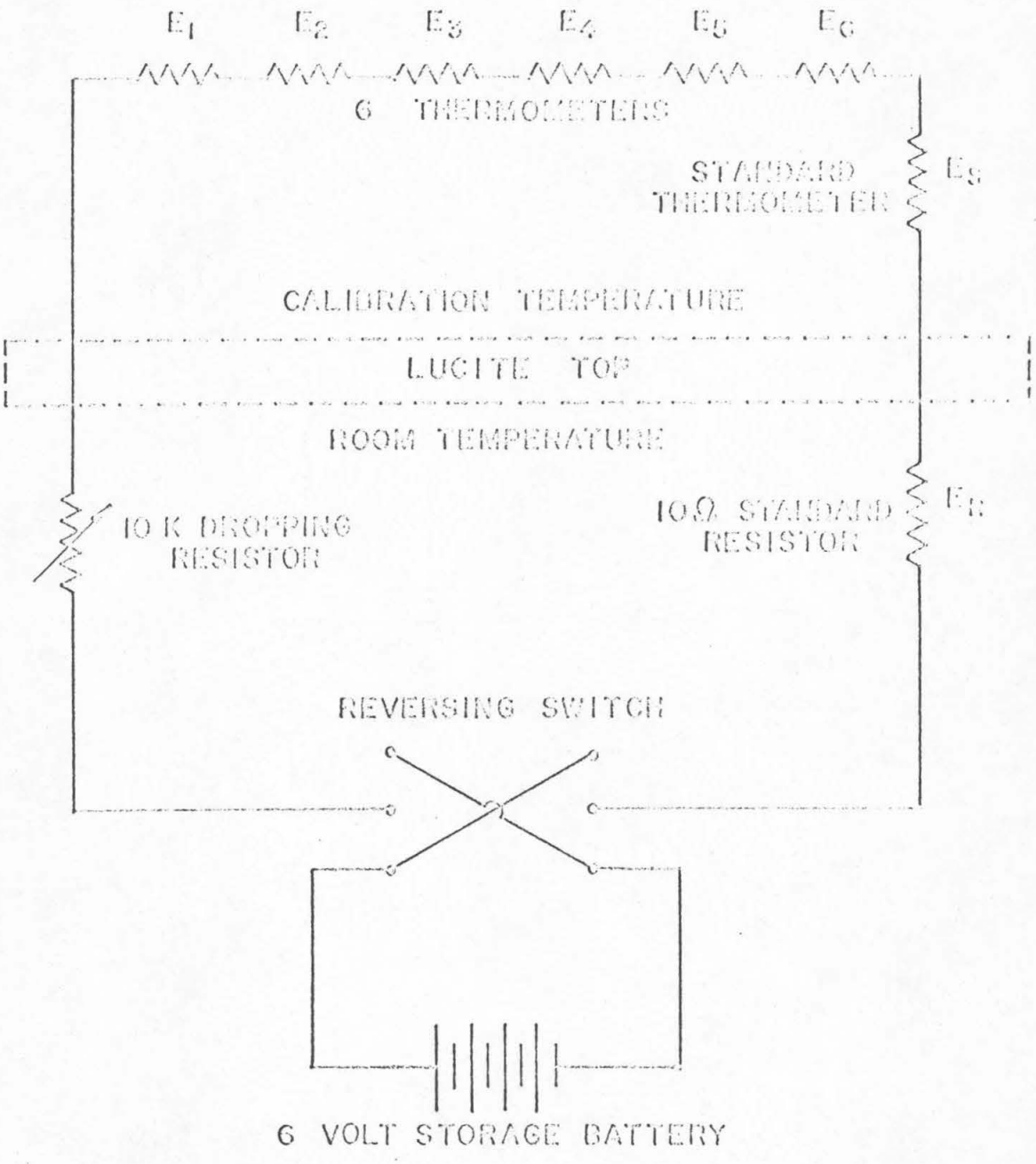

Figure 2. Existing thermometer calibration circuit[3]

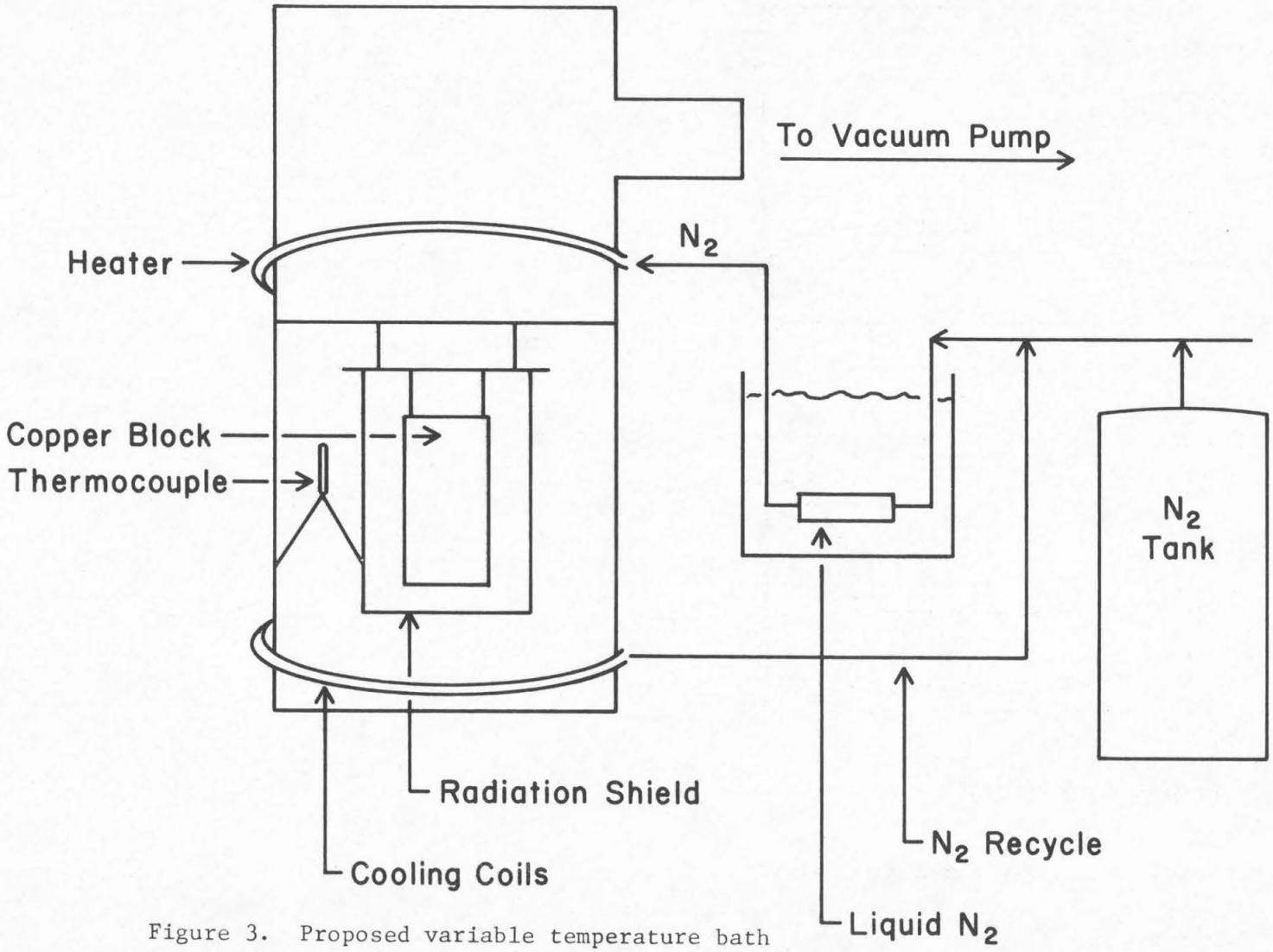

Figure 3. Proposed variable temperature bath

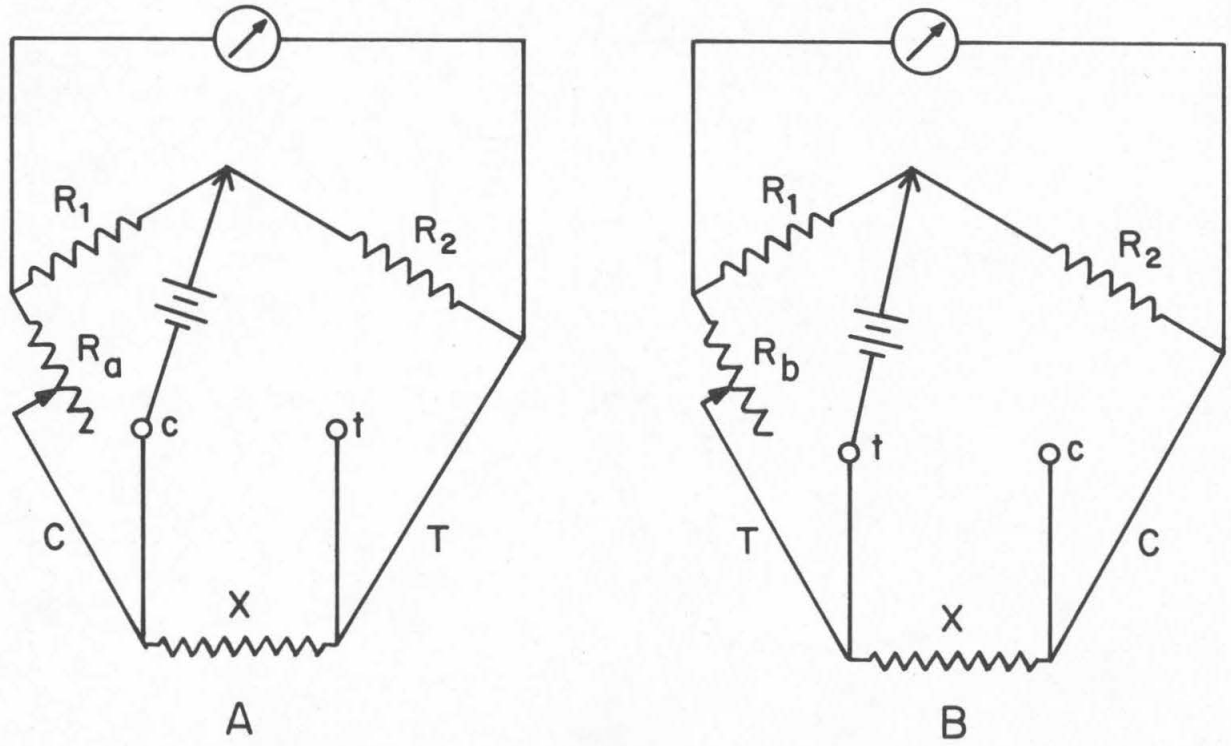

Figure 4. Mueller bridge operation

References

1. W. I. Honeywell, Ph.D. thesis, California Institute of Technology, 1964.

2. C. M. Knobler, W. I. Honeywell, and C. J. Pings, Rev. Sci. Instr. 34, 1437 (1963).

3. S. C. Smelser, Ph.D. thesis, California Institute of Technology, 1969.

4. Thermometer calibrations done by J. F. Karnicky, P. F. Morrison, and H. J. Strumpf.

5. K. D. Timmerhaus, ed., Advances in Cryogenic Engineering, Vol. 1 (Plenum Press, New York City, 1960), p. 126.

6. E. F. Mueller, in Temperature, Its Measurement and Control in Science and Industry, American Institute of Physics, Vol. 1 (Reinhold Publishing Co., New York City, 1941), p. 168.

7. H. F. Stimson, in Temperature, Its Measurement and Control in Science and Industry, ed. by H. C. Wolfe, Vol. 2 (Reinhold Publishing Co., New York City, 1955), p. 151.

Proposition III

It is proposed that a cell be designed and built with the idea of measuring the thermal conductivity of binary liquid mixtures in the consolute region. With the completion of the viscosity measurements in the gas-liquid critical region[1], the behavior of the thermal conductivity of binary mixtures is a major gap in the study of transport properties in the critical region.

Investigation into the behavior of the thermal conductivity of binary mixtures near the consolute or critical mixing point is of great interest. The critical mixing points are of two types, called upper and lower consolute points. For an upper consolute point, the components become miscible in all proportions above the critical temperature. For systems exhibiting a lower consolute point, the components are totally miscible below the critical temperature, at least until a solid phase is formed. There seems to have been only one serious investigation concerning the consolute thermal conductivity, that of Gerts and Filippov[2], reported in a Russian journal which is not readily available in an English translation. The authors present scant experimental details but conclude that there is no anomaly in the thermal conductivity. The claim of this one investigation is being perpetuated in the critical region literature, perhaps incorrectly.

It seems well established experimentally that there is a large anomaly in the thermal conductivity of a pure substance in the region

of its gas-liquid critical point[3]. Since the different types of critical systems are often considered analogous, it might be expected that the consolute thermal conductivity would also exhibit an anomaly. This seems even more reasonable since the recent viscosity data of the present author[1] seem to indicate that the anomalies for gas-liquid critical points and binary consolute points may be analogous.

It is proposed that a non-steady-state hot wire device be used to measure the thermal conductivity. For this method, the temperature change of a heated wire is monitored as a function of time. The time-temperature behavior of the wire can be related to the thermal conductivity of the fluid in which the wire is immersed by the following development. Consider the general equation of energy as given in Bird, Stewart, and Lightfoot[4], with the velocity terms eliminated and the pressure held constant:

$$\rho C_p \frac{\partial T}{\partial t} = - (\nabla \cdot q) \qquad (1)$$

where ρ is the density of the fluid

C_p is the heat capacity at constant pressure of the fluid

T is the temperature

t is the time

q is the rate of heat generation per unit area

Equation (1) can be solved with the aid of Fourier's law of heat conduction:

$$q = -k \nabla T \qquad (2)$$

where k is the thermal conductivity of the fluid. The density, heat capacity and thermal conductivity are assumed to be constant for

this development.

The hot wire is considered to be an infinite line source. At time $t = 0$ the temperature at the surface of the wire is T_o. This is also the temperature at radial distance $r = \infty$ for all t. At time $t = 0+$, a nonvarying current is applied to the wire. The rate of heat generation per unit length of wire q_ℓ is assumed to be constant. For the above boundary conditions, the solution to Eq. (1) is given in Carslaw and Jaeger[5].

$$T(r,t) = T_o - \frac{q_\ell}{4\pi k} \text{Ei}(-\frac{r^2}{4\alpha t}) \tag{3}$$

where α is the thermal diffusivity of the fluid equal to $k/\rho C_p$

Ei is the exponential integral given by

$$\text{Ei}(-x) = -\int_x^\infty \frac{e^{-u}}{u}\, du \tag{4}$$

The exponential integral can be expanded for small values of $(\frac{r^2}{4\alpha t})$ as follows[5]:

$$\text{Ei}(-\frac{r^2}{4\alpha t}) = \gamma + \ln(\frac{r^2}{4\alpha t}) - \frac{r^2}{4\alpha t} + \frac{1}{4}(\frac{r^2}{4\alpha t})^2 + \cdots \tag{5}$$

where γ is Euler's constant, equal to 0.5772. The term $(\frac{r^2}{4\alpha t})$ is very small since the wire is "almost" a line source. Thus the term $\ln(\frac{r^2}{4\alpha t})$ in Eq. (5) is much larger than the other terms. Equation (3) can then be approximated by

$$T(r_o,t) = T_o - \frac{q_\ell}{4\pi k} \ln(\frac{r_o^2}{4\alpha t}) \tag{6}$$

where r_o is the radius of the wire. Since r_o is constant

$$T(t) = T_o - \frac{q_\ell}{4\pi k} \ln \frac{r_o^2}{4\alpha} + \frac{q_\ell}{4\pi k} \ln t \qquad (7)$$

Thus, a plot of temperature versus log time should yield a straight line of slope $q_\ell/4\pi k$.

The resistance of the wire is used as a measure of its temperature. If a platinum wire is used, then the temperature-resistance characteristics are well known. For a small change in temperature of the wire

$$\Delta R = \frac{dR}{dT} \Delta T \qquad (8)$$

where dR/dT, the change in resistance of the wire with temperature, can be considered to be constant over the small temperature range. Thus, from Eq. (7),

$$\Delta T = \frac{q_\ell}{4\pi k} \Delta \ln t \qquad (9)$$

Combining Eqs. (8) and (9) yields

$$\Delta R = \frac{dT}{dR} \frac{q_\ell}{4\pi k} \Delta \ln t \qquad (10)$$

From Ohm's law

$$q_\ell = \frac{VI}{\ell} \qquad (11)$$

where ℓ is the length of the wire

V is the voltage

I is the current across the wire.

If the current is adjusted to a constant value,

$$\Delta R = \frac{\Delta V}{I} \qquad (12)$$

Combining Eqs. (10)-(12) yields

$$\Delta V = \frac{dT}{dR} \frac{VI^2}{4\pi \ell k} \Delta \ln t \tag{13}$$

This is the final equation for the data reduction. Since the current is held constant, the heat generation term q_ℓ cannot be constant. In principle, Eq. (1) could be solved for a time dependent heat generation. This would be rather difficult, so it is assumed that the solution is still valid as long as ΔV is kept small.

The non-steady-state method seems particularly well suited for measurements in the consolute region of a binary mixture. The main difficulty for thermal conductivity measurements in the critical region is probably that of convection. The contribution of convection to the total heat transfer is related to the size of the dimensionless grouping known as the Rayleigh number R

$$R = \frac{g\tau\rho^2 C_p \Delta T \, d^3}{k\eta} \tag{14}$$

where g is the local acceleration of gravity

τ is the isobaric expansion coefficient

ΔT is the temperature difference across which the convection occurs

d is the distance across which the convection occurs

η is the viscosity of the fluid.

Close to the critical point (or consolute point) both C_p and τ get very large, resulting in a large increase in the Rayleigh number. Thus, the convective mode of heat transfer could easily be a

significant part of the total heat transfer. It is absolutely necessary to keep the Rayleigh number small for thermal conductivity measurements.

The best work on the gas-liquid critical point thermal conductivity has been done with a steady-state, parallel plate apparatus[3]. Great care was taken to eliminate convection. This was accomplished by keeping the temperature difference across the plates small and especially by keeping the gap d between the plates small. It was necessary to check for the absence of convection by varying the temperature difference and ascertaining that the same thermal conductivity coefficient was calculated.

Although use of the Rayleigh number idea may not be exactly suited to a non-steady-state condition, it can still be quite helpful. When the current is first turned on through the hot wire, the ΔT is small (ΔT in this case can be taken as $T(t) - T_o$), and convection should be absent. As the ΔT increases, convection will presumably set in. However, the onset of convection should be easily seen since a plot of temperature (or voltage) versus $\ln t$ would then deviate from a straight line. The presence of a straight line amenable to the thermal conductivity determination should be proof enough of the absence of convection. This idea neglects, of course, the possibility of some fortuitous cancellation of errors, which would seem to be highly unlikely. It is of great importance to keep the ΔT as small as possible, so that critical point may be approached as closely as possible. Averaging the thermal conductivity over too large a temperature range might mask the critical effects.

The problem which really invalidates the parallel plate (or concentric cylinder) method is that of mixing the components. For a single component fluid, mixing is not necessary. Since measurements are confined to the single-phase region, homogeneity of the phase can easily be attained regardless of the history of the sample. While it is true that equilibration times are longer in the critical region, experience has shown [1] that the desired homogeneity can be reached after a reasonable period of time.

The situation is quite different with the binaries. Even away from the consolute point, if a binary mixture in the two phase region is brought to the single phase region, it is almost impossible to attain homogeneity without stirring. In the critical region, the binary diffusion coefficient becomes very small, thus delaying even further the approach to homogeneity. It is likely that the system would "never" de-mix without a stirrer.

As previously mentioned, the separation of the plates in the steady-state parallel plate method has to be kept very small (say less than 0.05 cm) to limit convection. It would probably be impossible to insure proper mixing in the region between the plates for a binary mixture. A thermal conductivity cell for the non-steady-state hot wire method could be constructed with no "dead" spaces, so that almost any type of stirring device would probably be sufficient to insure proper mixing. Once homogeneity of the single-phase region has been attained, further mixing would not be necessary as long as the system remained in this region. There would be no stirring during the measurements.

Investigations into properties in the region of the consolute point are often performed under what might be considered to be inappropriate conditions. Since the components are liquids at ambient conditions, many experimentors have found it convenient to have the system open to the atmosphere. The pressure of the system is thus always at atmospheric and there is a third phase present (the air vapor phase). The components of air are free to pass into the liquid phases, with the appropriate equilibrium set up.

Another technique used is to have a closed system, wherein the pressure is allowed to follow the vapor pressure of the sample. The pressure is usually much lower than atmospheric in this technique. The vapor pressure method requires corrections so that the property measured can be computed along a useful path, usually that of constant pressure. There is great uncertainty in the necessary corrections in the critical region.

The present proposal is for a closed system with no vapor phase, and the pressure adjusted to a constant, known value. The pressure could be controlled by the use of a diaphragm pressure transducer, connected to the thermal conductivity cell so as not to form any dead end spaces. Each data point would be taken at the same pressure, with the volume of the cell adjusted with a variable volume plunger. During a measurement, as the temperature is increased due to the heat generation of the wire, the pressure could be continuously adjusted, if necessary. Since the ΔT is to be kept small, the pressure change should also be quite small. There would be a large pressure change, however, between the different data points if the volume of the cell was not adjusted.

A small volume change would correct for a large pressure difference, since the liquids used can be expected to be quite incompressible.

As a start, the outside of the diaphragm could be left open to the atmosphere, thus controlling the pressure to the ambient conditions. Since the atmospheric pressure does not vary by more than a few tenths of a percent, the pressure control would be fairly good. The pressure could be measured on a barometer. For finer pressure control, the diaphragm could be connected to a pressure source and measuring system such as a dead weight tester, which would afford the best measurement possible. A whole range of other pressure devices could be used depending on the measurement accuracy desired. A pressure source would afford the opportunity to measure a complete series of thermal conductivities at different pressures.

The temperature and composition of the consolute point varies with pressure; presumably thermal conductivity also varies. The behavior of properties in the consolute region as a function of pressure has been given scant attention experimentally.

There are a large number of binary systems which might be investigated. It is very important to have the components in as pure a form as possible, and to accurately know the critical temperature and composition for the pressure of interest. The mixture 3-methylpentane-nitroethane has been carefully studied and apparently accurate coexistence curve data are available[6]. The consolute temperature of this mixture is in the ambient range, so a water thermostat could be used for temperature control. The thermostat described in Ref. [1] would be ideal for these measurements. The components are available

in quite pure form, and after some simple purification steps, a purity of 99.99% for the 3-methylpentane and 99.97% for the nitroethane can be readily attained[7].

As previously mentioned, the heater wire would probably be made of platinum. A very thin wire is desirable, so that the boundary conditions used in deriving Eq. (13) would be more closely approximated. In addition, a thinner wire yields a larger resistance change with temperature than a wire of larger diameter, thus improving the measurement accuracy. Wires as small as 6×10^{-4} cm in diameter have been used successfully[8].

The thermal conductivity cell would be made of precision bored glass. The visability afforded by a glass cell will be a great help close to the consolute point. A reasonable glass thickness would enable measurements to be taken at pressures up to a few hundred psia if desired. The cell diameter should be large with respect to the wire diameter to justify the assumption of a line source for the heated wire. Although gravitational effects are not as severe for consolute points as for gas-liquid critical points, the pressure change does alter the state of the system and should be kept as small as possible[9]. A cell diameter of 1 cm has been found to be satisfactory in relation to the line source assumption[10] and would give a reasonably small cell height, thus minimizing gravitational effects. The cylindrical axis of the cell would, of course, be parallel to the horizontal. Four electrical leads would be attached to the heater wire, two at each end. The leads could pass through the cell by attaching them to metal pins epoxied into holes in the glass. The heating wire could be epoxied to

small metal pins for support.

One end of the cell can be connected with a teflon gasket to a bellows valve, which acts as a variable volume plunger. The other end of the bellows valve is teed off to the diaphragm transducer and the manifold system. The length of the tee is kept as small as possible to eliminate any "dead-end" spaces. Both the valve and the diaphragm will be immersed in the water bath; the valve could have a handle extension while the electrical wires from the diaphragm could be protected by an air tube. The leads from the heater wire could pass through the same tube. The stirring device could be a small spring passing out the top of the cell through a teflon packing seal. The stirrer would be mechanically driven. Alternatively, a magnetic stirrer could be used. This would have the advantage of not requiring an additional seal. The other end of the glass cell is connected, also with a teflon gasket, to a sealing valve. The valve must have no lubrication in the fluid stream; if a packing valve is used, the valve threads must be above the packing. The valve is connected to the manifold tubing system. The system should include two small removable weighing bombs, which would be used to weigh in accurate masses of the two components. The manifold contains a nonlubricated stainless steel centrifugal pump, which is used to insure proper mixing upon loading. An additional pressure gauge would be useful in metering in the desired amounts of the components. The tubing system should be connected to a high vacuum oil diffusion pump. A schematic drawing of the proposed cell and tubing system is shown in Figure 1.

The loading procedure is important so that the precise composition of the mixture in the cell is known. A scheme such as the one given here could be followed. The weighing bombs are first filled with a known mass of the pure components and connected to the tubing system. Valve #1 is closed and weighing bomb #1 is opened. A predetermined pressure, as read on the gauge, is set by varying the temperature of the weighing bomb. With valve #2 and the bellows valve opened, the same procedure is followed with the other component from weighing bomb #2. The weighing bomb valves are closed, and the components are thoroughly mixed by opening valve #1 and turning on the centrifugal pump. The thermostat temperature is set so the mixture is in the single phase region throughout the manifold. After homogeneity has been established, the pump is turned off and valves #1 and #2 are shut. The weighing bombs can be removed and weighed; the mass of each component initially in the tubing system is determined by difference. These masses yield the accurate composition of the fluid in the closed cell. An entire series of measurements would then be taken for this composition. The temperatures can be measured by a calibrated platinum resistance thermometer immersed in the water bath. Data points can be taken for a series of temperatures in the single-phase region. Stirring would probably not be necessary as long as the fluid remained in the single-phase region. For each data point there is a small ΔT, so the actual state can be taken as the temperature at the mean of the ΔT. The ΔT is determined from the heater wire used as a temperature sensor as previously explained.

The basic electronic component necessary for the thermal conductivity measurements is a recording potentiometer. The potentiometer measures voltage directly. The recorder, which should have a very short time lag, since the total times are short (a few seconds), simply records voltage as a function of time. The recorded data can then be converted to a log time scale, and the slope of the straight line region determined by a linear least-squares technique. From Eq. (13) it can be seen that the slope is equal to $\frac{dT}{dR}\frac{VI^2}{4\pi\ell k}$.

The temperature dependence of resistance dT/dR can be determined by calibration with the measuring platinum resistance thermometer. The term can be assumed constant for the small temperature differences used. The current can be determined from the recorder voltages and the calibrated resistance. Average values of current, voltage, and resistance can safely be used, since the changes should be quite small. An accurate determination of the length of the heater wire between the potentiometer leads is also necessary. Using the above information, the thermal conductivity k can be determined. The state of the system is the constant known pressure and composition, and the mean temperature. It is expected that close to the consolute point the temperature intervals could be as small as $0.01^{\circ}C$.

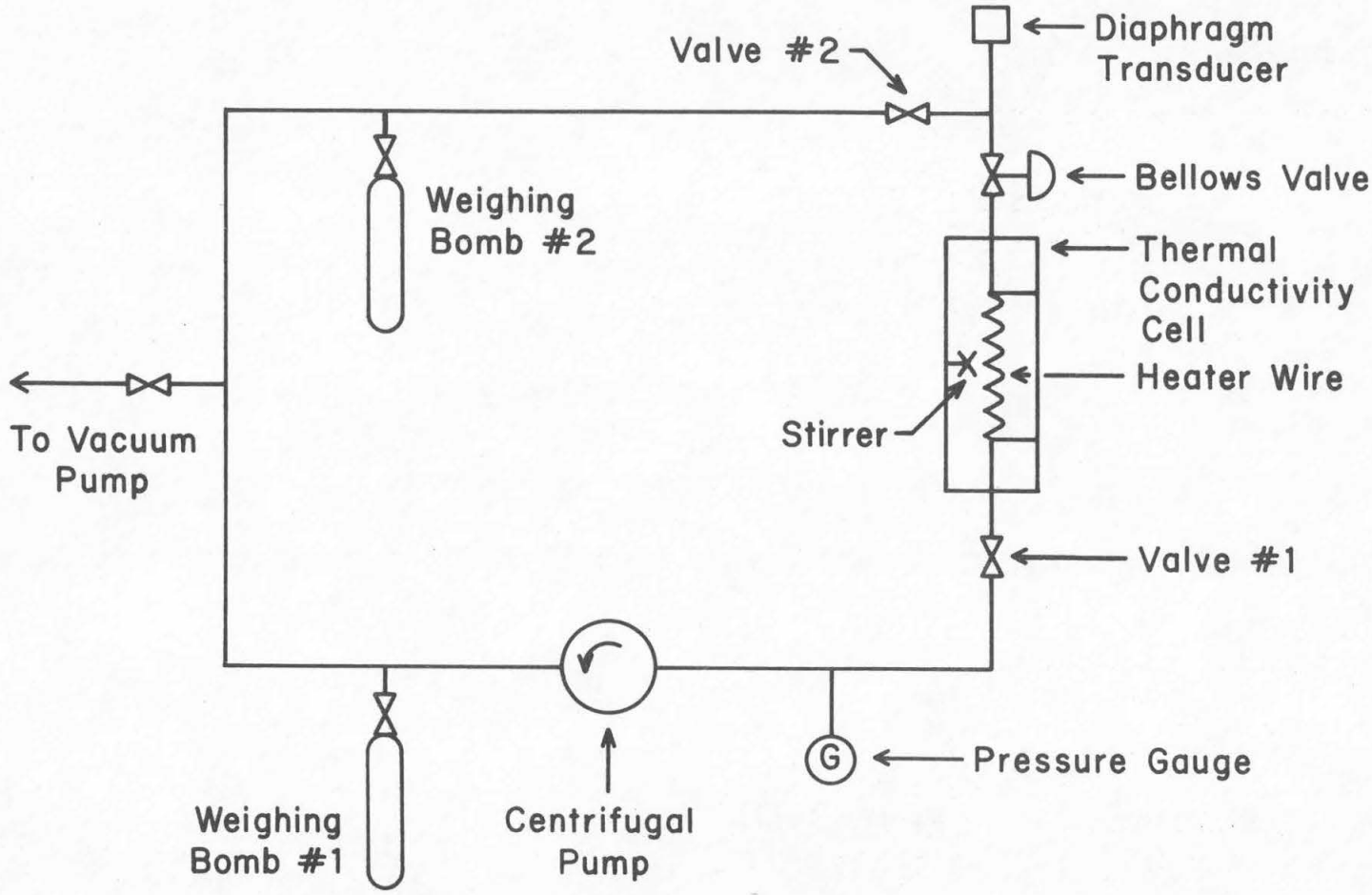

Figure 1. Proposed thermal conductivity apparatus

Nomenclature

C_p	Heat capacity at constant pressure
d	Plate separation
Ei	Exponential integral
g	Local acceleration of gravity
I	Current
k	Thermal conductivity
ℓ	Length of heater wire
q	Rate of heat generation per unit area
q_ℓ	Rate of heat generation per unit length
R	Resistance
r	Radial distance
r_o	Radius of wire
T	Temperature
T_o	Temperature at zero time
t	Time
V	Voltage
u	Dummy variable
x	Dummy variable
α	Thermal diffusivity
γ	Euler's constant
η	Viscosity
ρ	Density
τ	Isobaric expansion coefficient

References

1. H. J. Strumpf, Ph.D. thesis, California Institute of Technology, 1972.

2. I. G. Gerts and L. P. Filippov, Zh. Fiz. Khim. 30, 2424 (1956).

3. J. V. Sengers and A. Michels in Progress in International Research on Thermodynamic and Transport Properties (ASME, Princeton, New Jersey, 1962.)

4. R. B. Bird, W. E. Stewart, and E. N. Lightfoot, Transport Phenomena (John Wiley & Sons, New York, New York, 1960), p. 315.

5. H. S. Carslaw and J. C. Jaeger, Conduction of Heat in Solids, 2nd edition (Oxford University Press, London, 1959), p. 261.

6. A. M. Wims, D. McIntyre, and F. Hynne, J. Chem. Phys. 50, 616 (1969).

7. A. Stein, J. C. Allegra, and G. F. Allen, J. Chem. Phys. 55, 4265 (1971).

8. P. S. Davis, F. Theeuwes , R. J. Bearman, and R. P. Gordon, J. Chem. Phys. 55, 4776 (1971).

9. P. Heller, Rep. Prog. Phys. 30, 731 (1967).

10. J. K. Horrocks and E. McLaughlin, Proc. Roy Soc. 273A, 259 (1963).